Imaging Camera Measurements at Terahertz Frequencies

BSc. Thesis

Rowan Richie
Melle Vorst

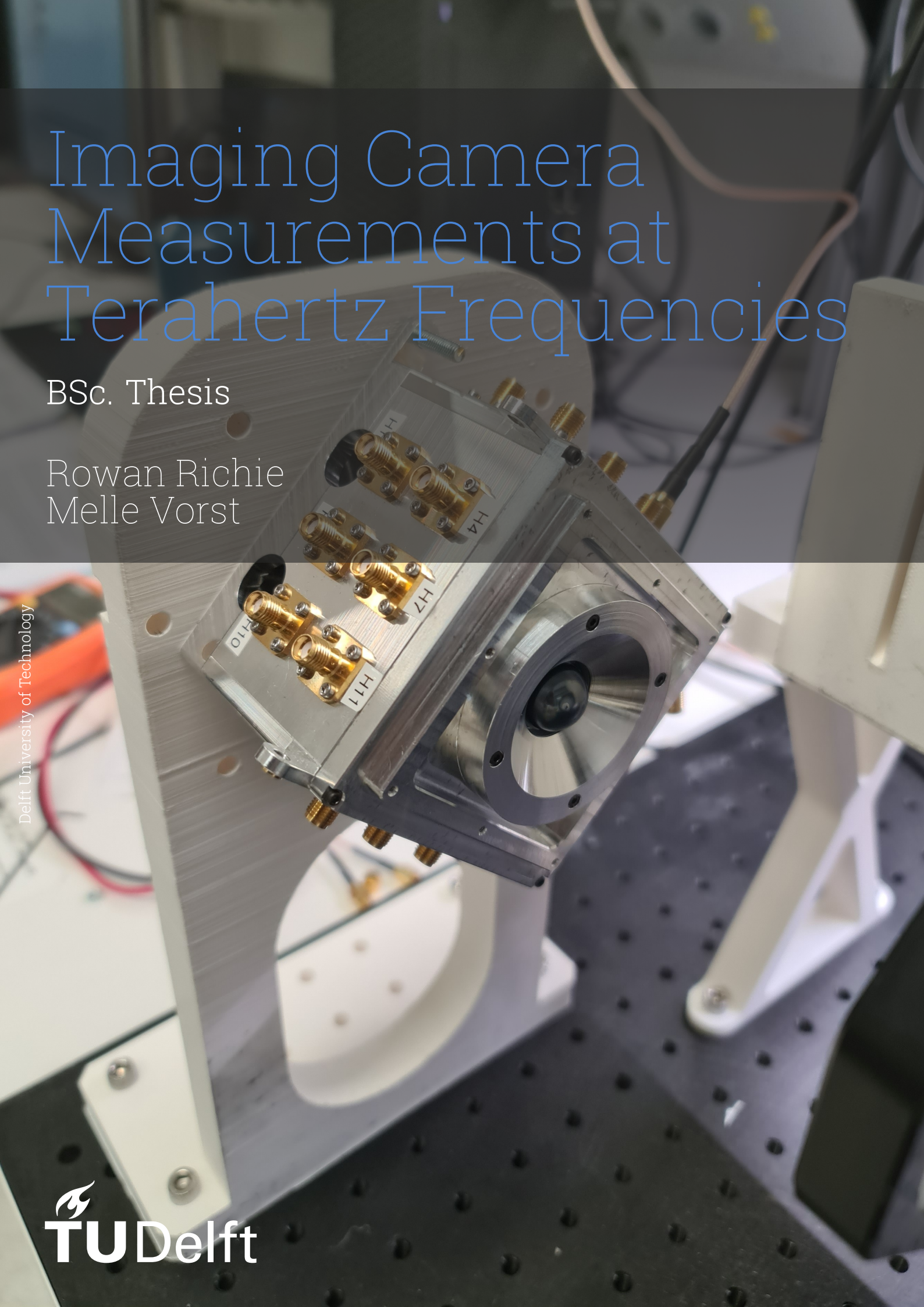

Delft University of Technology

TU Delft

Imaging Camera Measurements at Terahertz Frequencies

BSc. Thesis

by

Rowan Richie
Melle Vorst

Project Duration: April 20th, 2026 - June 26th, 2026
Supervisors: Dr. Maria Alonso-delPino and Dr. Martijn Hoogelander

TU Delft

Abstract

This thesis presents the integration and evaluation of a 24-pixel silicon-germanium bipolar complementary metal-oxide-semiconductor terahertz camera in an active illumination transmission imaging setup. The camera had previously been characterized at detector level, but its performance as part of a complete imaging system still had to be evaluated. The main objective was therefore to determine whether the camera could produce repeatable and interpretable images when combined with the available quasi-optical measurement system. Two MATLAB-based graphical user interfaces were developed. The first interface predicts the expected image resolution for a selected camera configuration, frequency, and sample image. This allows for the expected visibility of object features to be estimated before measurement. The second interface controls the measurement workflow by configuring the source, detector bias supply, readout electronics, data-acquisition hardware, and mechanical positioning system. It provides hardware selection, connection testing, scan definition, live image preview, metadata storage, and image reconstruction from the measured pixel responses. Active imaging measurements were performed on an ivy leaf sample. The measured detector responses were mapped to spatial scan positions, converted to decibels, normalized, and then reconstructed into terahertz transmission images. The main result was obtained around 400 gigahertz, where the leaf outline and central vein were visible in the reconstructed image. Frequency averaging over five neighboring frequency points reduced background variations such as standing waves, while preserving the main leaf structure. The results show that the integrated system can produce interpretable active terahertz images and that the developed workflow supports controlled and reproducible measurements. However, the demonstrated performance is still limited by mechanical scanning time, optical alignment uncertainty, standing-wave artifacts, and pixel-dependent response differences.

Preface

This thesis was written as part of the Bachelor Graduation Project for the BSc Electrical Engineering program at Delft University of Technology. The project was carried out within the THz Sensing Group and focused on the system-level implementation and evaluation of a 24-pixel SiGe BiCMOS terahertz camera.

The work presented in this thesis centered around the development of a controlled and reproducible measurement workflow for active terahertz imaging. This included the integration of the camera with the available quasi-optical setup, source-control hardware, detector readout, data-acquisition equipment, and CNC positioning system. A MATLAB-based hardware-control and image-acquisition interface was developed to configure the instruments, perform automated scans, store measurement data, and reconstruct images from the measured detector responses. The final goal was not only to obtain terahertz images, but also to evaluate how the complete measurement chain affects the performance of the new camera.

We would like to thank our supervisors for their guidance, feedback, and technical support throughout the project. Their expertise was especially valuable during the assembling of the measurement setup, interpretation of the camera behavior, and the refinement of the experimental approach. We would also like to thank the members of the THz Sensing Group for their support in the laboratory and for providing access to the equipment and previous work on which this project builds.

Finally, we would like to thank our fellow students, friends, and family for their support during the project. Their encouragement helped us throughout every stage of this thesis.

Rowan Richie
Melle Vorst
Delft, June 2026

Contents

1

Introduction

1.1. Background and motivation

The terahertz region lies between the microwave and infrared parts of the electromagnetic spectrum. The region covers frequencies from 0.1 to 10 THz [1]. This part of the spectrum combines several properties that are particularly useful for imaging applications. Its wavelength is shorter than that of standard microwave radiation, which allows for a finer diffraction-limited resolution for a given aperture size. At the same time, THz radiation can penetrate a range of non-metallic materials including paper, plastics, fabrics, and some packaging materials. Because the photon energy in the THz range is much lower than that of ionising radiation such as X-rays, THz radiation is generally considered as non-ionising.

These properties have led to research in the field of terahertz imaging for nondestructive inspection, security screening, biomedical analysis, industrial monitoring, and material characterisation [1], [2]. Low-terahertz radar has also been researched for automotive sensing, where the shorter wavelength can provide detailed information about objects and terrain in the vehicle surroundings [3]. However, the usefulness of such a system depends strongly on the application. Material loss, propagation distance, available source power, detector sensitivity, and image acquisition speed all determine whether a practical image can be obtained.

Technologies such as complementary metal-oxide semiconductor (CMOS) and silicon-germanium bipolar CMOS (SiGe BiCMOS) offer a path towards more compact and scalable systems. They allow detectors, antennas, readout electronics, bias circuits, and signal-processing functions to be combined on a single chip or closely integrated package [4]. Their compatibility with existing semiconductor manufacturing methods makes them attractive for the development of larger detector arrays. However, more than a sensitive detector is required to implement a complete THz camera. The detector array, optical system, source, readout electronics, mechanical positioning system, and processing softwar must operate together as one measurement chain.

This thesis concerns the system-level implementation and evaluation of a 24-pixel SiGe BiCMOS THz focal-plane-array camera. The work builds on an earlier 12-pixel CMOS camera and a quasi-optical imaging system that was developed by the THz Sensing Group at Delft University of Technology. The aim is to determine how the improved detector array performs when used to acquire complete images, using the earlier 12-pixel CMOS system as a technical benchmark. The acquired spatial images will be assessed rather than only evaluating detector performance only through circuit-level or radiation-pattern measurements.

1.2. THz imaging architectures

Different imaging systems can be classified according to their detection principle, illumination method, operating temperature, and their approach for image formation. The choices made in the different systems have influence on the achievable sensitivity, spatial resolution, field of view, acquisition time,

and also the system complexity. The main distinctions relevant to the camera used in this thesis are between heterodyne and direct detection, active and passive imaging, and focal-plane-arrays versus mechanically scanned single-pixel systems.

1.2.1. Heterodyne and direct detection

For a system with a heterodyne receiver, the incoming terahertz signal is mixed with a local-oscillator signal. The resulting signal is then translated to a lower intermediate frequency, where amplification and signal processing are easier to perform. In addition to the magnitude of the signal, heterodyne detection can preserve phase and frequency information. This is valuable for applications such as spectroscopy and material characterisation.

The main disadvantage is the complexity of the receiver. Each channel may require a mixer, a local-oscillator distribution network, intermediate-frequency circuitry, and additional amplification. This results in a larger chip area, more power consumption, and design complexity in order to replicate these components across a large array [4], [5]. Another challenge at THz frequencies is to maintain a sufficiently strong local-oscillator signal throughout a large array while having a consistent phase.

A direct detector on the other hand converts absorbed THz power into an electrical output without retaining the phase of the incident field. It therefore does not require a local oscillator or mixer at each pixel. The resulting pixel architecture can be smaller and consume less power, while the readout can be simpler [4], [5]. These properties make direct detection attractive for large integrated focal-plane arrays.

This reduced complexity comes at the cost of losing phase information and a strong dependence on detector noise. A common sensitivity metric is the noise-equivalent power (NEP), which is defined as the input signal power that produces a signal-to-noise ratio (SNR) of 1 in a 1 Hz output bandwidth. A lower NEP represents a more sensitive detector. For passive imaging, the detector NEP must be sufficiently low to distinguish small variations in the weak thermal radiation that is received from the observed scene.

1.2.2. Cooled vs room-temperature operation

Cooling is an effective way to improve detector sensitivity because it reduces several electronic and thermal noise contributions. Bolometers and superconducting detectors can achieve very low NEP when operated at cryogenic temperatures [6]. For example, large superconducting kinetic-inductance bolometer arrays have been demonstrated for passive submillimetre-wave imaging, but such systems require cryogenic operation and are therefore less suitable for compact low-cost cameras [7].

Additional cooling equipment and thermal isolation is needed for cryogenic operation of a camera. This increases the volume, cost, power consumption, and start-up time of the system. These requirements are acceptable in some specific scientific applications but are less suitable for compact or low-cost cameras.

Room-temperature operation avoids the cooling system but it is limited by the electronic noise of the detector and readout. For an uncooled direct-detection camera, the achievable temperature sensitivity depends on the NEP, effective RF bandwidth, optical efficiency, and detector integration time [8]. A wider operational bandwidth can improve the sensitivity because the detector collects signal power over a larger frequency range. A longer integration time also reduces the measured noise, but the trade-off is that it directly increases the image acquisition time. The design of a practical camera must therefore balance detector sensitivity, bandwidth, optical coupling, spatial resolution, and imaging speed.

1.2.3. Active and passive imaging

A passive THz imaging system measures radiation that is naturally emitted by the scene or received from the surrounding environment. For this architecture, no active illumination source is required. This simplifies the illumination side of the setup and it is attractive for applications in which the use of an external source is not desirable. Passive systems are difficult to implement because objects at room-temperature generally generate very limited radiometric contrast. The detector must distinguish this small difference from its own noise and fluctuations introduced by the readout and environment [8].

An active imaging system illuminates the object with an external THz source and measures the transmitted or reflected signal. The additional power improves the signal-to-noise ratio and dynamic range. This makes active imaging more practical with room-temperature direct detectors. There have been several demonstrations of active systems using different technologies. For example, a 32x32-pixel CMOS camera operating between 0.7 and 1.1 THz was used for room-temperature active video imaging [9]. Han et al. demonstrated a 4x4 CMOS Schottky-diode array at 280 GHz and an additional single-pixel detector at 860 GHz [10]. Sengupta et al. combined a 4x4 SiGe receiver array with an integrated CMOS source at 280 GHz [11]. Room-temperature imaging has also been demonstrated using GaAs field-effect-transistor detectors [12].

Active illumination introduces additional design requirements. The source beam becomes part of the complete imaging response, so its amplitude distribution affects both coupling and image uniformity. In an FPA system, the illumination must cover the relevant pixel beams with sufficiently small variation. If the source beam is too narrow, the center pixels may be illuminated more strongly than the edge pixels. If the beam is too wide, the illumination becomes more uniform but the coupled power per pixel is reduced. The optical system must therefore try to balance between illumination uniformity, coupling efficiency, and also spatial resolution.

Both of the imaging architectures are relevant to the motivation of the new camera. Passive imaging are also important because the improved sensitivity of the new detector array was specifically developed with passive imaging in mind. However, the experimental evaluation in this thesis focuses on active imaging, because active illumination provides a controlled signal level for validating the complete measurement setup.

1.2.4. Single-pixel scanning and focal-plane arrays

A single-pixel imaging system obtains an image by measuring one spatial position at a time. In the setup that is being used, the object in the imaging plane is translated repeatedly until the desired field of view has been sampled. This approach can produce detailed images because the sampling interval is determined by the scan step size.

The main limitation is the total image acquisition time. Every spatial position in the grid must be measured sequentially, thus the number of required positions increases quickly with image size and resolution. Another factor that introduces additional settling time is the mechanical translation, which could also lead to positioning uncertainty or repeatability errors.

A focal-plane array (FPA) contains multiple detector elements that observe different spatial positions. During image acquisition, several points can be measured at the same time. The field of view is increased and therefore less mechanical scan positions are needed to obtain the full image. Large integrated arrays have demonstrated that room-temperature THz video imaging is technically possible [9]. However, increasing the number of pixels does not automatically improve the spatial resolution. The resolution also depends on the optical aperture, wavelength, detector spacing, and beam overlap.

When an array is not sampled densely enough, mechanical translation can still be used to recover additional spatial samples. Some methods can improve spatial sampling, but they require multiple measurements and therefore increase the total acquisition time. An example of this is the geometrical multi-frame super resolution method, which improved the reconstructed image from multiple shifted frames [13].

1.3. Spatial resolution and focal-plane sampling

Spatial resolution describes the ability of an imaging system to distinguish nearby features as separate objects. For an imaging system with aperture diameter D, the smallest angular resolution that can be achieved scales approximately as

$$\Delta\theta_{lim} \approx \frac{\lambda_0}{D} \tag{1.1}$$

where λ_0 is the free-space wavelength [8]. The exact resolution depends on the beamwidth definition and how well the camera can distinguish features. However, this relationship shows that a larger aperture or a shorter wavelength allows for finer angular resolution.

The aperture maps a point source to a diffraction pattern instead of an infinitesimal small point. Two nearby sources can only be distinguished if their resulting patterns are sufficiently separated. Even if the optics can support this separation, the FPA must be sampled densely enough by the detector in order to retain the available spatial information. The focal-plane sampling condition that is associated with a diffraction-limited resolution is

$$d_{f,lim} = \frac{F^{\#\lambda_d}}{2} \tag{1.2}$$

where d_f is the spacing between detectors, $F^{\#}$ is the optical f-number, and λ_d is the wavelength in the dielectric medium in which the focal plane is located [8]. The factor of $\frac{1}{2}$ appears because the array must sample both neighboring intensity maxima and also the reduction between them. If only the peak positions are sampled, there is not enough information to distinguish the two separate features.

An array with a larger spacing is undersampled relative to the diffraction limit. It could still form an image, but it would not capture all of the spatial information available from the optics in a single frame. The missing samples can be recovered by using additional mechanical positions, but it does come at the expense of longer measurement time. On the other hand, denser sampling improves spatial coverage but can reduce the size of each antenna feed and thereby lower the coupling efficiency to the optical system. The result is a trade-off between spatial resolution. imaging speed, and sensitivity. Van Berkel et al. showed that increasing the feed size can improve spill-over efficiency and imaging speed, but it also increases the sampling interval unless additional scanning is performed [8].

This distinction explains why pixel count alone does not determine spatial resolution. A large array with a wide pitch may cover a large field of view but still be undersampled at the same time. A smaller array with tighter spacing may provide better spatial detail over a smaller field of view. The ideal camera therefore combines a large number of sensitive detectors with a sufficiently small spacing between them and an optical system that preserves the corresponding beam overlap.

1.4. State-of-the-art systems

Silicon-integrated THz systems have developed in several different directions. Some systems prioritise a large number of pixels and video-acquisition, while others focus more on the detector sensitivity, operational bandwidth, or dense focal-plane sampling. The 32x32 pixel CMOS camera of Al Hadi et al. demonstrates the scalability of direct-detector arrays and their ability to achieve high frame rates while using a source for active illumination [9]. The imaging systems of Han et al. and Sengupta et al. show that detectors, readout circuitry, and sources can be integrated in silicon technologies at frequencies in the range of 300 GHz [10], [11]. Their systems highlighted the feasibility of integrated THz imaging. However, there is still a trade-off between array size, detector sensitivity, bandwidth, and focal-plane sampling.

The focal-plane architecture that was implemented by Van Berkel et al. addresses this trade-off from a radiometric perspective [8]. The sensitivity of the system improves with detector bandwidth and optical efficiency for uncooled passive operation. Increasing the feed size can improve the optical coupling, but a larger spacing reduces the instantaneous sampling density. Mechanical scanning can compensate for undersampling, although the drawback is that the effective imaging speed will be reduced.

The 12-pixel chessboard FPA developed by Hoogelander et al. was designed specifically to achieve tight focal-plane sampling while remaining compatible with integrated direct detectors [14]. The FPA was implemented in 22-nm CMOS and operated over a nominal frequency range of 200 to 600 GHz. The number of detector locations per unit area was increased by using a dual-polarised connected-array geometry. Measurements showed that this system had an aperture efficiency of approximately -4.1 dB and an average gain roll-off of approximately -1.5 dB between diagonally adjacent elements at 400 GHz [14].

The Schottky-barrier-diode detectors used in this CMOS implementation were characterised separately. Their measured system NEP reached a minimum of approximately $20\ \mathrm{pW}/\sqrt{\mathrm{Hz}}$, with a frequency-averaged value of approximately $90\ \mathrm{pW}/\sqrt{\mathrm{Hz}}$ over the characterised range [15]. This sensitivity was insufficient for the intended passive imaging scenario, so a coherent source had to be used for the imaging demonstration.

Afterwards, a dedicated quasi-optical system was developed to preserve the dense sampling of the array while providing active illumination [16], [17], [18]. The system used a silicon hyperhemispherical lens at the camera, a biconvex lens to focus the pixel beams into the imaging plane, and a separate plano-convex lens to illuminate the imaging plane from the source side. The illumination was designed to couple to all pixel beams without allowiung the source pattern to determine the image resolution.

The final system demonstrated near diffraction-limited images between 350 and 475 GHz [18]. An ivy leaf was placed inside an envelope and then imaged in transmission. The main veins appeared as regions of higher attenuation, and the spatial detail was used to demonstrate the effect of the tight focal-plane sampling. The system achieved an imaging dynamic range between 20 and 25 dB over the previously mentioned frequency range. Since the camera contained only 12 readable pixels, the object had to be mechanically translated and the sub-images were combined to form a complete image. By using a combination of mechanical translation, pixel multiplexing, and data acquisition, the total acquisition time was around one hour per frequency [17], [18].

This earlier system demonstrated the spatial-resolution advantage of the chessboard architecture, but it did not provide practical passive imaging. Its limited sensitivity required active illumination and extensive mechanical scanning was needed due to the small number of readable pixels. These limitations motivated the development of a more sensitive chessboard camera.

The newer camera is implemented in a 130-nm SiGe BiCMOS process and contains a 24-pixel chessboard FPA mounted on the base of a silicon hyperhemispherical lens with an anti-reflection coating [19]. Each antenna element is connected to a direct detector using bipolar transistors. The resulting array is a focal-plane array with dense sampling and improved detector sensitivity. The measured NEP is on the order of 10 $pW/\sqrt{Hz}$ between the frequency range of 330 to 500 GHz. The detector characterisation estimates an NETD of approximately 1.6 K for an integration time of 1 second per pixel when the full operating bandwidth is considered [19]. The measured radiation patterns agree with the simulations within approximately 1 dB.

These detector-level results do not yet establish how the improved detector performance translates into complete images. The camera must still be integrated with the optical setup, source-control hardware, voltage bias supply, readout electronics, data-acquisition hardware, positioning system, calibration procedure, and processing software. The resulting image quality therefore depends on the complete measurement chain rather than on the detector NEP alone.

1.5. Situation assessment

1.5.1. Past situation

The earlier 12-pixel CMOS camera established that a tightly sampled FPA can produce near diffraction-limited THz images [14], [18]. A quasi-optical transmission setup was developed, the camera was integrated with a multiplexed readout, and a CNC machine was used to translate the samples through the imaging plane [17]. The work also established methods for extracting the modulated detector response, compensating for variation between pixels, combining measurements from multiple scan positions, and reducing frequency-dependent standing wave effects.

The results showed that the chessboard-array concept and the optical system worked as intended. They also identified several practical limitations such as the sensitivity of the Schottky-diode detector being insufficient for passive imaging. Also, the limited number of pixels resulted in long acquisition times. Lastly, both the source and detector required careful calibration.

1.5.2. Current situation

The available 24-pixel SiGe BiCMOS camera improves the detector sensitivity and doubles the number of pixels relative to the earlier CMOS camera [19]. The camera has already been characterised in terms of responsivity, noise, and radiation patterns. The existing setup also provides the main components for active imaging, including a coherent THz source, quasi-optical lenses, readout electronics, analog-to-digital converters, and a mechanical positioning system.

This camera has not yet been evaluated as part of a complete and automated imaging workflow. A reliable software implementation must combine the hardware control, camera configuration, scanning, data storage, calibration, image reconstruction, and also visualisation. Measurements are required to determine which frequencies and integration settings together with processing methods provide useful images.

Although the detector sensitivity was developed with passive imaging as a long-term goal, this work focuses more on active imaging. Active illumination prtovides a controlled signal level and makes it possible to validate the integration of the new camera with the existing quasi-optical setup, readout chain, mechanical positioning system, and post-processing workflow.

1.5.3. Desired situation

The desired outcome of this project is an imaging system that can be operated through a controlled and repeatable workflow. The camera and supporting components should be configured from the same interface. Measurements should be acquired automatically over a defined grid, and the raw data should be stored together with the settings required to reproduce the measurement. A separate simulation interface should support the interpretation of the measured images by estimating the expected spatial resolution.

The processing method should convert the raw detector signals into spatial images while accounting for the physical pixel positions. Active images should demonstrate whether the new camera can reproduce or improve on the imaging performance of the earlier CMOS system.

The final evaluation of the camera must be able to distinguish between detector performance and system performance. It should be able to identify which limitations originate from the camera and which ones come from the remaining components such as source, optics, readout, acquisition method, calibration, or measurement environment.

1.6. Problem definition

The 24-pixel SiGe BiCMOS camera has demonstrated promising detector sensitivity, but its imaging capabilities within the complete experimental system have not yet been established. Therefore, it is unknown how effectively the camera can produce repeatable and interpretable THz images when combined with the available quasi-optical setup and measurement hardware.

The new camera cannot be evaluated by simply treating it as a replacement for the earlier CMOS camera. The new detector architecture requires suitable biasing and readout, since the increased pixel count changes the acquisition procedure. All measured outputs must be mapped correctly to their positions in the imaging plane. Standing waves, pixel-dependent responses, mechanical positioning, integration time, image-processing choices, and source-power variations can all affect the resulting reconstructed image.

The central problem addressed in this thesis is therefore the missing system-level acquisition and processing method for the new camera. Without such a method, the improved detector metrics cannot be related reliably to the image quality or acquisition speed.

1.7. Scope and boundaries

The project focuses on the integration, control, measurement, and evaluation of the existing 24-pixel camera. The design and fabrication of this camera are outside the scope of this thesis. The camera

architecture and detector are therefore treated as fixed. Their operation is explained where necessary in order to understand the measurement system, but they are not redesigned.

The main hardware boundary is formed by the available quasi-optical components, source equipment, readout electronics, analog-to-digital converters, and mechanical positioning system. These components form the experimental boundary of the project. The settings, alignment, control software, and calibration procedures may be adjusted, but the camera and main optical components are not being redesigned.

The main adjustable parameters include the imaging configuration, operating frequency, source output level, detector and readout settings, detector integration time, number of averaged acquisitions, selected pixels, readout order, scan dimensions, step size, motion sequence, pixel calibration, frequency averaging, and image normalisation.

The main measurable performance metrics include detector response, dynamic range, signal-to-noise ratio, pixel-to-pixel response variation, object contrast, spatial resolution, total image acquisition time, measurement repeatability, and stability over time and frequency.

This work will evaluate the overall performance of the complete system. The conclusions drawn for future applications are therefore limited to the technical capabilities that are demonstrated by the performed measurements.

1.8. Research questions and objective

The objective of this thesis is to implement and experimentally validate an automated acquisition and processing workflow for evaluating the active imaging performance of the 24-pixel SiGe BiCMOS THz camera. The central research question is:

> To what extent can the 24-pixel SiGe BiCMOS THz camera produce repeatable and interpretable images in an active configuration when integrated with the available quasi-optical measurement system?

This question is divided into the following supporting questions:

1. How can the camera, source, readout electronics, data-acquisition equipment, and mechanical positioning system be integrated into an automated measurement workflow?
2. How can the measured pixel responses be mapped, stored, and processed into reconstructed THz images?
3. Can the integrated imaging system reproduce an interpretable THz image of a sample, and how does this result relate to the optical reference image and resolution simulation?
4. How do factors such as integration time, frequency averaging, pixel selection, and scan settings affect image quality and the total acquisition time?

1.9. Thesis structure

Chapter 2 presents the Program of Requirements. In this chapter the project objective is translated into functional and technical requirements for hardware control, measurement automation, image reconstruction, resolution simulation, performance, and documentation.

Chapter 3 describes the Materials and Methods. It introduces the 24-pixel camera, quasi-optical setup, active measurement configurations, readout electronics, control software, calibration procedures, scanning method, and image-processing workflow.

Chapter 4 presents the measurement results. It includes the relevant system characterization, active images, resolution simulation results, and processed image outputs.

Chapter 5 discusses the results in relation to the Program of Requirements, the earlier CMOS imaging system, and the state of the art implementation. It also examines the limitations of the system, measurement uncertainties, unsuccessful measurements, and the consequences of the main design and processing choices that were made.

Chapter 6 answers the research question, summarizes the main conclusions, and provides recommendations for further development of the imaging system.

Appendix A contains image resolution results and THz image outcomes of other objects than the ivy leaf with observations.

Appendix B contains an ethical reflection on the implementation and engineering process.

Appendix C contains full size images of radiation patterns, GUI layouts, and measurement results including the results in Appendix A.

1.10. AI Acknowledgment

Generative AI tools, specifically ChatGPT and Gemini, were used during this project as a supporting tool for code debugging and text refinement. During the implementation phase, the tool was used to help interpret MATLAB error messages, suggest possible causes of software bugs, and propose improvements (safeguards) to the structure of the code. All generated code suggestions were reviewed, modified, tested, and validated before being included in the final demonstrator.

It was also used to improve the clarity and grammar of selected parts of the thesis text. References and technical claims were checked against the cited literature before inclusion. No measurement data, experimental results, or conclusions were generated by AI.

2

Program of Requirements

The goal of this project is to develop two Graphical User Interfaces (GUI's), one to control the hardware of the imaging system and the other to simulate the outcome image resolution.

2.1. Requirements for the Hardware-Control and Image-Acquistion Interface

The requirements in this subsection define the minimum functionality and system behavior needed to operate the imaging setup safely and consistently.

[1.1] The interface must provide control access to the hardware components required for THz image acquisition.

[1.2] The interface must allow the user to select and configure the hardware implementation without modifying the source code.

[1.3] The interface must initialise the selected hardware components from the stored configuration and also provide a function to test the connections before image acquisition is started

[1.4] The interface shall show the hardware status and report initialisation steps, connection-test results, configuration changes, and errors in a visible logging section.

[1.5] The interface must allow the user to define the main image acquisition settings, including the measurement name, output directory, operating frequency and frequency range, selected pixels, scan dimensions, scan step size, and CNC middle position.

[1.6] The interface shall display a live preview of the measured image during acquisition so that the user can monitor the scan while it is running.

[1.7] The interface must save the measured data together with the metadata required to interpret and reprocess the measurement, including scan settings, selected pixels, frequency settings, and acquisition settings.

The system requirements that the control and image-acquisition GUI must satisfy are as follows:

[2.1] The implementation must separate the GUI layout, hardware configuration, hardware management, instrument driver code, and image-acquisition logic into separate components.

[2.2] The instrument driver classes must implement low-level instrument communication such as VISA.

[2.3] Connection testing and initialisation must not unexpectedly enable the source output, change detector bias voltage, or move the CNC.

[2.4] The absolute CNC movements during image acquisition have to stay within safe limits and avoid resetting position.

[2.5] The interface must validate all user inputs before starting an acquisition and must stop the measurement safely when an error occurs. Invalid scan settings or missing hardware initialisation prevents the scan from starting.

2.2. Requirements for the Image Resolution Simulation GUI

For the image resolution simulation GUI the following functional requirements have been posed:

[A.1] The user must be able to specify all inputs which are needed to create an image with the frequency extender, imaging plane and camera.

[A.2] The user must be able to simulate, with the aid of the GUI, how the THz outcome image would look, based on an optical image as input, in terms of resolution.

[A.3] The GUI must show three stages of the image: (1) the optical input image, (2) the inverted black and white image, and (3) the simulated outcome picture.

[A.4] After the simulation part has finished, the final outcome image should appear in a separate figure for improved visibility.

The system requirements of the image resolution simulation GUI are determined to be the following:

[B.1] The inputs of the GUI must be logically divided into fitting categories.

[B.2] The simulation can only start once all inputs have been filled in.

The requirement for manufacturing is the following:

[C.1] The GUI layout and its working principle must be made in MATLAB

3

Terahertz Imaging System

This chapter consists of three sections. In section 3.1 the quasi-optical system for taking the THz images is introduced. After section 3.1 one has an idea of the components that are needed to make these THz images. To control those components from one place, the hardware GUI is designed. The acquisition settings that were defined before starting a measurement are given in section 3.2. What this GUI looks like and how it works will be explained in section 3.3. Lastly in the end of chapter 3 in section 3.4 the image resolution simulation GUI will be discussed. As in the section before that, the GUI layout and the working principle will be examined.

3.1. Quasi-Optical System

An overview of the complete system can be seen in figure 3.1 below. The system can be divided into three modules: the source, the QO-setup, and the read-out. Section 3.1.1 will go over the components of the source module. Section 3.1.2 will then discuss the QO-setup module. In section 3.1.3 the read-out module will be addressed. And finally in section 3.1.4, after all components in the system have been explained, a radiation pattern of three pixels is optained to determine the pixel separation.

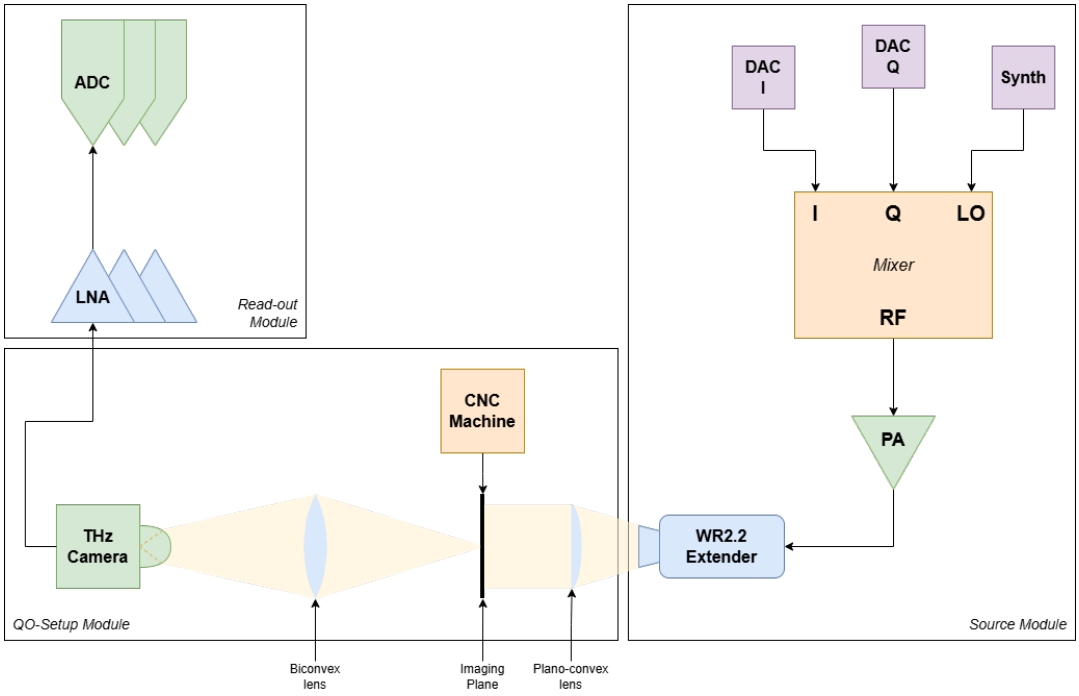

Figure 3.1: Complete overview of the THz imaging system. The large squares indicate the three modules.

3.1.1. Source module

The source module consists of two Digital-to-Analog Converters, a frequency synthesizer, an IQ mixer, a power amplifier (PA) and a WR2.2 frequency extender which covers a range of 325-500GHz. The way these components are connected to each other can be seen in figure 3.2. The frequency extender is the key component in applying active illumination in the QO imaging system. It acts as a flashlight shining from behind the imaging plane in the direction of the camera. The frequency extender has a frequency multiplication factor of 36. Thus, for an imaging frequency range of 325-500GHz, the range at the input would have to be 9-14GHz. This input frequency is provided by the Keysight N5183B synthesizer which operates as the local oscillator in the mixer component.

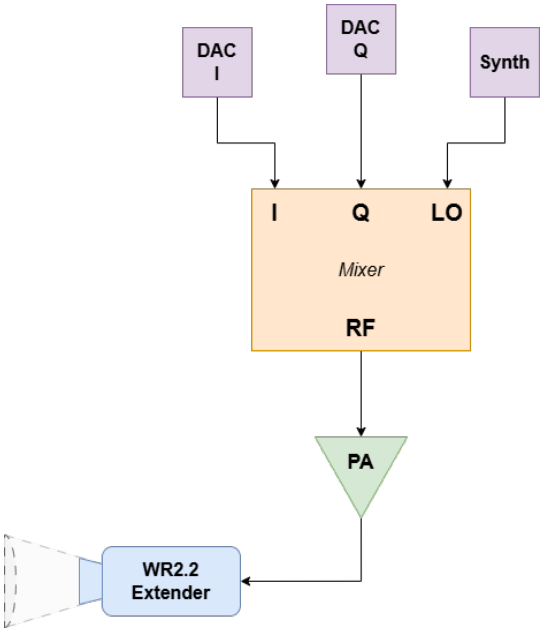

Figure 3.2: Schematic of the source module.

An important trade-off between image quality and imaging speed has to do with the integration time. The integration time is the amount of time the camera reads out one pixel. Decreasing this integration time results in faster scanning of a pixel and thus faster scanning of the whole image. A downside to this however is that white noise has a bigger influence on the SNR and decreases with that the image quality. On the other hand, increasing the integration time results in the white noise being averaged out over time and thus increasing the SNR. The downside of increasing the integration time is that scanning the whole image takes significantly longer.

Where white noise *decreases* with increasing integration time, flicker noise or "$1/f$ noise" *increases* with an increasing integration time. To lower the effect of flicker noise on the imaging signal, on-off modulation is implemented. Flicker noise is more present at the lower frequencies than at the higher frequencies. With on-off modulation the carrier signal, created by the synthesizer frequency in this case, is switched on and off with a modulation frequency f_{mod} which is much larger that the integration frequency. This on-off switching is also referred to as "*chopping*". Chopping the integration data with the modulation frequency lifts the signal to the modulation frequency when looking at the frequency spectrum. The signal is now much less affected by the $1/f$ noise since the band is now focused around f_{mod}. As a result of lowering the $1/f$ noise, the dynamic range has been significantly increased.

The IQ mixer is the component that implements the on-off modulation. The modulation frequency can be specified as an input value for the DACs. Here a modulation frequency of 100KHz is used since this achieves the highest dynamic range in this particular setup [14]. The I and Q voltage values of the DACs determine if the signal is on or off. To increase the dynamic range of the on-off modulation as

much as possible, active cancellation is applied to obtain a high quality off-state. When setting the I and Q voltages to 0, a small portion of the local oscillator signal will still get through to the output of the mixer. This phenomenon is referred to as '*LO leakage*'. LO leakage makes it that even when the I and Q voltages are set to 0, there will still be a signal coming out at the output. The active cancellation is achieved via a technique known as '*LO Suppression*'. The idea is to look for a specific combination of small I and Q voltages with which the mixer makes a small signal. This signal will have the same amplitude as the LO leaking signal, but has a phase shift of exactly 180 degrees. The phase shift of the created signal ensures destructive interference with the LO leaking signal which results in a high quality off-state. These I and Q values have been found by sweeping over the voltages and finding the local minimum of the power. First this is done on a coarse scale (steps of 0.1V), after that a finer scale (0.001V) is taken around the local minumum and the voltages are sweeped again. These I and Q voltages are different per frequency. For this reason a Look-Up Table (LUT) has been created with the needed I and Q voltages for every integer GHz frequency between 325 and 500GHz. An example of such a coarse and fine sweep can be found in figure C.3 in Appendix C. For the on-state, the Q value is kept the same while the I value is increased until it sends the extender into saturation mode. Figure 3.3 shows a sweep of the power at a frequency of 400GHz when increasing the I voltage. This is what will go into the frequency extender.

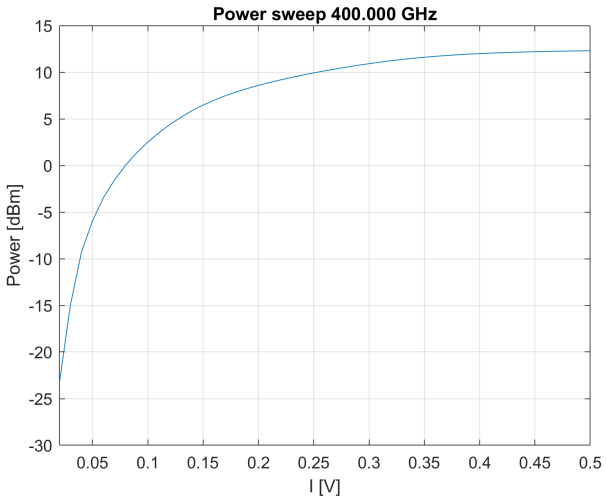

Figure 3.3: Power sweep at 400GHz frequency. For a very small value of I the power is very low. At 0.5V the power saturates.

A power sweep of the output signal of the frequency extender has been done at every integer frequency ranging from 325 to 500 GHz. The result can be seen in figure 3.4. As can be seen from the picture, the on and off signal are clearly distinguishable.

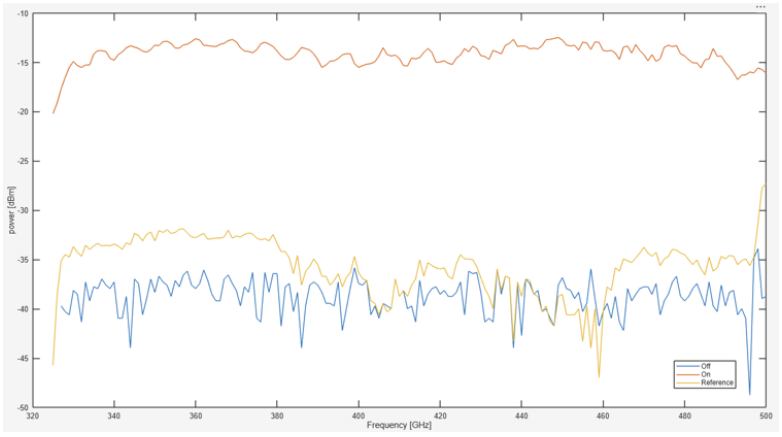

Figure 3.4: Power sweep from 325-500GHz. The red line represents the on signal, the blue line the off signal and the yellow line is a reference which is connected to nothing.

The last component of the source module is the power amplifier (PA) which is placed in between the IQ mixer and the frequency extender. The PA simply amplifies the power coming from the IQ mixer signal and sends it into the frequency extender. The gain of this amplifier is 26 dB [20].

3.1.2. QO-setup module

Once the THz waves are created and emitted from the frequency extender, they enter the QO-setup module. This module consists of a CNC machine, a planoconvex lens, a biconvex lens, the camera and the object to be imaged. The ordering of components can be seen in the schematic in figure 3.5.

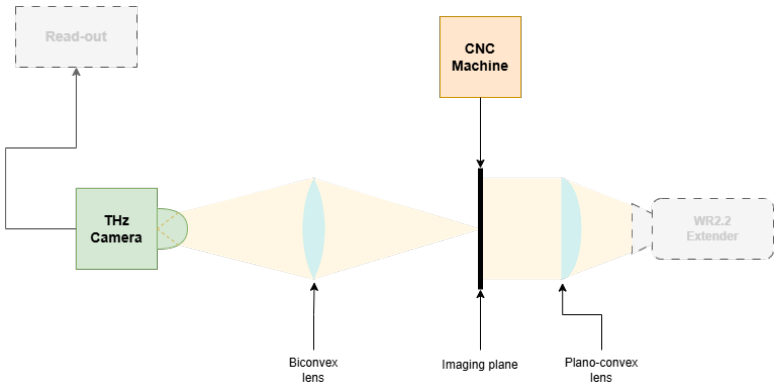

Figure 3.5: Schematic of the QO-setup module. The waves travel from right to left from the frequency extender, through the planoconvex lens, the imaging plane (where the object is located), through the biconvex lens, and finally ends in the camera where it is then read out by the read-out module. The yellow parts in between represent the path of the traveling waves.

Starting from front to back, the waves coming from the frequency extender first go through the planoconvex lens. The task of the planoconvex lens is to make a collimated beam of the waves coming from the extender. A collimated beam hitting the imaging plane would ensure an as uniform as possible illumination of the pixels. It is placed on a 3D-printed mound which is connected to the mount of the frequency extender. An image of this can be found in figure C.6. The f-number of the planoconvex lens is chosen to be $f_{pc} = 1.48$ since this shows maximum aperture efficiency [17].

The SiGe camera consists of 24 pixels. This is too small to make a somewhat detailed image of an object. To account for the lack of pixels, the object in question is moved in a plane called the *imaging plane*. By moving the object based on its pixel separation and taking a picture of a certain region, one can make a many pixel image from using few pixels. To move the object in the imaging plane a CNC is used. To attach the object to the CNC the object is placed in an envelope. The CNC model used in this setup is the Colinbus Laboflex-30 which has a μm displacement accuracy.

After the THz waves traveled through the object they are focused by the biconvex lens onto the hyperhemispherical lens of the camera. The biconvex lens has two different f-numbers for the two sides. The f-number on the side of the camera is 2.12 while the f-number on the imaging plane side is equal to 2.5 [17]. The hyperhemispherical lens on the camera focuses the radiation even more and onto the antennas of the FPA which is attached to the back of the hyperhemispherical lens.

3.1.3. Read-out module

After the radiation waves have been captured by the camera, the data signal coming from a single pixel is sent to the read-out module. The read-out module consists of two types of components: the LNAs and the ADCs. As can be seen in figure 3.6, the signal first gets amplified by an LNA before it is read out with an ADC. The reason for there being three LNAs and three ADCs in the schematic is that due to practical considerations only three ADCs can be used simultaneously. If all 24 pixels were to be used for the imaging, a switching system would have to be implemented [17]. For the sake of simplicity this switching system has been left out and each of the three pixels has its own LNA and ADC channel.

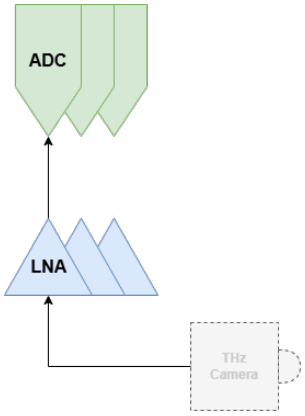

Figure 3.6: Read-out module schematic. The signal from the camera is sent through the LNA and ends in the ADC. Each pixel used in this report has its own LNA and ADC channel

According to the gain vs frequency plot, see figure 3.7b, the gain of the LNA is roughly 40dB.

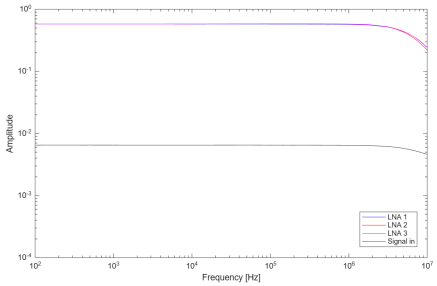

(a) Amplitude vs frequency plot. The black line is the input signal. The colored lines are the LNAs.

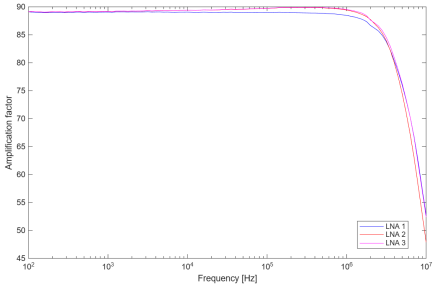

(b) Gain vs frequency plot. The amplification factor for the LNAs is around 90. This comes down to ∼40dB.

Figure 3.7: Two plots from performed LNA measurements

After the signal has been amplified by the LNA, it is digitized by the ADC. The value of the signal represents the outcome of the scan of one pixel at a certain frequency from the frequency extender. These values, when placed together accordingly to the movement of the CNC, make the final THz outcome image.

3.1.4. Radiation Pattern

Once all components had been calibrated and were connected into the system, a scan of the radiation pattern coming from the frequency extender was made. The corresponding I and Q voltages, which are different for each frequency, were obtained from the LUT discussed in section 3.1.1 and set as inputs for the DACs.

The created radiation pattern is a mapping of the three pixels together. To see how waves would travel through the focusing lens, the frequency extender was moved parallel to the plane of the lens over the whole surface. To move the frequency extender over the same plane as the lens, it was attached to the CNC before being set in place in the final setup. The face of the horn of the frequency extender was located at the same distance from the lens as where the envelope, which contained the object, would be. The patterns have been measured from 330GHz to 500GHz in increments of 10GHz. From the mapping of the three pixels the pixel separation could be determined. This was found to be 1.5mm. The created radiation pattern at a frequency of 400GHz can be found in figure C.1 in Appendix C.

3.2. Acquisition settings

The acquisition settings that were defined before starting a measurement can be seen in Table 3.1. Before each measurement, a common set of acquisition settings was defined in the measurement interface. These settings determined the selected camera pixels, source frequency configuration, detector readout, CNC scan grid, and data-storage parameters. The same general configuration was used for both the image-acquisition measurements and the radiation-pattern measurements, while the scan region and measurement objective were adjusted depending on the experiment. Table 3.1 summarizes the main settings required to reproduce the measurements.

Table 3.1: Overview of the acquisition settings used during the THz imaging measurements.

Parameter	**Setting or description**
Measurement type	Active THz measurement.
Camera	24-pixel SiGe BiCMOS THz camera.
Selected readout pixels	Three camera pixels measured simultaneously
Displayed pixel	One selected pixel used for the main reconstructed result
Source configuration	Synthesizer and frequency extender used as illumination source
Source frequency	Selected from the interface depending on the measurement
Frequency sweep settings	325 to 400 GHz for radiation-patterns, 398 to 402 GHz for the ivy leaf
Source output power	Synthesizer output power set before acquisition.
IQ mixer control	DAC voltages selected from the frequency-dependent lookup table
Detector bias supply	Bias voltage supplied by the Keithley source: $V_{bias} = 0.75$ V
Readout chain	LNA outputs connected to the data-acquisition hardware.
Integration time	Acquisition time of $t = 10$ ms
Scan range	90x90 mm for ivy leaf, 60x60 mm for radiation patterns
Scan step size	1.5 mm in both dimensions
Grid size	3721 grid positions per frequency
CNC movement mode	Target positions generated from center position and scan-grid
Saved metadata	Frequency settings, selected pixels, scan settings, acquisition settings, and measured detector responses
Image reconstruction	Measured detector responses mapped to the CNC positions
Post-processing	Detector response converted to dB and normalized to the maximum value in the reconstructed image

Unless stated otherwise, the same hardware configuration and acquisition settings were used for both the radiation-pattern measurements and the image-acquisition measurements. The difference between the two was the selected scan region and the interpretation of the reconstructed spatial response.

3.3. Hardware Control and Image Acquisition Interface

The imaging setup contains several independently controlled instruments including the signal generator, IQ mixer control DACs, camera supply, ADCs, and the CNC positioning system. Operating these instruments manually would require the user to configure multiple software interfaces and execute the measurement steps in the correct order. This approach is prone to errors and would increase the probability of inconsistent settings, incomplete measurements, potentially unsafe positioning commands, and measurement results that are difficult to reproduce. Therefore, a GUI was developed in MATLAB to provide a single control environment for configuring the hardware, testing communication, defining measurement parameters, and monitoring the image acquisition.

The hardware-control GUI was developed with four main objectives that are defined in chapter 2. In particular, the GUI had to control all the hardware required for image acquisition, allow the user to select and configure the connected instruments, test communication before a scan, define the acquisition settings, and store the resulting data with sufficient information for post-processing. The implementation is therefore focused on reproducibility, modularity, and safe operation rather than only on visual convenience. This design of the GUI directly addresses requirements [1.1], [1.2], [1.3], [1.5], and [1.7].

The resulting application consists of a hardware-configuration interface and a separate image-acquisition interface. The first tab is used to select, configure, initialise, and test the connected instruments. The second tab is used to define the measurement grid, set the middle position of the CNC, start the scan, and inspect the live image preview. Figure 3.8a shows the final layout of the hardware-configuration interface, and Figure 3.8b shows the final layout of the image-acquisition interface.

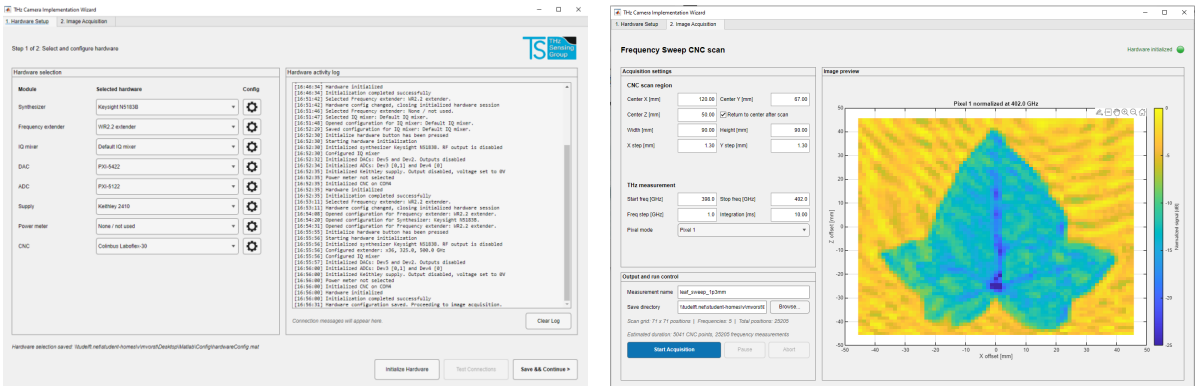

(a) Hardware-selection tab of the GUI

(b) Image-acquisition tab of the GUI

Figure 3.8: Interface for both hardware-selection and image-acquisition

3.3.1. Software architecture

The hardware-control and image-acquisition routines were divided over multiple MATLAB files to keep the implementation organised and maintainable. Instead of placing the GUI layout, hardware communication, configuration handling, and measurement logic in a single script, each file was assigned a specific task.

The main GUI file manages the user interface, while the hardware-configuration files store and load the selected instruments. The hardware-manager file creates and connects the corresponding hardware objects that are used throughout the process. The image-acquisition file performs the actual scan sequence. This separation makes the code easier to extend when new hardware is added or replaced and it reduces the chance that changes in the interface affect the measurement process.

The GUI interface itself was implemented as a standalone MATLAB class named *THzCameraWizard*. The state of the selected hardware must be available throughout the process, so a class-based implementation was selected rather than a procedural script. Additionally, the active connections, user-interface components, acquisition settings, and measurement results are also retained throughout the session. A procedural implementation would require these states to be passed manually between

many separate functions, which would make the code more difficult to maintain and could result in an inconsistent state between functions.

The software was divided into four functional layers:

1. Graphical user interface (GUI)
2. Hardware configuration
3. Hardware-management layer
4. Classes for instrument drivers and acquisition

The GUI layer is responsible for displaying the controls, reading user input, validating measurement settings, logging hardware status information, and plotting the acquired image. It does not contain the low-level communication commands for every instrument, since those are located in the driver classes for each respective instrument. This separation was introduced to satisfy [2.1] and [2.2], which indicated that the hardware configuration, hardware management, instrument driver code, and acquisition logic must be separated into distinct software components.

The hardware configuration is stored separately from the interface layout. Default configurations for the available instruments are defined by the *defaultHardwareOptions()* method. The settings for all the instruments such as VISA address, serial port, bias voltage, or calibration-file location are stored in a settings schema. This schema can be retrieved by using the *getSettingSchema()* method. The GUI can then generate the appropriate configuration that is needed for the selected hardware, without having to hard-code all the device-specific settings into the main interface.

The selected hardware and its settings are stored in *hardwareConfig.mat*, which allows for the same setup to be restored in later MATLAB sessions. This design satisfies [1.2], because the setup can be stored, restored, and edited without changing the acquisition process.

The *HardwareManager* is responsible for constructing the appropriate driver objects and managing the active connections. Each time the GUI is closed, the connections with the instruments are closed so that they are ready for a new session.

The final layer consists of the separate instrument classes, such as the signal generator, power-supply, DAC, ADC, and CNC drivers. The image acquisition itself is performed through a separate class called *THzImageAcquisition*.

This separation prevents the interface from becoming dependent on one specific hardware configuration, and it allows the user to test different parameters for the acquisition. Another advantage is that an individual driver can be tested independently before it is connected to the complete application. This also supports requirement [2.1], since the acquisition sequence is implemented separately from the GUI layout.

3.3.2. Hardware-selection interface

The first tab of the GUI is used to select and configure the available laboratory equipment. Each hardware category is shown in a separate row containing its name, a drop-down menu, and a configuration button. The drop-down menu selects the driver or hardware implementation, while the cogwheel opens the settings belonging to that selection. This structure satisfies [1.2], since each hardware category can be selected through the interface and configured through a component-specific settings dialog.

The hardware categories represented in the final configuration include the following:

- Synthesizer
- IQ mixer control
- DAC channels
- ADC channels

- Detector bias supply
- CNC positioning
- Supporting source or readout components

The configuration dialog is created from the selected component's settings schema. This allows different instruments within the same category to request different input parameters for the configuration. For example, a GPIB-controlled instrument requires a VISA resource address, while the CNC controller requires a communication port and motion-related settings. Additionally, the detector supply configuration contains the required bias voltage. The IQ mixer configuration prompts the user to specify lookup-table file, since these calibration values are specific to the source and modulation system rather than to a single image scan. An example of a configuration window can be seen in Figure 3.9.

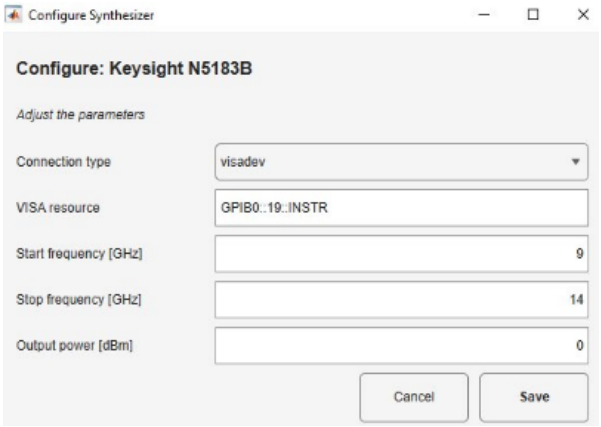

Figure 3.9: Configuration window of an instrument

The hardware tab also contains separate Initialize Hardware and Test Connections buttons. These were placed because connection management is part of the system preparation and should be completed before an image scan is done.

The Initialize Hardware function reads the saved configuration, creates the selected driver objects, and establishes the required communication interfaces. The Test Connections function checks whether the created objects respond correctly. Separating these actions is useful during troubleshooting, since the user can distinguish between an error in object configuration and a failure of an already established instrument connection.

A logging panel on the right side of the interface reports any actions that are carried out by the application. This includes the start and outcome of hardware initialisation, connection tests, configuration changes, and errors that are returned by the instrument drivers. The log was added because a single status lamp does not provide enough information to identify which device failed or during which step the error occurred. The previously mentioned functions satisfy requirements [1.3] and [1.4].

3.3.3. Instrument driver classes

Every remotely controlled instrument is represented by a separate MATLAB driver class. The driver translates the high-level requests from the acquisition process into the communication commands required by the physical instrument. This approach creates a common boundary between the GUI and the hardware. The interface only needs to know which operations are available, such as connect, disconnect, configure, enabling or disabling output, setting frequency or voltage, measuring output, or moving the mechanical position. The exact method names differ between drivers, but the principle remains the same. The GUI uses meaningful hardware operations rather than directly transmitting the command strings. This satisfies requirement [2.2], since low-level instrument commands are implemented inside hardware driver classes instead of inside the GUI.

3.3.4. Communication and connection testing

Instrument communication was implemented using MATLAB's instrument control functionality. VISA-based devices are accessed through `visadev`, which supports interfaces such as GPIB, USB, serial, and TCP/IP [21]. The communication address for the instrument is obtained from the saved hardware configuration.

During initialisation, the corresponding driver class creates the communication object and applies the configured settings. By using queries, the code can confirm whether the configured address points to the intended device. Another way to test the hardware connection is by using a status or measurement query.

The connection test must not alter anything in the experimental setup. Therefore, it avoids actions such as enabling the THz source, changing the detector bias voltage, or moving the CNC. A successful connection test only confirms that communication has been established and that the selected driver is actually compatible with the hardware instrument. This satisfies requirements [1.3] and [2.3].

Any errors that are generated inside a driver class are passed back to the HardwareManager and displayed in the GUI log. This enables the user to observe device-specific error information and handle it accordingly.

3.3.5. Safe hardware initialisation

A pre-defined initial hardware state is important because several devices retain their previous settings after a MATLAB program has been stopped. The initialisation sequence was therefore designed to establish communication before activating any of the outputs. The general initialisation sequence is:

1. Load the saved hardware configuration
2. Create the required driver objects
3. Open the communication interfaces
4. Verify the instrument connections
5. Configure the requested ranges and operating parameters
6. Apply the camera bias settings
7. Load the IQ mixer calibration lookup table
8. Make sure controllable source outputs are disabled until the measurement starts

This sequence prevents the source from being enabled before the synthesizer frequency, output power, and IQ mixer voltages have been configured. It also ensures that the bias supply is operated using the voltage and range that is expected by the detector system.

At the end of a measurement, or when the acquisition is aborted due to an error, any outputs should be returned to a safe state. In particular, the RF output and detector bias output must not remain active. To ensure this happens, a safe shutdown call is made to each instrument and they are handled by the hardware driver classes. This satisfies requirements [2.3] and [2.5], because outputs are not enabled unexpectedly and the system is returned to a safe state if the acquistion process is interrupted.

3.3.6. Image-acquisition interface

The second tab of the GUI contains the controls required to define and execute an image scan. It combines the measurement parameters, CNC scan settings, output directory, hardware status, and also the live image preview in the same interface. The main input parameters are:

- CNC center position coordinates
- Scan width and height
- Horizontal and vertical step size
- Operating frequency or frequency range
- Detector integration settings

- Selected detector pixels
- Measurement name or file prefix
- Output directory

The CNC center position is used as the reference point from which the scan grid is generated. The acquisition routine calculates the required target positions from this center position, the selected scan dimensions, and the horizontal and vertical step sizes. The resulting positions are then checked against the CNC limits before mechanical motion is started. During image acquisition, the software does not issue any coordinate-reset commands. This ensures that the scan is performed using absolute target positions and satisfies requirement [2.4].

The calculated scan grid and total number of measurement positions are displayed together with the output information. This allows the user to inspect the size of the measurement before starting the scan. Additionally, there is a pause button in case the user needs to make some final adjustments to the setup before continuing with the measurement. There is also an abort button to stop the current acquisition. These acquisition parameter fields satisfy requirement [1.5].

A live image preview is displayed on the right side during the scan. The preview is updated as new spatial positions become available. It also includes a color bar so that the displayed magnitude can be interpreted. The preview is normalized every time it updates, so the color bar scales with the measured transmission values. This plot is intended as immediate measurement feedback rather than as a final processed image. The live preview satisfies requirement [1.6] by giving the user an idea of what is being measured while the scan is still running.

3.3.7. Link between GUI and acquisition logic

The entire measurement procedure is implemented in THzImageAcquisition.m. The start acquisition button reads and validates the GUI fields, makes a structure for the acquisition settings, and passes this structure together with the connected hardware objects to the acquisition class. This approach satisfies requirement [2.1], because the acquisition seuqency is implemented separately from the GUI layout and hardware-configuration logic.

This separation was selected for three reasons. First, the same acquisition procedure can be executed without the GUI during debugging. Second, the measurement sequence remains the same independent of changes to the visual layout. Third, the GUI remains focused on status and plotting updates instead of containing one large hardware-control block. The acquisition class coordinates the following operations:

1. Validate the requested measurement settings
2. Configure the signal generator and source-control system
3. Configure the detector bias and readout
4. Calculate the required grid positions
5. Move the CNC to the next absolute position
6. Acquire the detector signals
7. Extract and store the detector responses
8. Update the live preview
9. Repeat the procedure for the remaining positions and frequencies
10. Save the result and measurement metadata
11. Return the hardware to its safe output state

The exact source and readout sequence is described in 3.6, where the modulation, ADC acquisition, pixel readout, and detector-response calculation are discussed.

3.3.8. Data storage and measurement metadata

Each measurement is saved as a MATLAB data file. The saved result structure contains the measured image data together with the settings used to perform the measurement. The stored metadata includes:

- Measurement name and output path
- Frequency or frequency range
- Selected pixel mode
- Scan dimensions and step sizes
- Physical grid coordinates
- Camera bias settings
- Source settings
- Acquisition and integration settings
- Hardware configuration
- Raw detector responses
- Reconstructed image values

By saving these values together with the image, the user can reprocess the image without repeating the complete scan. Additionally, the displayed matrix alone does not identify the pixel spacing, measurement frequency, or detector configuration. Saving the measurement data together with the scan and hardware metadata satisfies requirement [1.7].

3.3.9. Input validation and error handling

The GUI validates the user input before allowing an acquisition to start. For example, numerical input fields must contain finite values within the supported operating range. Scan dimensions and step sizes must produce a valid number of positions. An output directory must be selected, and the CNC steps must be within its limits before any mechanical motion is allowed.

The hardware status is shown in the top right of the acquisition tab using a visual indicator along with a label. The user can confirm whether the initialisation has been completed without having to return to the hardware tab. The connection controls for the instruments remain on the hardware tab in order to preserve a clear separation between setup preparation and measurement execution.

These checks satisfy [2.5], because image acquisition is prevented when the hardware is not ready or when invalid acquisition settings have been entered by the user. If any error occurs, the acquisition is stopped and the message is reported through the GUI logging area. Hardware outputs are then disabled and partial data is saved in order to diagnose the failure.

3.3.10. Main design choices

A dedicated hardware-control interface is more than just operating the instruments through separate scripts. The number of interacting components and the need to perform long, repeated image scans introduces a level of complexity that needs to meet the set requirements. The final design choices were made with these requirements in mind and to reduce the probability of user errors during the measurement. The main design choices were:

- **Class-based GUI:** retains the application state and allows the hardware objects, settings, and interface components to be managed within one application.
- **Configuration schemas:** allow the configuration interface to adapt to the selected hardware implementation.
- **Persistent configuration file:** reduces repeated setup work and ensures that selected instruments and settings can be restored.
- **Separate `HardwareManager`:** object creation, connection management, hardware availability.
- **Separate acquisition class:** keeps the imaging method independent of the GUI layout

- **Connection testing and logging:** make hardware errors visible before a long scan is started.
- **Live image preview:** allows detection of incorrect positioning, missing signal, saturated readouts, or unexpected image patterns during acquisition.
- **Measurement metadata storage:** links saved data to the settings used to acquire them.

These choices transformed the original collection of instrument-specific control procedures into a repeatable imaging workflow. Another user can select the configured hardware, initialise the devices, define a scan grid, and execute the same acquisition sequence without having to manually adjust anything in the code.

3.4. Resolution Simulation Software

With a pixel separation of 1.5mm, the SiGe camera is very limited in resolution compared to optical cameras nowadays. Because of this limitation, it can be beneficial to know beforehand if scanning the object with THz frequencies will give a useful outcome or if certain details of the object lack due to the limited resolution. To estimate the effects of the pixel separation, a tool, referred to as the '*resolution simulation software*', has been developed. With the aid of the single pixel radiation pattern of the camera and an optical image of the object, the tool estimates what the outcome picture will look like based on the step size in the imaging plane. An example of a single radiation pattern at a frequency of 400GHz is shown in figure C.2. This means that it can estimate the outcome of the picture based on the pixel separation, but also the outcome of coarser scans in terms of step size. As stated in requirement [A.2], the GUI that has been created will aid the user in making THz images. Section 3.4.1, 3.4.2 and 3.4.3 go over the practical design choices of the layout. In section 3.4.4 the actual working principle is explained. And finally in section 3.4.5 the purely optical nature of this resolution simulation software is emphasized. Since the programming environment used by the Terahertz Sensing Group is MATLAB, the GUI is also designed in MATLAB as mentioned in requirement [C.1]. MATLAB has excellent GUI building capabilities with its app designer tool to build apps interactively. This GUI however, has been built programmatically by using MATLAB functions to improve refined customization of the layout.

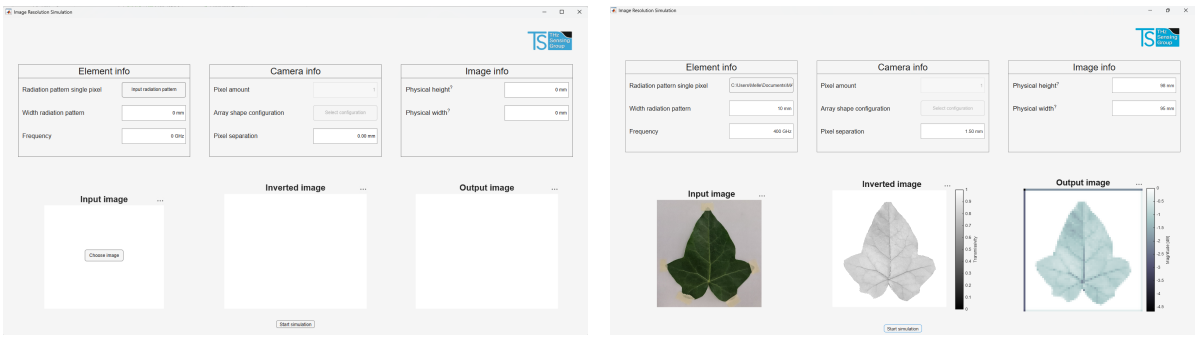

(a) Resolution simulation GUI layout at start-up

(b) Resolution simulation GUI layout after simulation

Figure 3.10: The resolution simulation GUI layout at start-up and after simulation

3.4.1. Input Definitions

Figure 3.10 shows what the resolution simulation GUI looks like at start-up and after the simulation is completed. The inputs of the GUI are categorized in three parts ([B.1]): the element info, the camera info, and the image info.

The element info block contains the input file of the radiation pattern of a single pixel. A '.fig' file can be selected as a file from the computer. Once selected, the user can hover the cursor over the button to view the complete file name for verification. Each radiation pattern has a certain maximum deviation from its center. This deviation from left to right, or top to bottom assuming the radiation pattern is square shaped, is what is described as the width of the radiation pattern in mm. This width shall be of importance in the working principle. The last element of the element info box is the frequency, whose units are in GHz.

The camera info block contains elements concerning the physical properties of the camera. The pixel amount is the amount of pixels the camera will use for the scan. The amount has been locked in at a single pixel. Simulating with a single pixel takes away deviations in magnitudes for the different pixels, which as a result ensures uniform images. In future experiments with this imaging setup this value could be changed to the amount of pixels used for the scan. Important to notice is that when eventually simulating the outcome using multiple pixels, the input radiation pattern should have the corresponding amount of pixels. Where these pixels are located with respect to each other can then be selected at the 'array shape configuration' point. Lastly, the pixel separation can be defined in mm. This will determine the step size in the simulation process.

The last category, the 'image info', contains two characteristics regarding the optical image: the physical height and the physical width of the optical picture of the object. Say an object is 100mm long and the optical picture includes both 10mm of the background at the top and bottom, then the physical height would be 120mm. These are important to determine the final outcome resolution based on the pixel separation. The amount of steps one can take based on the physical size and the pixel separation is what determines the resolution of the final outcome picture. More on this will be explained in section 3.4.4. All the inputs mentioned above are needed to simulate an image and thus requirement [A.1] is met.

3.4.2. Image Evolution

Requirement [A.3] states that three images need to be shown in the GUI: one for the input image, one for the inverted image, and one for the final outcome image. As can be seen in figure 3.10, the bottom half of the GUI layout contains these three spaces for images. An input image can be selected from files by pressing the 'Choose image' button. This image is going to be the optical image of the object one wants to scan. Recommended is to take the optical images without a flash. This is due to the fact that a flash will bring unwanted outcome in the image processing.

Once the optical image has been selected, the inverted picture in the middle will appear as well. To arrive at the inverted image, the optical image is grayscaled first and converted into doubles. This is important so that the pixel values of the optical image can be used as a scaling factor in the simulation process. This will be elaborated on in section 3.4.4. To be able to compare the simulated outcome pictures to the actual taken pictures by the imaging system, the grayscaled image is inverted. Inverting the image ensures that the veins will appear darker compared to the leaf parts around them. This coincides with the final outcome pictures from Van Dijk [17]. Inverting the image does result in a black background due to the envelope holding the leaf being white inside. To closely resemble the form of the desired outcome pictures, the pixels below a certain value were put to the maximum pixel value. This has it as a result that the black background is turned white. The value from which the pixels are set to the maximum pixel value is determined by trial and error. In this step a pixel value of 0.47 or lower is converted into a 1.0. An example of an optical image and its adapted inverted image can be seen in figure 3.10b. The inverted image is what is used to simulate the final outcome image. The final outcome image on the bottom right appears once the simulation has been completed.

3.4.3. Fault Preventive Measures

Since simulating an image takes multiple minutes, the GUI should prevent the user from erroneous results as much as possible. To make sure the right file types are filled in for both the radiation pattern and the optical image, the possible file types for selection have been restricted to *.fig*-files and *.jpg, .jpeg, .png*-files respectively. To improve user-friendliness, the GUI has been implemented with several pop-up notifications. It is important that all inputs have been specified before the simulation starts to obtain usable results at the outcome ([B.2]). In case the user tries to start the simulation before every input has been given, a pop-up screen appears indicating which input is missing. The simulation can only start when all inputs have been given.

Once the simulation has started, a loading bar will appear to show the user that the simulation is in operation. A cancel button has been added to the loading bar in case the user wants to cancel the simulation. When canceled, the user will be notified via a pop-up screen and brought back to the GUI. If not canceled, the simulation will run till completion. Once the simulation is completed, a confirmation

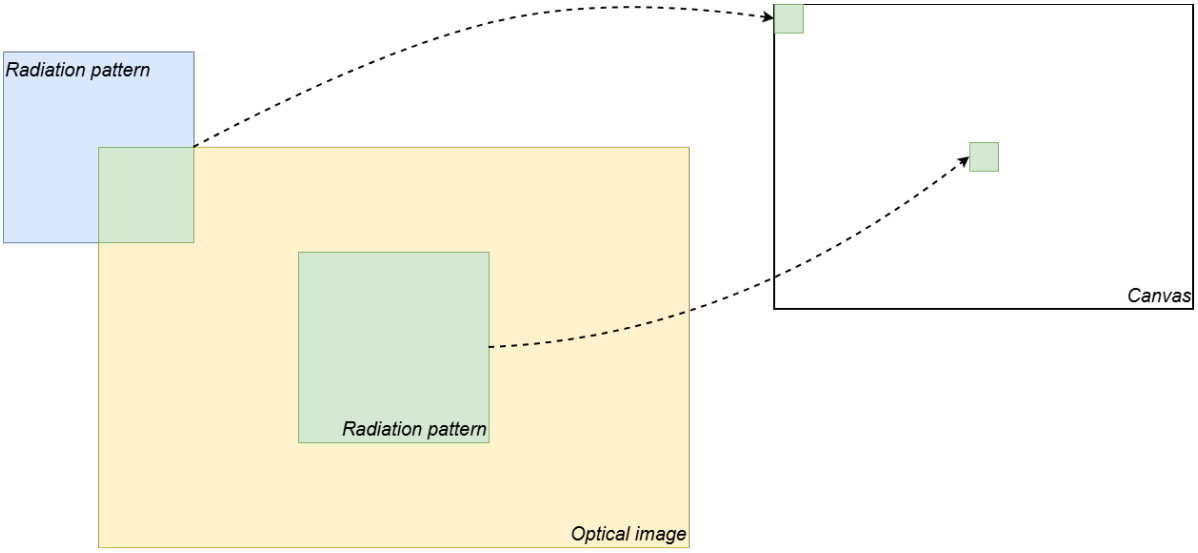

Figure 3.11: Schematic of working principle of the resolution simulation software. The yellow rectangle being the optical image, the blue square the radiation pattern, and the green part where they overlap. After computation a newly created pixel value is placed in the corresponding spot in the canvas on the right.

pop-up appears indicating how long the duration of the simulation was. Together with this pop-up a separate figure with the simulated outcome image will appear, the reason for this figure being improved visibility ([A.4]). Once the simulation has been completed, the user can close the GUI via a confirmation pop-up.

3.4.4. Simulation Principle

The resolution simulation software consists of two separate files. One file is for the layout and interactivity of the GUI. This is what has been discussed in the previous sections of section 3.4. The other file is called upon in the end from the GUI file once the 'start simulation' button has been pressed. This file is the actual working principle of the resolution simulation. This section is a walkthrough of this working principle.

The simulation process starts with assigning the entered numeric values from the user to their corresponding variable in the code. After this has been done, the pixel size of the optical input is obtained. Next, a *meshgrid* is made. A meshgrid in MATLAB turns a 1D array into a 2D or 3D coordinate matrix. This grid goes from 0 to the physical size in mm in a total amount of steps which is equal to the pixel size. This goes for both x and y direction when looking at the optical image as a 2D plane. Similarly, the data from the radiation pattern file is obtained together with its pixel size. Again a meshgrid is made is a similar way. The grid from the radiation pattern goes from minus half the radiation pattern width (GUI input) until plus half the radiation pattern width. Defining the grid this way has it that the coordinate $(x, y) = (0, 0)$ is located in the middle of the radiation pattern. The meshgrids of both the image and the radiation pattern are later used in an interpolation function in a loop.

Depending on the defined pixel separation, the pixel can only take a discrete number of steps over the optical image. The pixel size, and with that the resolution, of the simulated outcome image depends on this amount of steps. To obtain the outcome dimensions of the simulated image, the pixel size in both x and y direction is obtained by dividing the physical dimensions by the pixel separation. With these calculated dimensions in x and y direction a matrix of zeros is made. This matrix will be referred to as "*the canvas*". The canvas forms the framework of the final outcome image which is created pixel by pixel starting from an empty frame, similar to a painter and its painting.

Before a loop is started to create pixel by pixel, the radiation values from the pattern are converted from dB to linear to allow multiplication with the pixel values of the optical image later on. Figure 3.11 shows

a schematic of how a pixel value is calculated and how the loop will operate. The center of the radiation pattern is placed over the top left pixel of the optical image via an interpolation function. Via this interpolation function, both the values outside of the radiation pattern and outside of the optical image pixel boundaries are set to 0. The next step is to multiply the overlapping values. These values are then integrated and converted to dB scale. This dB value is subsequently placed into the top left of the canvas and represents the first pixel value of the outcome image. Once the first pixel has been placed, the radiation pattern moves to the right with the specified pixel separation. The interpolation function in the next iteration of the loop works with a relative location of the radiation pattern when looking in the optical image plane. The same steps as above are then repeated. The scans are made from left to right before moving down one step with the pixel separation until all values of the canvas have been filled.

Once the canvas has been filled, the values of the canvas are normalized by subtracting its maximum value from all elements of the matrix. The outcome image is then placed in the GUI and in a separate figure for improved visibility by using the *imagesc* function. Both images are plotted in colors from the 'bone' spectrum. This is to compare the simulation results to the actual image data, which will also be plotted in bone colors, following the outcome image style from Van Dijk [17].

3.4.5. Simulation vs Ground Truth

An important thing to keep in mind is that the image resolution simulation software will not show the expected outcome picture from the ground truth (actual THz image). The simulation software is created to give the user an idea what the picture would look like in terms of resolution. Resolution here translates to the coarseness of the pixelized image. Having a larger pixel separation results in less steps over the optical image and thus a coarser outcome image. Similarly, a smaller pixel separation translates to more steps over the optical image and thus a better resolution of the outcome image.

A thing the resolution simulation software does not take into account is the material of the object and the absorption properties of that material. Darker spots in the THz image arise from the lack of radiation arriving at the camera compared to brighter spots in the THz image. The lack of radiation in certain parts, in the case of a leaf, is due to water inside the leaf absorbing the radiation coming from the frequency extender. These transmissive and absorbing properties of materials can not be taken into account in the resolution simulation software. An example can be seen when looking at a public transport card as shall be demonstrated in section A.2. The simulated outcome image of the resolution simulation software would be the outside of the card. When placing the card in the THz system, the outcome image would be very different. The THz waves would easily travel through the paper of the card, but will be absorbed by the metal chip inside. In the outcome image of the system, the details on the card will not be visible. Instead, the metal chip inside will be exposed. This is something that can not be done from an optical image. The dB scale next to the simulation outcome image therefore does not correspond to the dB scale of the THz image outcome.

4

Results

This chapter presents the results of the active THz imaging workflow. First, the reference image of the ivy leaf sample is shown. This image is used as a reference for the location of the leaf features. The expected spatial resolution is then evaluated using the resolution-simulation interface. After this, the acquired THz images are shown, including the raw and processed image outputs.

The goal of this chapter is to present the measured outcomes. The interpretation of the observed image quality, limitations, and differences with respect to previous work is discussed in chapter 5. Additional objects were also measured during the project. These measurements are included separately in Appendix A, together with a brief discussion of their results.

The imaging performance was validated using a leaf sample, which was selected because it contains structures with different expected THz transmission levels. In particular, the main veins contain more water than the surrounding leaf surface, so they are expected to absorb the transmitted signal more strongly. The sample therefore provides a useful test object for evaluating whether the imaging system can reconstruct spatial transmission contrast. It also allows for a comparison between the measurements done with the previous camera.

The main result presented in this chapter is a reconstructed active THz transmission image of the ivy leaf sample at 400 GHz, together with a frequency-averaged version obtained from the measurements around this frequency. The results are presented in terms of the visible leaf features, the expected spatial resolution, the final acquisition settings, and the observed improvement after frequency averaging. The radiation pattern used to estimate the spatial resolution can be found in figure C.2.

4.1. Reference image

The reference image of the leaf sample that was captured using a phone camera can be seen in figure 4.1. This image is not used as a quantitative optical measurement, but only as a visual comparison for the spatial location of the leaf features. The optical image shows the central vein running from the stem towards the leaf tip, together with several secondary veins extending towards the leaf edges. These features are used for a qualitative comparison with the reconstructed THz image. The scan covered a region of approximately 90 mm by 90 mm, which includes the complete leaf and a small surrounding background region.

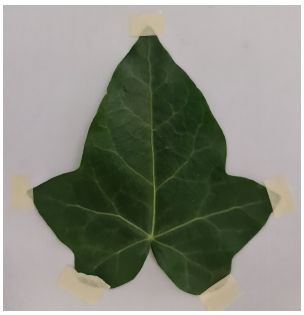

Figure 4.1: Optical reference image of the leaf sample.

4.2. Resolution-simulation result

The resolution-simulation interface was used to estimate the expected spatial resolution for the imaging configuration. In the simulation, the same frequency and sampling settings were used as the measurement. The result provides a reference level of spatial detail that can be expected from the acquired image. Figure 4.2 shows the output of the resolution simulation at different frequencies.

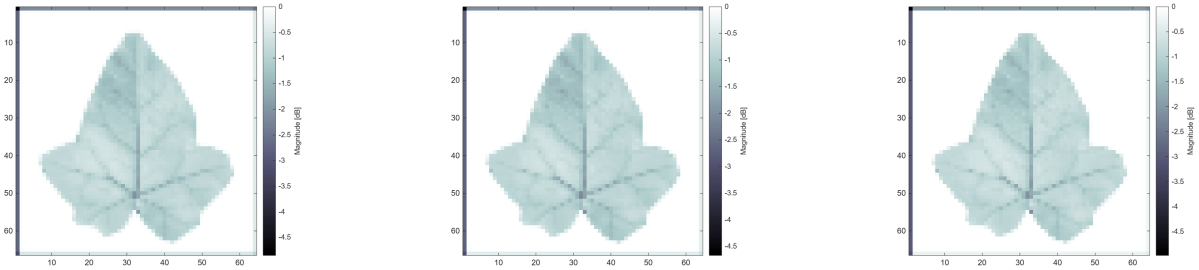

(a) $f = 350GHz$ **(b)** $f = 400GHz$ **(c)** $f = 450GHz$

Figure 4.2: Resolution-simulation outcomes for the leaf at different frequencies f.

4.3. Acquired THz images

Measurements were performed at multiple frequencies to evaluate the behavior of the imaging system over the available operating range. In this chapter, only the result around 400 GHz is shown as the representative measurement. It provides a clear example of the reconstructed leaf image and allows a direct comparison between the raw and frequency-averaged result. Additional images acquired at other frequencies are included in Appendix A. Although three camera pixels were measured during the scan, the figures in this chapter show the result of one selected pixel to present image formation clearly. The remaining pixel results are also included in the appendix for completeness.

4.3.1. Single-frequency image

Figure 4.3a shows the reconstructed THz image of the leaf sample at 400 GHz. The measured detector response of one pixel was converted to dB and then normalized to the highest transmitted value in the image. The outline of the leaf is clearly visible, and the central vein appears as a region of lower transmission compared with the surrounding leaf material. Several weaker structures are also visible inside the leaf area, although the background contains variations that are still present in the single-frequency result.

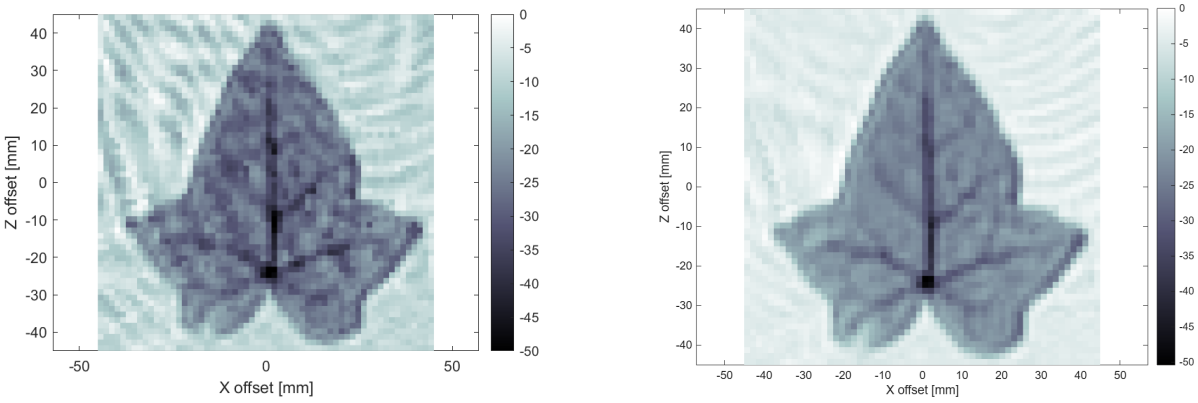

(a) Raw THz image of the leaf at 400 GHz

(b) Frequency-averaged around 400 GHz

Figure 4.3: Comparison between the raw THz image of the ivy leaf sample at 400 GHz and the frequency-averaged image obtained by combining the measurements at 398, 399, 400, 401, and 402 GHz.

4.3.2. Frequency-averaged image

To reduce frequency-dependent standing-wave artifacts, the images around the frequency of interest were averaged. The frequency-averaged image was obtained by combining frequencies ± 1 and ± 2 GHz around the center frequency. This approach reduces the influence of standing waves that vary with frequency, while still preserving object features that are relatively consistent over the narrow frequency range [17].

Figure 4.3b shows the raw ivy leaf at 400 GHz next to the frequency-averaged result. Compared with the raw image, the averaged result shows a smoother background and there is a more clear separation between the leaf area and the surrounding region. The central vein remains visible after averaging, which indicates that the averaging process reduces frequency-dependent artifacts without removing the main object features.

5

Discussion of the Results

In this chapter, the results from chapter 4 are discussed. First, the resolution simulation results are compared to the obtained THz images from the BiCMOS camera. After that, the images from the BiCMOS camera will be compared to the images from the CMOS camera used in Van Dijk's research [17].

5.1. Simulation vs Ground Truth

In figure 5.1, a comparison between the optical image and the resolution simulated one can be seen. One thing that stands out when looking at figure 5.1b is that the tips of the leaf have been cut off. This is due to the tape having a light color and therefor being filtered out by the image processing. The tape cutting parts of the image away in the simulation is not seen as problematic. This is because the tape is always located on the outside parts of the object so that the details in the center of the object are visualized more clearly. When looking at the contour of the leaf, the simulation is well able to display the contour of the optical image. Also most part of the veins inside the leaf are clearly distinguishable from the other parts of the leaf. The veins are displayed in dark colors while the parts where no veins reach are in lighter colors. This coincides with the expectation of the image of a leaf when looking at Van Dijk's results.

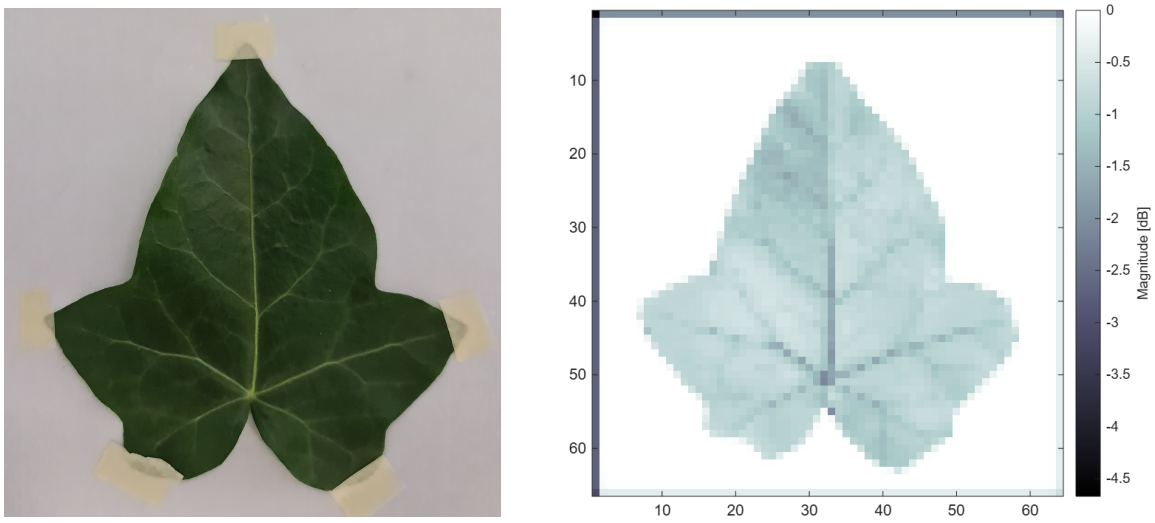

(a) Optical image of the ivy leaf.

(b) Resolution simulation of ivy leaf

Figure 5.1: Optical image of the ivy leaf with the resolution simulation result

To validate if the resolution image software is a helpful tool for the imaging system, the simulated results

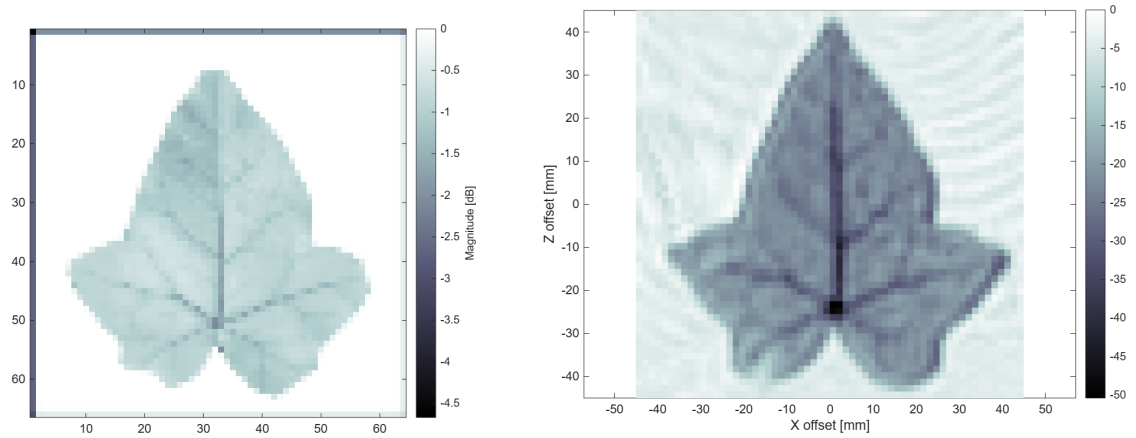

(a) Simulated image of ivy leaf at $f = 400GHz$

(b) THz image at $f = 400GHz$

Figure 5.2: Comparison of the simulated image and the THz image.

and the ground truth images are compared based on their resolution. Figure 5.2 shows the simulated image on the left and the obtained averaged THz image on the right side around a frequency of 400 GHz.

When comparing the two images in figure 5.2, one can see that the two images are very similar when it comes to resolution. The contours of both images follow the same path apart from the chopped off tips in the simulation image. Also the darker veins stand out in both images. The reason for the non-vein parts of the leaf being darker in the THz image then in the simulated image is because the simulation from the optical picture does not take transmissive characteristics of the object into account, as had been discussed in section 3.4.5. The ripples which are active in the background are due to the effect of standing waves. The two color bars of the images cannot be compared, again because of what has been described in section 3.4.5.

5.2. CMOS vs BiCMOS camera

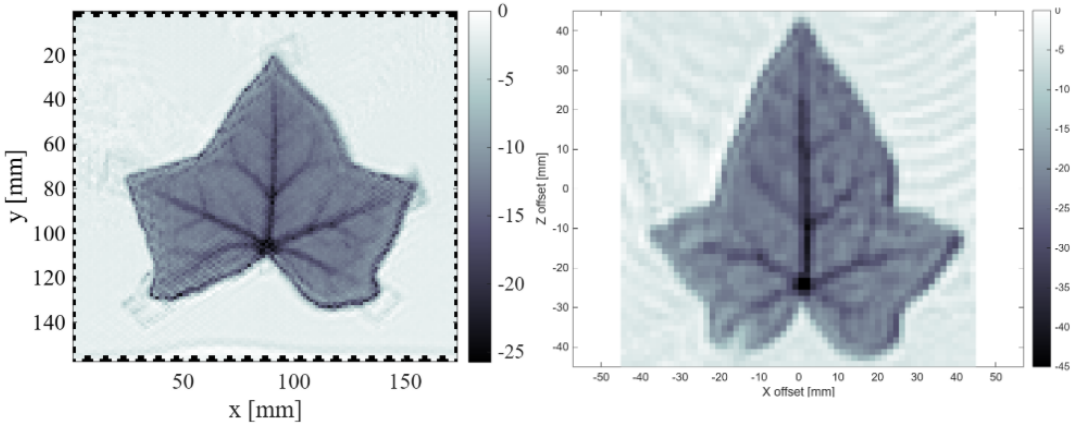

Figure 5.3: Comparison between CMOS camera used by Van Dijk on the left and BiCMOS camera used in this project on the right at $f = 400GHz$.

The image on the left in figure 5.3 is an image of an ivy leaf for the CMOS camera used by Van Dijk. On the right an image of the BiCMOS camera used in this project is presented. For a good comparison, the conditions would ideally be the same leaf in both figures with matching conditions like its water content. Nonetheless, some things can still be said regarding the resolution and the dynamic range.

What can be seen when comparing the resolution of the two images is that the CMOS camera seems to have a much higher resolution. This can be seen best when looking at the contours of the leaves.

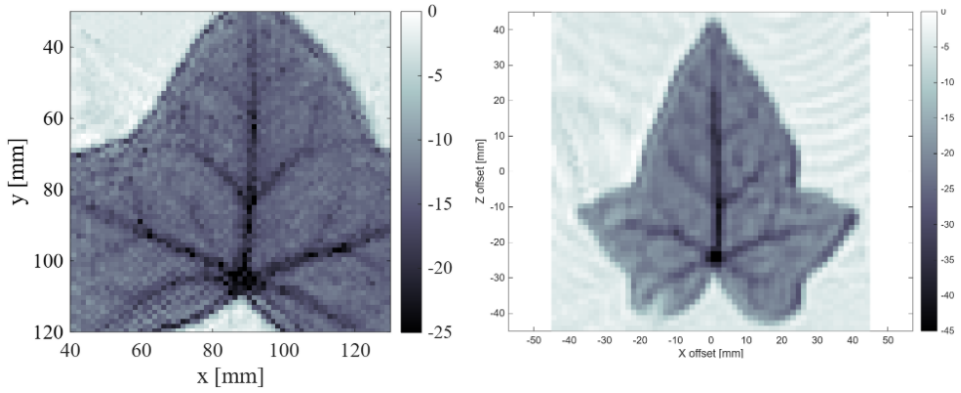

Figure 5.4: The CMOS leaf is now cut to be the same size as the BiCMOS leaf. When following the contours the resolution is roughly similar.

This huge difference in terms of resolution mostly has to do with the fact that the leaf in the CMOS image is much bigger than the leaf in the BiCMOS image. Where the image in the CMOS case has dimensions of roughly 150x170mm, the BiCMOS dimensions are only 90x90mm. A larger imaging region has more pixels for the same pixel separation. When limiting the axes to the same size of the BiCMOS image, the difference in resolution already decreases vastly as can be seen in figure 5.4. It can be seen that the difference in resolution, now only determined by the pixel separation, does not give significant benefits in terms of details. The same details can be seen in both images.

The dynamic range for the BiCMOS has been established by taking two extremes cases for transmissive properties. The highest dB value at the camera has been taken when no envelope was present in between the planoconvex and biconvex lens to simulate full transmissivity. The lowest dB value has been taken when a fully reflective piece of metal was placed in between. The difference in these to signals determines the dynamic range in dB. For the CMOS camera the dynamic range lies between 25dB and 30dB. For the BiCMOS this is measured to be between 45dB and 50dB. An improvement of 20dB in dynamic range for the BiCMOS can be concluded. This improvement in dynamic range means that the images from the BiCMOS camera can have more details.

5.3. Measurement uncertainty and limitations

Several factors may have influenced the measured image quality. First, the optical alignment of the source, lenses, sample, and camera is critical. A small misalignment can reduce the coupled power or introduce non-uniform illumination. Since the source beam and pixel beams both contribute to the final transmission response, alignment errors can affect both the signal level and the spatial uniformity of the image.

Second, standing waves can occur in the setup due to reflections between optical components, the sample holder, the camera lens, and surrounding structures. These standing waves can introduce frequency-dependent variations that are not directly related to the object itself. Frequency averaging can reduce this effect, but it does not remove all systematic variations.

Third, the CNC positioning system introduces practical limitations. The scan grid is generated from discrete mechanical positions, and each movement requires settling time. Positioning uncertainty can therefore slightly change the true sample position relative to the imaging plane. The distance between the imaging plane and camera lens could not be measured exactly, which introduces an uncertainty in the optical alignment. A small deviation from the intended distance may place the lens slightly out of focus and reduce the sharpness of the reconstructed image.

Finally, the sample itself also introduces uncertainty. The leaf may not be perfectly flat, or its water content may change over time. The sample being placed inside an envelope and fixed with tape can also have influence, since these materials may contribute to the measured transmission.

6

Conclusion and Future Work

This final chapter is provided with the conclusion of this work together with some proposals for future work. The conclusion will be made following the posed supporting research questions in section 1.8. The supporting questions were as follows:

1. How can the camera, source, readout electronics, data-acquisition equipment, and mechanical positioning system be integrated into an automated measurement workflow?
2. How can the measured pixel responses be mapped, stored, and processed into reconstructed THz images?
3. Can the integrated imaging system reproduce an interpretable THz image of a sample, and how does this result relate to the optical reference image and resolution simulation?
4. How do factors such as integration time, frequency averaging, pixel selection, and scan settings affect image quality and the total acquisition time?

The future work section will mention some improvements on the execution part of this work, together with a new step in THz imaging with the evaluated BiCMOS camera.

6.1. Conclusion

The central research question of this thesis was to determine to what extent the 24-pixel SiGe BiCMOS THz camera can produce repeatable and interpretable images in an active configuration when integrated with the available quasi-optical measurement system. The results show that the camera can be integrated into a complete active imaging workflow and can produce interpretable THz transmission images of a sample. The developed MATLAB interfaces combine hardware configuration, connection testing, scan definition, live image preview, data storage, resolution-simulation, and post-processing in their respective controlled workflows. This makes the measurement and simulation procedure repeatable in the sense that the same settings can be stored and reused.

In chapter 3 the imaging setup to obtain THz images has been discussed. In the setup, the signals of two DACs together with a synthesizer signal were mixed together in an on-off modulated fashion before being amplified by a PA and fed into a frequency extender which is there to actively illuminate the object in the imaging plane. The imaged object is moved by a CNC machine while the frequency extender sends waves through the object via a focusing lens into the THz camera.

The measured pixel responses were successfully mapped to spatial positions in the imaging plane and reconstructed into THz images. The main result shown in the thesis is the ivy leaf measurement around 400 GHz. In this result, the outline of the leaf and the central vein are visible, which shows that the integrated system can produce an interpretable active THz image. The optical reference image and

resolution simulation provide supporting information for identifying the main leaf features. Measurement at other frequencies and from other measured pixels are included in the appendix, but the main conclusions are based on the representative 400 GHz result. Additional measurements on different objects were made, which provided extra insight into the capabilities of the camera.

The image quality was affected by several acquisition and processing choices. Increasing the integration time can improve the stability of the measured response, but at the same time it increases the total acquisition time. This ensures a better SNR since random white noise is filtered out. Frequency averaging over 398, 399, 400, 401, and 402 GHz reduced background variations, such as standing waves which showed a rippled pattern, while preserving the main leaf structure. Pixel selection also affected displayed result, since three pixels were measured during the scan but only one selected pixel was shown in the main results for clarity. The scan area and step size determined the number of required spatial positions and therefore formed one of the main contributors to the total measurement time. If more pixels could be read out and combined at the same time, the step size could be reduced and therefore acquire images quicker. Overall, the thesis demonstrates that the 24-pixel SiGe BiCMOS camera can be used for active image formation in the available setup, but the demonstrated performance is still limited by system-level factors such as optical alignment, mechanical scanning, standing waves, and pixel-dependent response.

6.2. Future Work

Future work should first focus on making the imaging performance more quantitative. Repeated measurements of the same sample should be performed with equal settings to determine the repeatability of the reconstructed images. In addition, the signal-to-noise ratio and dynamic range could be calculated from defined regions in the image instead of being assessed only by visual inspection. This would make it possible to compare different frequencies, integration times, pixels, and processing methods more objectively.

A second improvement is the optimization of the acquisition procedure. The total acquisition time is strongly influenced by the number of scan positions, integration time, number of frequency points, and the CNC motion sequence. Faster scans could be obtained by reducing unnecessary hardware enable and disable steps, optimizing settling times, and using more camera pixels simultaneously. The effect of these changes should be tested against the resulting image quality to find a practical balance between speed and performance. Scanning with more pixels also requires the resolution simulation software to be updated to simulate outcome images based on the corresponding multi-pixel radiation pattern. This makes the simulation process quicker and also takes deviations in multi-pixel radiation patterns into account.

When looking at physical upgrades to the setup, one most likely has to implement a switching system to use multiple pixels together with a limited amount of ADCs. Also all measurements have been done without the use of absorbing foam. The use of absorbing foam could potentially decrease the effect of standing waves even more which results in better images.

Future work should also address the remaining optical and calibration uncertainties. The distance between the imaging plane and the camera lens could not be measured exactly, which may place the system slightly out of focus and reduce the sharpness of the reconstructed image. A more precise alignment procedure should therefore be developed. In addition, pixel-dependent response differences should be characterized in order to implement response-equalization, which would improve the uniformity of multi-pixel images.

The last suggestion for future work would be to demonstrate a different type of THz imaging with the camera. One could go for reflective imaging instead of transmissive imaging to perhaps observe metal surfaces inside electronic objects. Since the dynamic range of the BiCMOS camera has been determined to be much lower than its predecessor, passive imaging is also something to be investigated.

References

[1] G. Valušis, A. Lisauskas, H. Yuan, W. Knap, and H. G. Roskos, "Roadmap of Terahertz imaging 2021," *Sensors*, vol. 21, no. 12, p. 4092, Jun. 2021. DOI: 10.3390/s21124092.

[2] J. Wang, M. Naftaly, and E. Wasige, "An overview of terahertz imaging with resonant tunneling diodes," *Applied Sciences*, vol. 12, no. 8, Apr. 2022, Art. no. 3822. DOI: 10.3390/app12083822.

[3] D. Jasteh, E. Hoare, M. Cherniakov, and M. Gashinova, "Experimental low-terahertz radar image analysis for automotive terrain sensing," *IEEE Geoscience and Remote Sensing Letters*, vol. 13, no. 4, pp. 490–494, Apr. 2016. DOI: 10.1109/LGRS.2016.2518579.

[4] P. Hillger, J. Grzyb, R. Jain, and U. R. Pfeiffer, "Terahertz imaging and sensing applications with silicon-based technologies," *IEEE Transactions on Terahertz Science and Technology*, vol. 9, no. 1, pp. 1–19, Jan. 2019. DOI: 10.1109/TTHZ.2018.2884852.

[5] E. Seok et al., "Progress and challenges towards Terahertz CMOS integrated circuits," *IEEE Journal of Solid-State Circuits*, vol. 45, no. 8, pp. 1554–1564, Aug. 2010. DOI: 10.1109/JSSC.2010.2049793.

[6] P. L. Richards, "Bolometers for infrared and millimeter waves," *Journal of Applied Physics*, vol. 76, no. 1, pp. 1–24, Jul. 1994.

[7] A. Timofeev et al., "Optical and electrical characterization of a large kinetic inductance bolometer focal plane array," *IEEE Transactions on Terahertz Science and Technology*, vol. 7, no. 2, pp. 218–224, Mar. 2017.

[8] S. van Berkel, O. Yurduseven, A. Freni, A. Neto, and N. Llombart, "THz imaging using uncooled wideband direct detection focal plane arrays," *IEEE Transactions on Terahertz Science and Technology*, vol. 7, no. 5, pp. 481–492, Sep. 2017. DOI: 10.1109/TTHZ.2017.2736338.

[9] R. A. Hadi et al., "A 1 k-pixel video camera for 0.7–1.1 Terahertz imaging applications in 65-nm CMOS," *IEEE Journal of Solid-State Circuits*, vol. 47, no. 12, pp. 2999–3012, Dec. 2012. DOI: 10.1109/JSSC.2012.2217851.

[10] R. Han et al., "Active Terahertz imaging using schottky diodes in CMOS: Array and 860-GHz pixel," *IEEE Journal of Solid-State Circuits*, vol. 48, no. 10, pp. 2296–2308, Oct. 2013. DOI: 10.1109/JSSC.2013.2269856.

[11] K. Sengupta, D. Seo, L. Yang, and A. Hajimiri, "Silicon integrated 280 GHz imaging chipset with 4 $\times$ 4 SiGe receiver array and CMOS source," *IEEE Transactions on Terahertz Science and Technology*, vol. 5, no. 3, pp. 427–437, May 2015. DOI: 10.1109/TTHZ.2015.2414826.

[12] A. Lisauskas et al., "Terahertz imaging with GaAs field-effect transistors," *Electronics Letters*, vol. 44, pp. 408–409, Feb. 2008.

[13] R. Zatta, R. Jain, J. Grzyb, and U. R. Pfeiffer, "Resolution limits of hyper-hemispherical silicon lens-integrated THz cameras employing geometrical multiframe super-resolution imaging," *IEEE Transactions on Terahertz Science and Technology*, vol. 11, no. 3, pp. 277–286, May 2021. DOI: 10.1109/TTHZ.2021.3063839.

[14] M. Hoogelander et al., "Chessboard focal plane array for a CMOS-integrated Terahertz camera," *IEEE Transactions on Terahertz Science and Technology*, vol. 13, no. 6, pp. 704–717, Nov. 2023. DOI: 10.1109/TTHZ.2023.3297072.

[15] S. van Berkel et al., "Wideband modeling of CMOS schottky barrier diode detectors for THz radiometry," *IEEE Transactions on Terahertz Science and Technology*, vol. 11, no. 5, pp. 495–507, Sep. 2021. DOI: 10.1109/TTHZ.2021.3085137.

[16] M. Hoogelander et al., "Diffraction-limited imaging demonstration using a silicon integrated array at terahertz frequencies," in *International Conference on Infrared, Millimeter, and Terahertz Waves, IRMMW-THz*, 2022. DOI: 10.1109/IRMMW-THz50927.2022.9895490.

[17] R. van Dijk, “Demonstration of near diffraction-limited imaging using a THz CMOS-integrated camera,” M.S. thesis, Delft University of Technology, Delft, The Netherlands, Nov. 2023.

[18] M. Hoogelander, R. van Dijk, M. Spirito, N. Llombart, and M. Alonso-delPino, “Demonstration of near diffraction-limited Terahertz images using a CMOS-integrated chessboard array,” *IEEE Transactions on Terahertz Science and Technology*, vol. 14, no. 4, pp. 531–536, Jul. 2024. DOI: 10.1109/TTHZ.2024.3387650.

[19] M. Hoogelander, M. Spirito, B. Sutbas, C. Carta, N. Llombart, and M. Alonso-delPino, “Chessboard FPA in 130-nm SiGe BiCMOS for high-resolution passive terahertz imaging,” *IEEE Journal of Microwaves*, vol. 6, no. 2, pp. 334–349, 2026. DOI: 10.1109/JMW.2026.3660185.

[20] Mini-Circuits, *Wideband amplifier ZVA-213-S+ datasheet*, https://www.minicircuits.com/pdfs/ZVA-213+.pdf, Accessed: June 11, 2026.

[21] MathWorks, *Visadev: Create connection to device using VISA*, MATLAB Documentation, Accessed: 2026-06-13, 2026.

[22] J. F. Johansson, “Millimeter-wave imaging theory and experiments,” Onsala Space Observatory, Onsala, Sweden, Tech. Rep. 151, 1986.

A

Supplementary Imaging Results

This appendix contains several results of objects other than the ivy leaf that have been imaged. Per object the optical image, the resolution simulation image, and the THz outcome will be given. The remaining objects that have been scanned are tag from a piece of clothing (A.1), a public transport ticket (A.2), a pencil (A.3), a blister pack (A.4), a floppy disc (A.5), a pipette filled with water and air bubbles (A.6), and a slice of bacon (A.7). All resolution simulation images and THz images have been made at a frequency of 400 GHz.

A.1. Tag

A tag from a piece of clothing bought in store has been imaged. The optical image together with the simulated image can be seen in figure A.1 below. The tag has a thickness of 0.6mm.

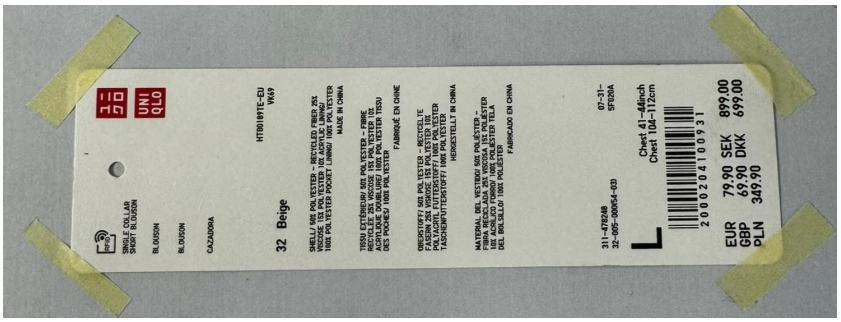

(a) Optical image of the tag.

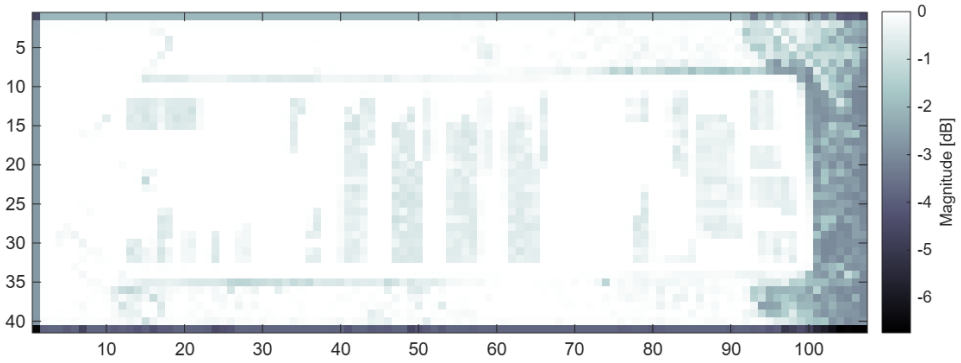

(b) Simulation outcome at a frequency $f = 400GHz$.

Figure A.1: Optical image of a tag and the resolution simulation.

Comparing the simulated image to the optical, one can see that the letters on top appear blurred due to the 1.5mm resolution being too coarse for the small letters. Figure A.2 shows the simulated image next to the THz image.

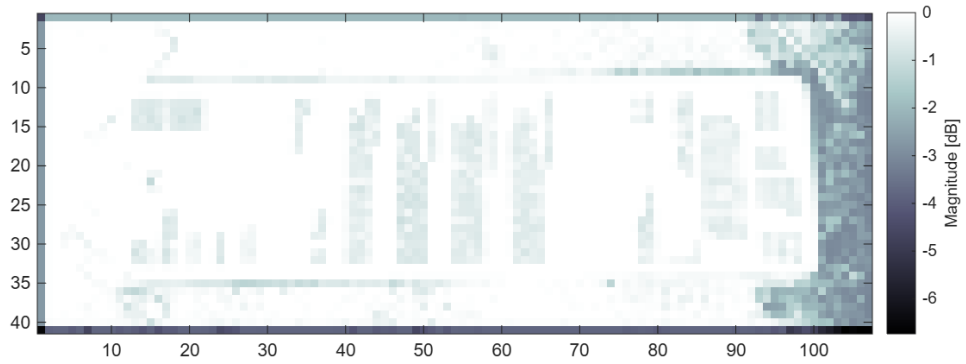

(a) Simulation outcome at a frequency $f = 400GHz$.

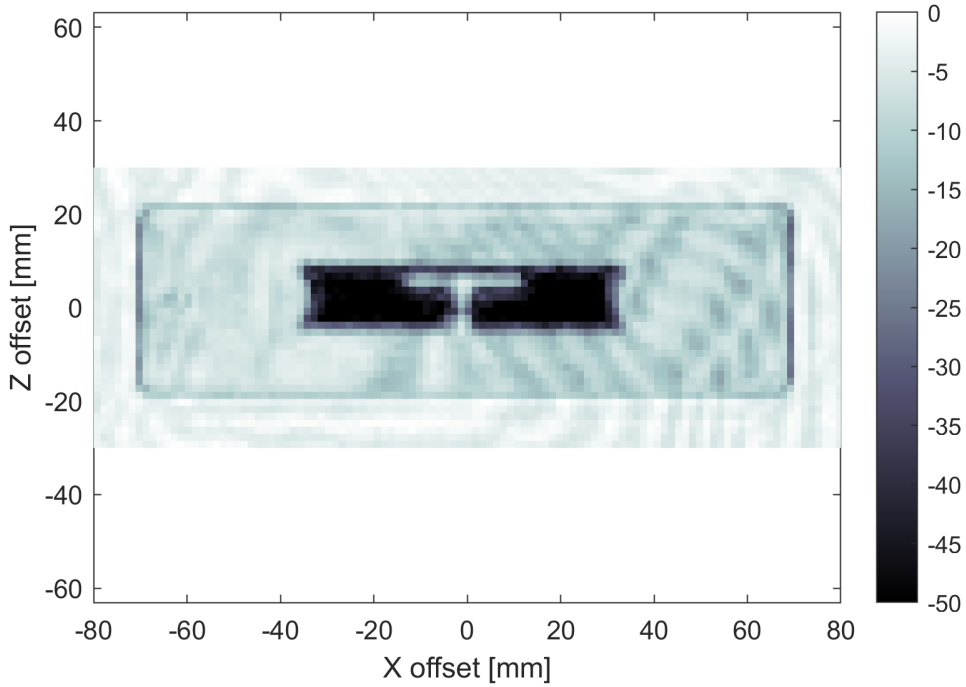

(b) THz image outcome at $f = 400GHz$.

Figure A.2: Resolution simulated image together with THz outcome image.

The THz image clearly shows the limitations of the resolution simulation software. The simulation software expected the image to look the same but with blurred letters. Instead, the THz image beautifully exposes the hidden metal structure of the RFID-chip located inside the ticket. The THz waves are able to travel through the paper parts of the ticket, but are reflected by the metal of the chip. That is why the chip is revealed in THz imaging. The RFID-chip turns out to be about 20mm high and 70mm wide and has a T-shaped gap in the middle with inward curved edges on the short sides.

A.2. Public Transport Ticket

Just like a tag, a temporary public transport card also contains an RFID-chip inside. Figure A.3 below shows the optical image of a metro ticket together with the simulated outcome at a frequency of 400GHz. The ticket has a thickness of 0.4mm.

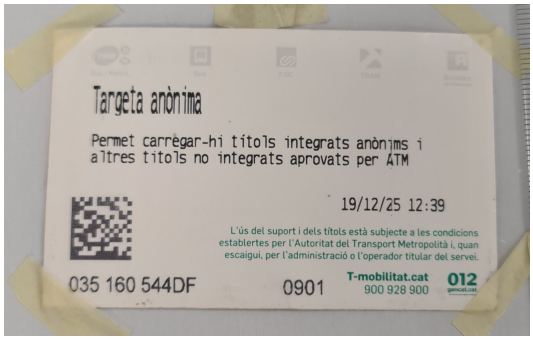

(a) Optical image of the metro ticket.

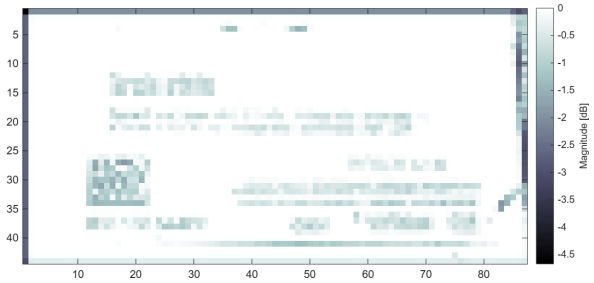

(b) Simulation outcome at a frequency $f = 400GHz$.

Figure A.3: Optical image of the metro ticket and the resolution simulation

From the simulated image, results similar to those of the tag can be observed. The letters on the surface of the card have become indistiguishable. This is what is to be expected from a pixel separation of 1.5mm since the lines of letters here are also smaller than that. The corresponding THz image at 400GHz is shown in figure A.4 below next to the simulated one.

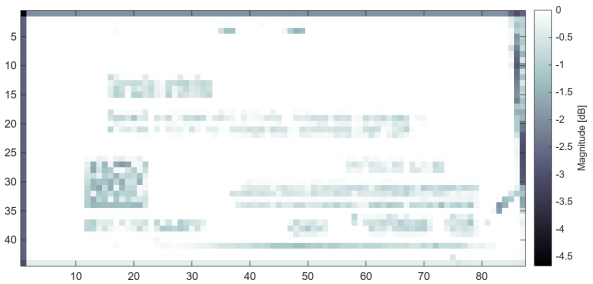

(a) Simulation outcome at a frequency $f = 400GHz$.

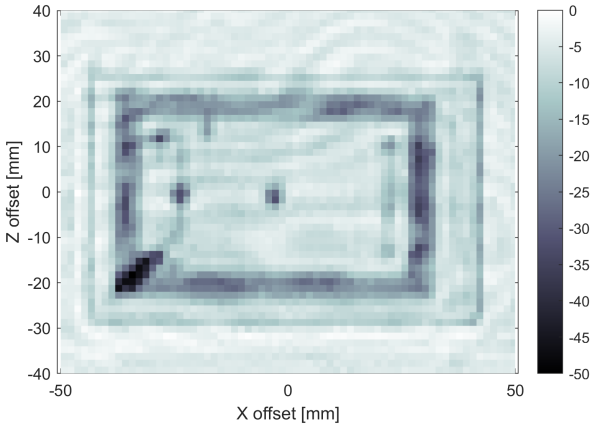

(b) THz image outcome at $f = 400GHz$.

Figure A.4: Resolution simulated image next to the THz outcome image.

Just as with the tag, the RFID chip inside has been exposed. Unlike the tag RFID-chip, this chip mostly goes along the sides leaving a big hole the center apart from a tiny spec. The strip of the metal square is around 5mm tick, with the long sides of the square being around 70mm long and the short sides a little more than 40mm. Since the metal square shows a spectrum of colors instead of one shade, it suggests to consist of multiple thin lines next to each other instead of one thick strip. A confirmation is shown in figure C.7.

A.3. Pencil

An excellent absorber of THz waves is graphite. The inside of a pencil is made from this material. Since pencils are made of wood, which is also what paper is made of, the THz waves should travel through the pencil except for the graphite filling. This could potentially mean one can scan for faults or fractions in the graphite in this case. Since the BiCMOS camera has a pixel separation of 1.5mm, fractions of the graphite will most likely be impossible to spot. For the sake of future THz camera's with better resolutions, an artificial fracture here has been exaggerated to demonstrate faults in the graphite. The pencil has been split in two parts over its length and a piece of 5mm has been carved out to represent the graphite filling not being one piece anymore. This can be seen in figure A.5a below. Figure A.5 shows the optical image and the simulated image side by side. The thickness of the graphite with the wood is 4.8mm.

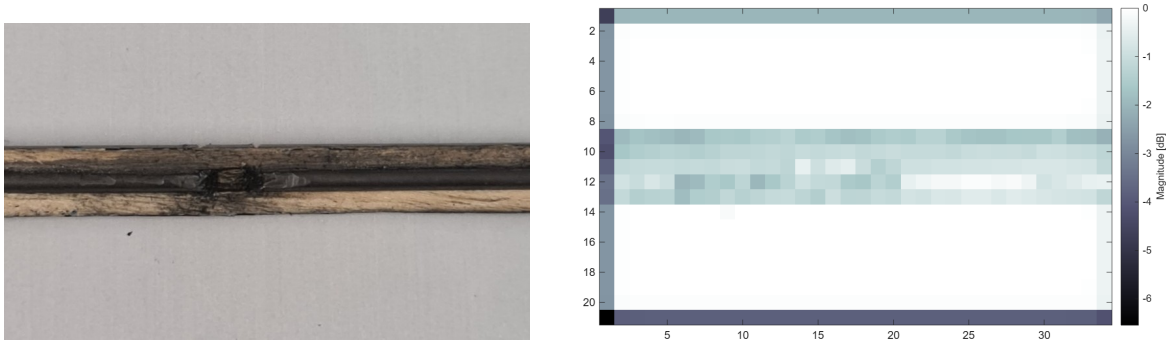

(a) Optical image of the pencil.

(b) Simulation outcome at a frequency $f = 400GHz$.

Figure A.5: Optical image of the pencil and the resolution simulation.

In the middle of the simulated image, slightly to the left, one can see a somewhat lighter spot in the place where the gap would be when looking at the optical image. This would mean that the THz image would be able to demonstrate the gap in the graphite in case the THz waves are able to traverse through wood. The reason the simulated image is fairly pixelated is because the scan is taken over a small section of 50mm of the pencil. Figure A.6 below shows the simulated image next to THz outcome image at a frequency of 400GHz.

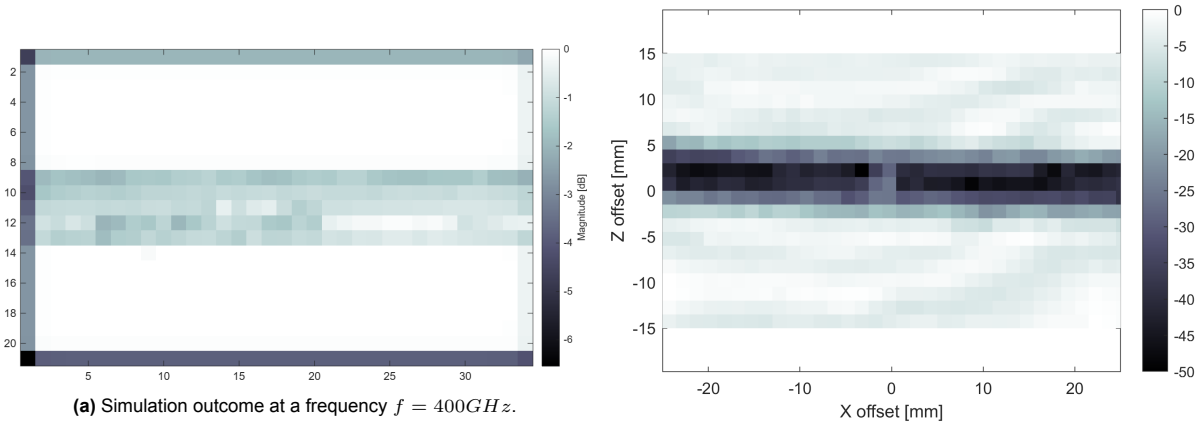

(a) Simulation outcome at a frequency $f = 400GHz$.

(b) THz image outcome at $f = 400GHz$.

Figure A.6: Resolution simulated image next to the THz outcome image.

As expected and proven by the resolution simulation software, the THz image is able to show the gap

in the graphite. This shows that THz imaging could play an interesting role in the future when it comes to checking the quality of materials.

A.4. Blister Pack

Another combination of a transmissive material with a non-transmissive material is a blister pack. THz waves should be able to travel through the plastic, but are reflected by the metal foil layer behind it. For this particular case, one should be able to show which pill compartments have been opened and which ones are still closed. This is what can be tested with the imaging setup. Figure A.7 below shows the optical image of the blister pack together with its corresponding resolution simulation image. The thickness of the plastic with the metal foil is 0.4mm. The pill containing part is 3.6mm high.

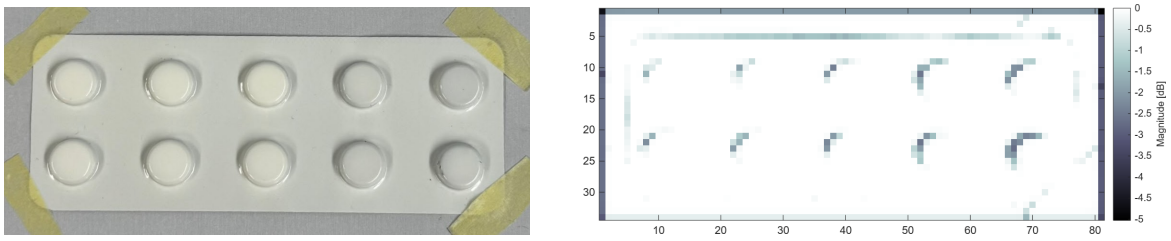

(a) Optical image of the blister pack.

(b) Simulation outcome at a frequency $f = 400GHz$.

Figure A.7: Optical image of the blister pack and the resolution simulation.

The simulated image shows another fault of the resolution simulation software. If the object itself is mostly white, loads of details will disappear in the simulated image. The THz image does not have problems with the color of an object, its outcome only depends on the material properties. Figure A.8 below shows the simulated image next to the THz outcome image at a frequency of 400GHz.

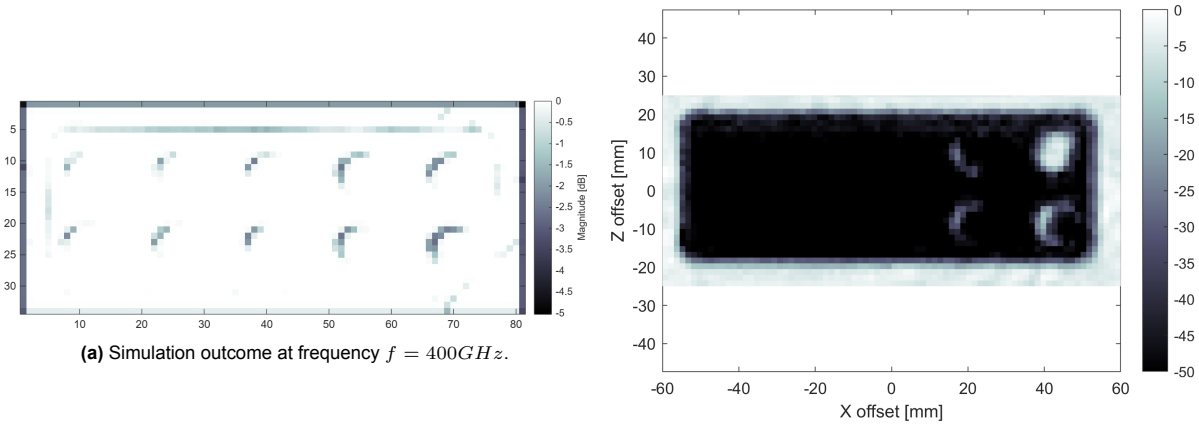

(a) Simulation outcome at frequency $f = 400GHz$.

(b) THz image outcome at $f = 400GHz$.

Figure A.8: Resolution simulated image next to THz outcome image.

Figure A.8 clearly shows a difference between the simulated image and the THz outcome image. What can be concluded from the THz image is that the four right pill compartments of the blister pack have been opened. This corresponds with the adaptations that were carried out in the preparation of the imaging sample.

A.5. Floppy Disc

Some floppy disc components are visible from the outside like the metal slide on top, known as the 'shutter', which can be seen in figure A.9a. One cannot see what components lie inside however. THz imaging can expose what is inside since most part of the floppy case is made of plastic. Figure A.9 shows the optical image and its simulated one side by side. The floppy has a thickness of 3.3mm.

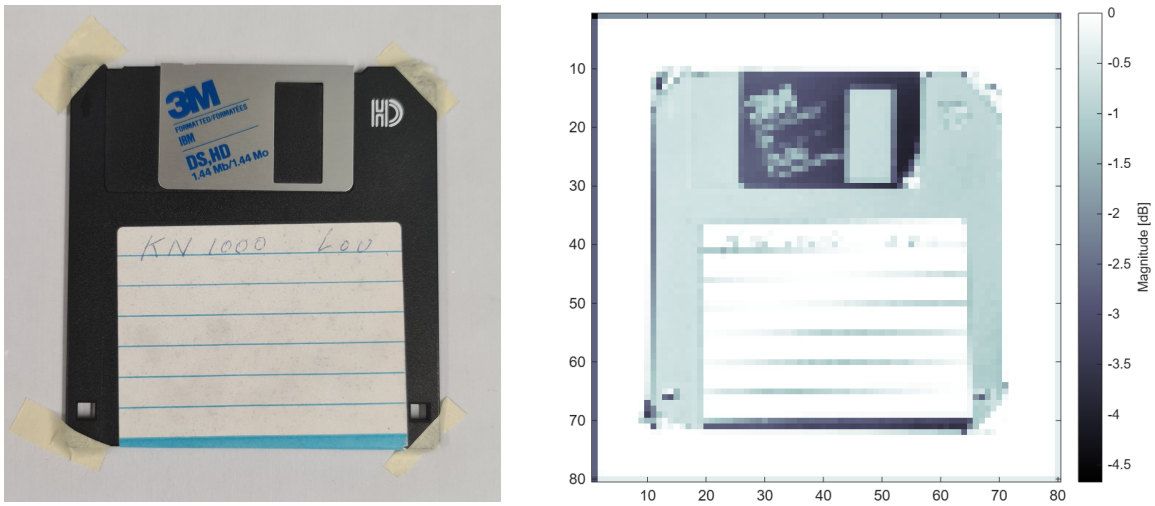

(a) Optical image of the floppy disc.

(b) Simulation outcome at a frequency $f = 400GHz$.

Figure A.9: Optical image of the floppy disc and the resolution simulation.

When looking at the simulated image at the hole in the metal shutter on top, one can see that the resolution of the camera will clearly show the hole with clean lines in case no metal would hind behind the hole. Figure A.10 below shows the THz outcome image next to the simulated image.

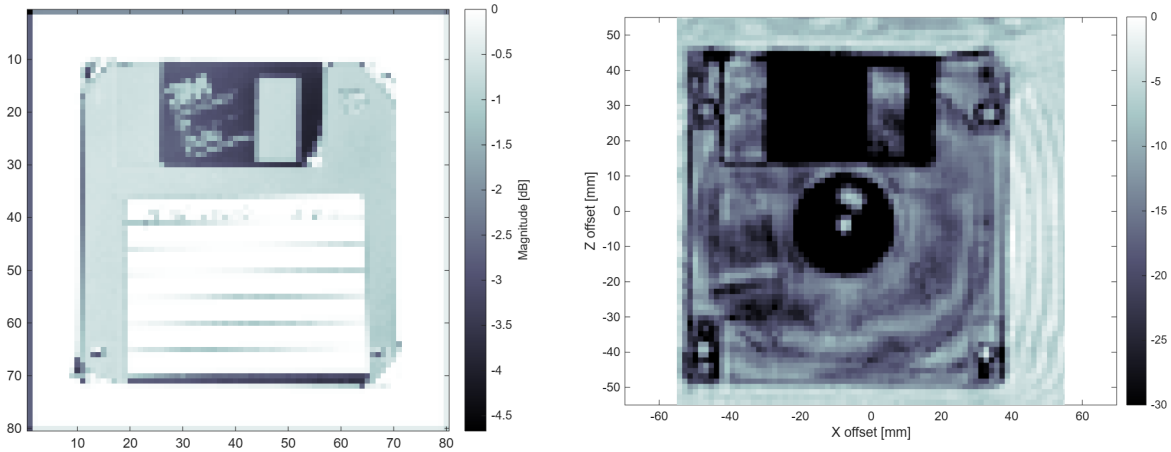

(a) Simulation outcome at a frequency $f = 400GHz$.

(b) THz image outcome at $f = 400GHz$.

Figure A.10: Resolution simulated image next to THz outcome image.

The THz image beautifully shows the reflected pieces of metal, both the metal shutter on top as well as the the little metal circle in the middle off the back side known as the "drive hub". Not only the metal parts can be seen, but also the disc inside is vaguely visible. The limits of the dynamic range have been manually decreased to -30dB to 0dB with the aim to make the disc stand out more.

A.6. Pipette

A similar principle to the case with the pencil would be the detection of air bubbles in a tube filled with a liquid. A concrete example of this would be for instance in server cooling applications. Air bubbles in a liquid cooling system could cause spots where the electric components get hot since no fluid can reach it. To test if air bubbles or cavities would be visible to the THz camera, a pipette has been filled with water and air bubbles in the tube. The optical image of the prepared pipette can be seen in figure A.11 together with the simulated outcome image. The threshold value for the background color correction has been lowered from 133 to 100 to improve the visibility of the simulation outcome. The tube in the middle has a thickness of 4.7mm.

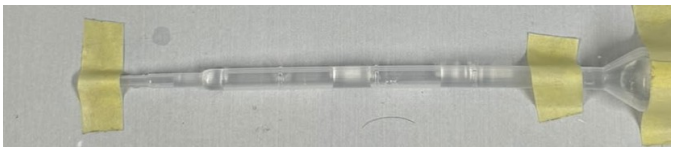

(a) Optical image of the pipette filled with two air bubbles.

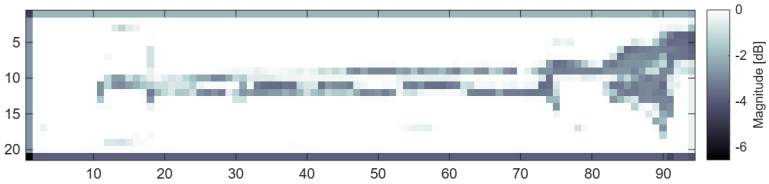

(b) Simulation outcome at a frequency $f = 400GHz$.

Figure A.11: Optical image of the pencil and the resolution simulation.

When looking at the simulated image in figure A.11 above, two darker sections appear above the 40th and 60th pixel on the x-axis. The reason for this can be seen in the optical image. The regions where water is located in the tube appear brighter since the water reflects the lights coming from the ceiling better than the parts where air is located. In the simulated image this would result in a lighter spot at the places where liquid is present. It can be seen from the simulated image that the water contents are distinguishable from the air contents. Figure A.12 below shows the simulated image next to the outcome THz image.

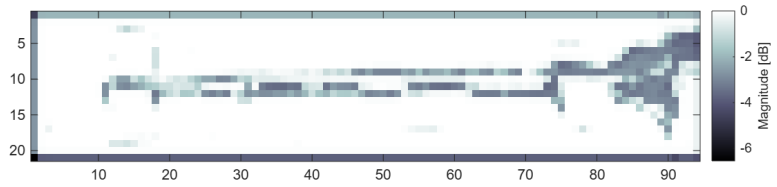

(a) Simulation outcome at a frequency $f = 400GHz$.

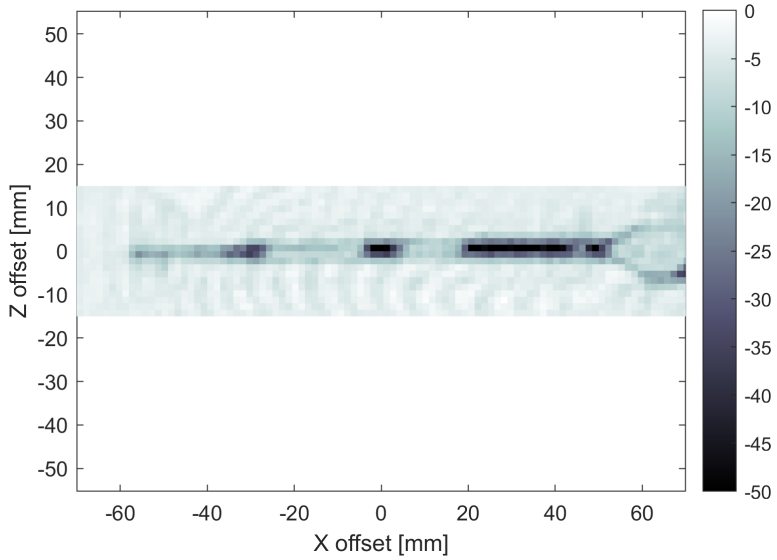

(b) THz image outcome at $f = 400GHz$.

Figure A.12: Resolution simulated image next to the THz outcome image.

When comparing the simulated image with the THz outcome, one can see that the colors inside the tube are opposed as to one another. This is because the water in the simulated images appears brighter than the air cavities and therefore gets a lighter color. To the THz waves water is a great absorber and therefor absorbs most of the radiation, making the water dark in the image and the air cavities lighter since the waves are not absorbed in those parts.

A.7. Bacon

It has been established that difference in water or fluid contents in general can be brought to light by the THz imaging system. In terms of medical applications it would be interesting to see the difference in water contents in organic tissue. A hypothetical implementation would be in oncology where tumors could perhaps be detected based off a different water content of the tumor compared to healthy tissue. To see how the THz system would perform on organic tissue, a piece of bacon has been imaged (see figure A.13). The bacon has a thickness of 0.6mm

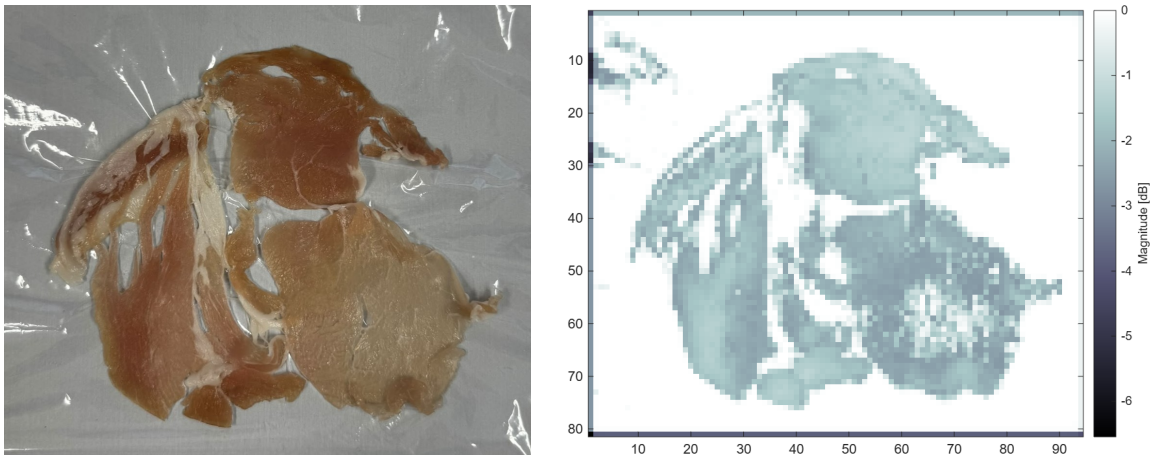

(a) Optical image of a slice of bacon.

(b) Simulation outcome at a frequency $f = 400GHz$.

Figure A.13: Optical image of a slice of bacon and its simulated outcome.

Looking at the simulated image above, one can see that the reflections of the foil containing the slice of bacon are also simulated. These are expected to disappear in the actual THz image. Comparing the gaps in the piece of bacon to the gaps in the simulation, it is expected to distinguish the gaps from the meat itself. Another thing that can be seen is that the white parts of the meat have been filtered out, resulting in the gaps appearing bigger in the simulated image. Figure A.14 below shows the simulated image next to the THz outcome.

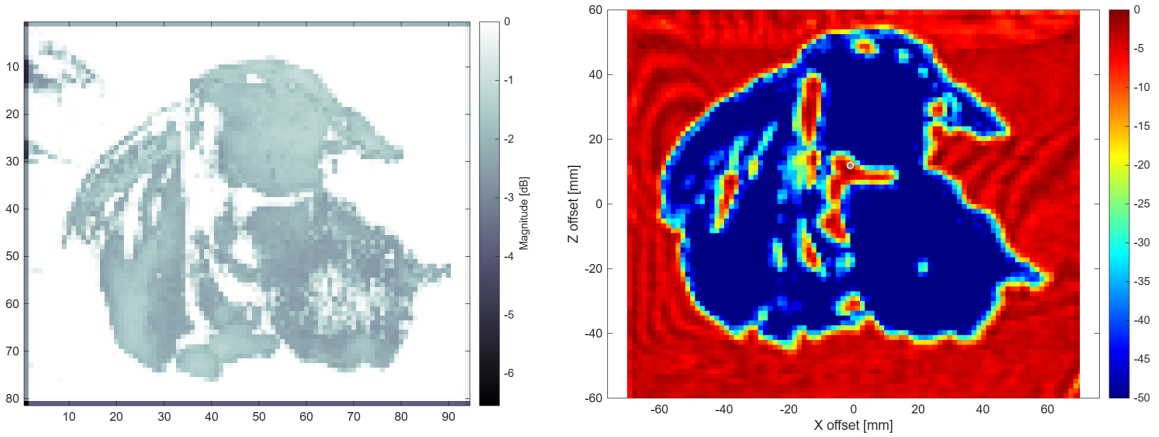

(a) Simulated outcome at a frequency $f = 400GHz$.

(b) THz image outcome at $f = 400$.

Figure A.14: Resolution simulated image next to the THz outcome.

The bacon has been plotted in 'jet' colors in MATLAB. This is to improve the visibility in the fat parts of the slice. As expected, the reflections of the foil in the optical image which have been simulated are not present in the THz image. Comparing the gaps in the bacon one can see that the holes are clearly visible. The red tissue seems to absorb the most of the THz waves. From comparing the optical image to the THz outcome, to compare the white tissue areas, it can be seen that the white areas absorb the waves less than the red area. This means that less water is present in the white tissue compared to the red tissue. The hypothesis to this is that fat contains more oils is stead of water compared to the red tissue. The THz image system has not been tested on other fluids than water so therefor this remains a hypothetical declaration.

B

Ethical Implications of the Product and Engineering Process

B.1. Societal impacts of the product

The concept demonstrator developed in this project is an active THz imaging system based on a 24-pixel SiGe BiCMOS camera. If such a system were developed further, it could have several positive societal impacts. THz imaging can be useful for non-destructive inspection, for example by detecting hidden structures, water content, defects, or foreign objects without cutting open or damaging a sample. Relevant stakeholders include researchers, industrial users, quality-control engineers, and potentially medical or security professionals. A compact THz camera could improve inspection reliability and reduce material waste by identifying defects earlier in industrial settings. In other fields such as biomedical research, it could support tissue or sample analysis.

There are also some negative impacts of this system. Imaging technologies that can see through packaging, clothing, or other non-metallic barriers may raise privacy concerns if applied to people or their personal belongings. In security applications, stakeholders such as travellers, employees, or the general public could be affected if the imaging is performed without sufficient transparency or consent. Another risk is that a THz image can appear precise, while the actual interpretation may depend strongly on calibration, resolution, or noise of the overall system.

B.2. Ethical aspects of the development process

The development process in this project was ethically low-risk because it did not involve people, animals, or sensitive data. The measurements were performed on non-living samples, such as an ivy leaf. The acquired data therefore did not contain personal or privacy-sensitive information. The main ethical aspects were related to laboratory safety, responsible use of equipment, and accurate reporting.

The setup used several electronic components which could introduce practical risks if operated incorrectly, such as unsafe mechanical movement, unintended source operation, or damage to equipment. For this reason, the software implementation included connection testing and input validation. Another process-related consideration is energy and resource use. Long automated scans consume time and electricity. This makes it important to plan measurements carefully and avoid unnecessary repeated scans.

B.3. Ethical evaluation

The most significant ethical concern for a future THz imaging system is privacy. A system that can image through certain materials could be misused if deployed without clear boundaries. This is especially relevant in public security or workplace monitoring, where individuals may not have any control over being scanned. Another concern is reliability. If THz images were used for medical decisions, false

positives or false negatives could have serious consequences. The technology should therefore not be presented as more accurate or mature than the evidence shows.

At the same time, the product also has ethically valuable aspects. Non-destructive imaging can reduce waste, support safer inspection, and provide information without damaging the samples. The engineering process also included responsible choices. Namely, the project avoided human and animal subjects. Measurement data were stored for traceability. A relevant trade-off is performance versus resource use. Higher resolution and frequency averaging can improve imaging quality, but they also increase scan time and energy use. Another trade-off is automation versus safety. Automation improves repeatability, but only if safeguards are implemented to prevent unintended hardware actions.

B.4. Reflection on the design choices

The main ethical considerations that influenced the project were safety and reproducibility. The hardware-control GUI was designed to reduce the chance of user error by separating hardware configuration, connection testing, acquisition settings, and live measurement feedback. CNC movement was handled through controlled scan settings rather than manual commands. Measurement metadata were saved together with the measured data so that results could be checked and reprocessed later. The simulation GUI applied a similar approach by only keeping a fixed amount of inputs available to the user of the interface, while doing all of the processing in a separate module. These choices support responsible engineering because they make the demonstrator easier to inspect, repeat, and verify.

Looking back, the project could have further strengthened the ethical process by including a more formal risk checklist before doing long measurements. Also, energy or acquisition-time costs for different scan settings could be recorded. These additions would make the trade-off between image quality and measurement resources clearer.

B.5. Forward-looking responsibility

Several measures would be required if the demonstrator were developed further. First, the intended application must be defined clearly. For any application involving people, privacy and informed consent would be essential. Second, the system would need technical validation, including calibration procedures and uncertainty measures. Third, the software should include audit logs, safe default states, and clear user feedback. Finally, the development process should involve relevant stakeholders early, including the end users, safety experts, and ethics specialists. This would help ensure that improved imaging performance is matched by a responsible deployment of the system.

C

Full-sized Images

This appendix contains additional figures that support the results presented in the thesis. The figures are included at a larger scale to make visual comparison easier for the reader. This includes additional THz images acquired at different frequencies, larger versions of the GUI screenshots, and supporting simulation outputs.

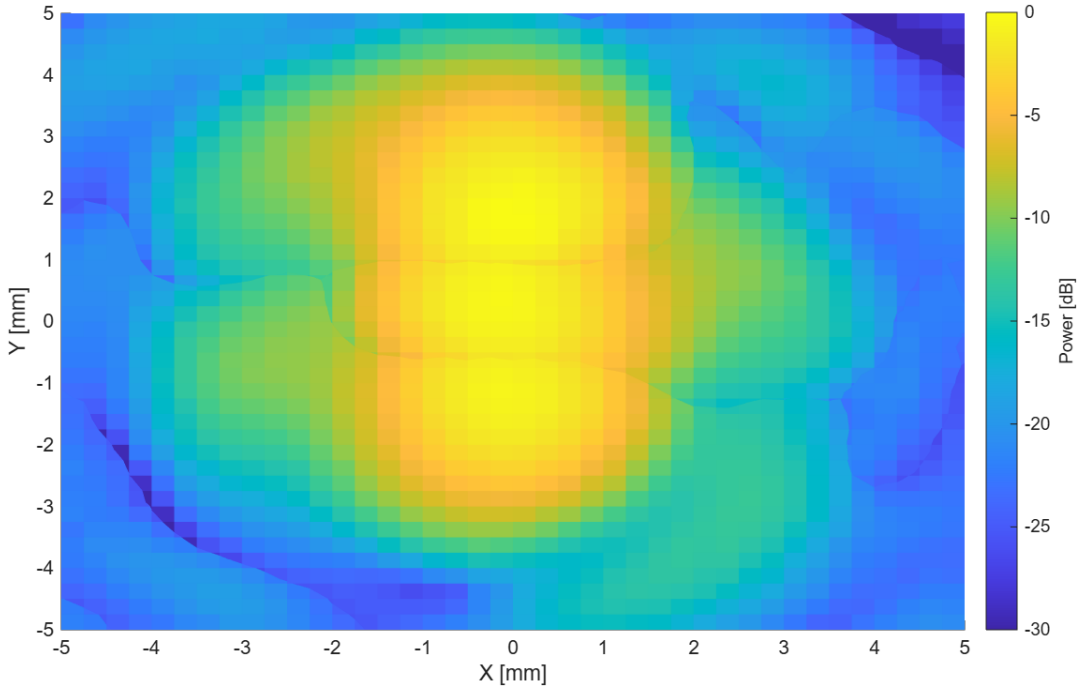

(a) Top view of the radiation pattern.

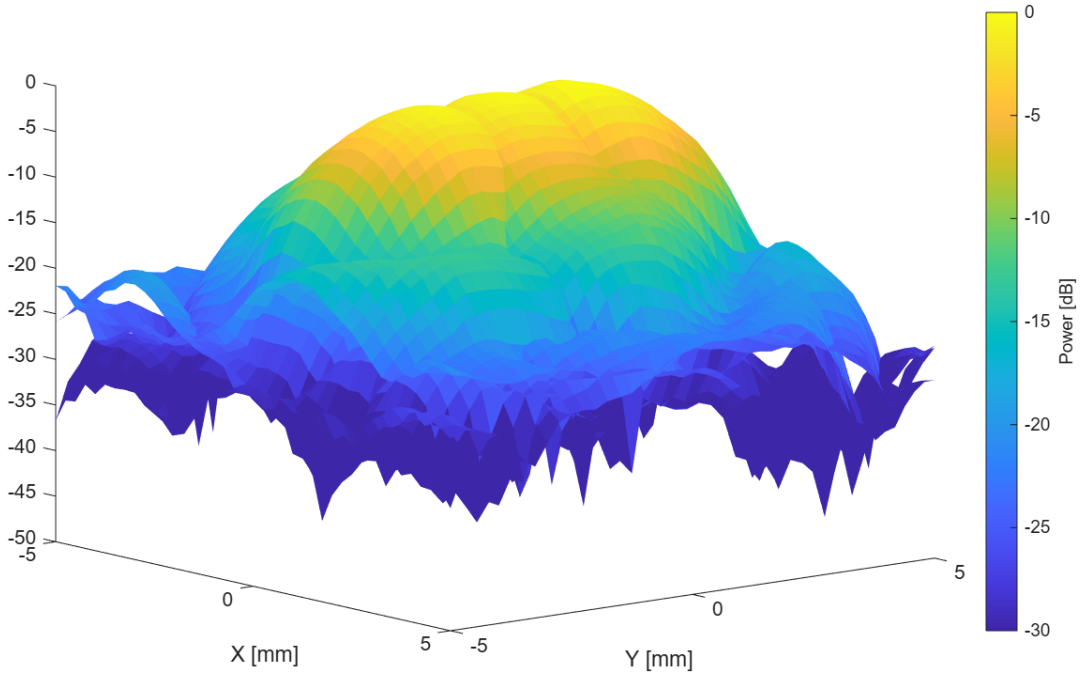

(b) 3D-view of the radiation pattern.

Figure C.1: Obtained plots of the radiation pattern at $f = 400GHz$.

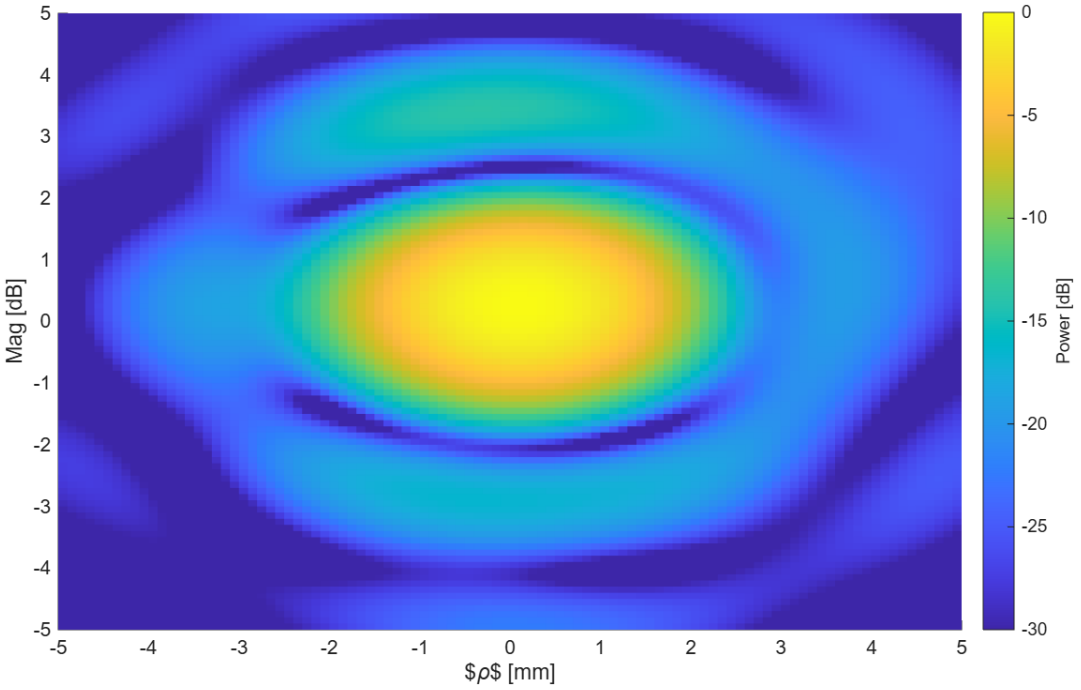

(a) Top view of the radiation pattern.

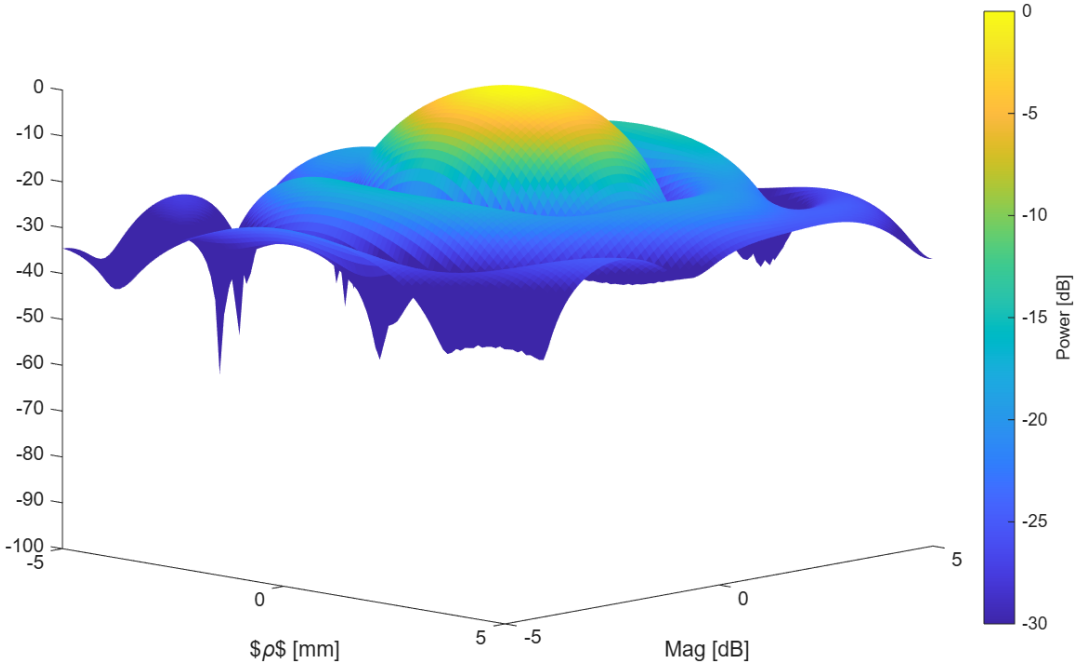

(b) 3D-view of the radiation pattern.

Figure C.2: Single pixel radiation pattern at $f = 400GHz$.

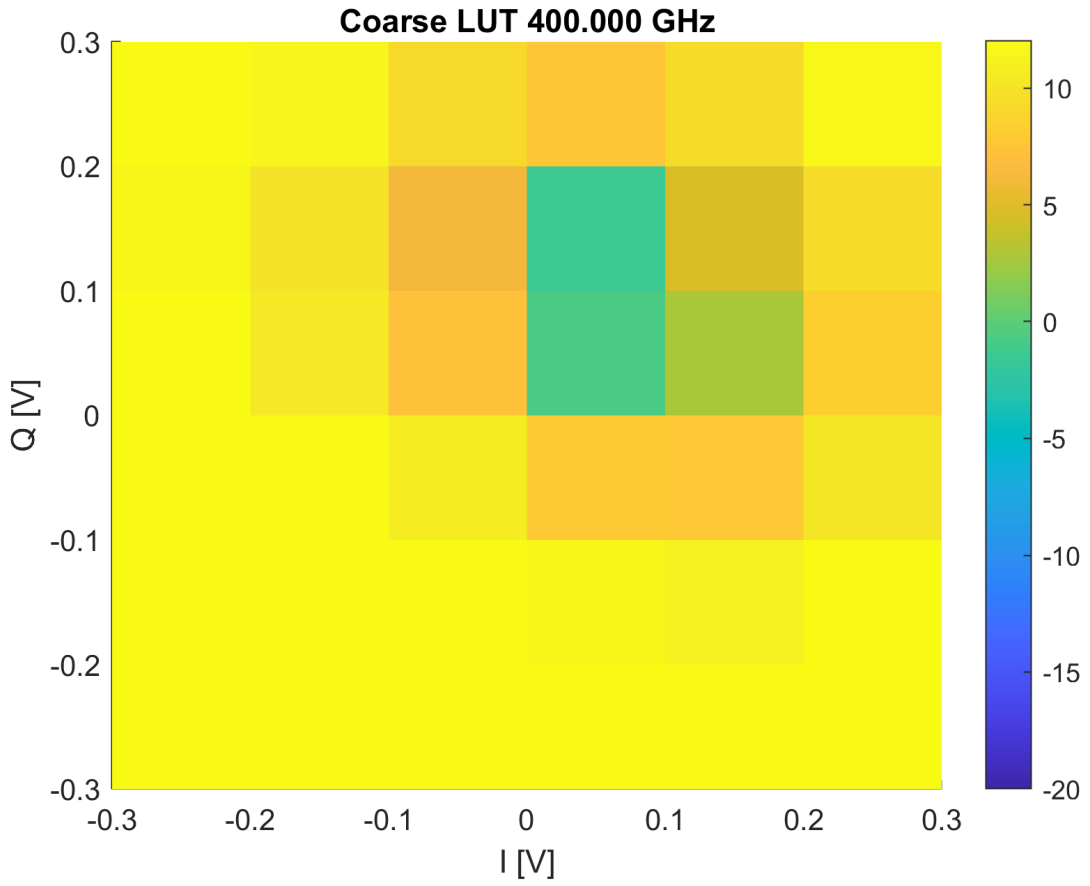

(a) Coarse scan over I and Q voltages.

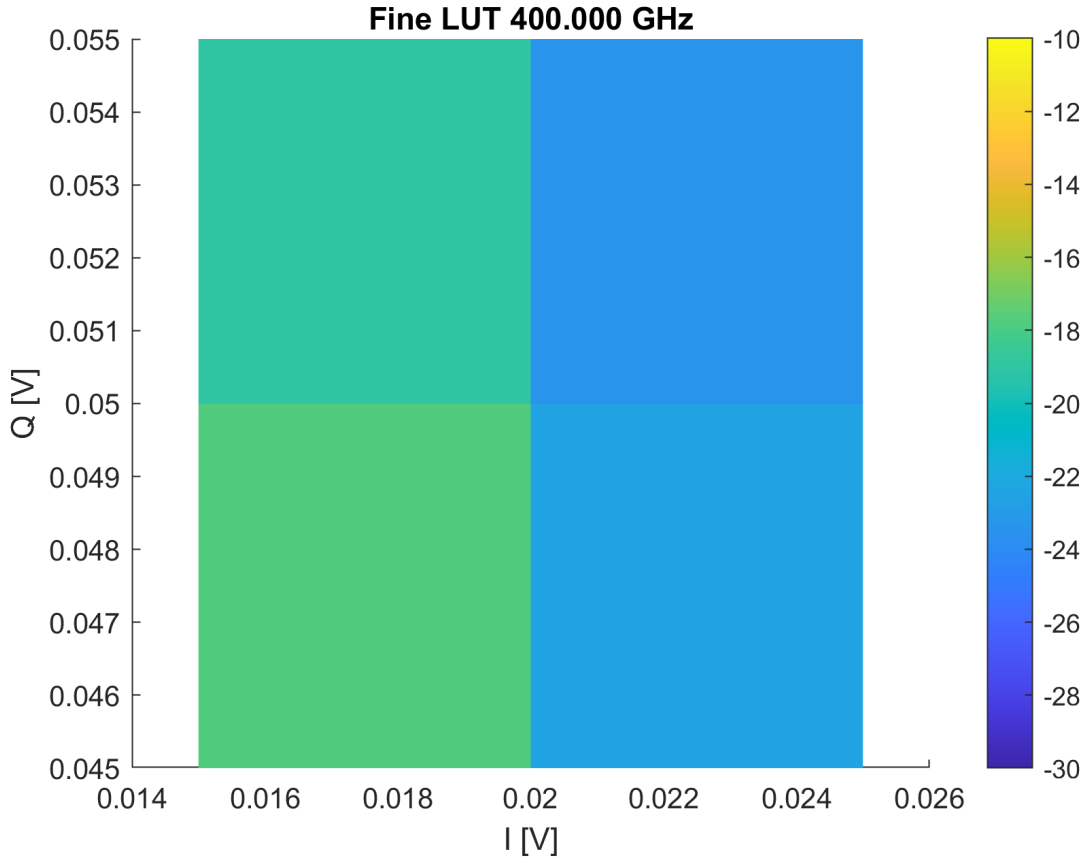

(b) Fine scan over I and Q voltages.

Figure C.3: LUT at a frequency $f = 400GHz$.

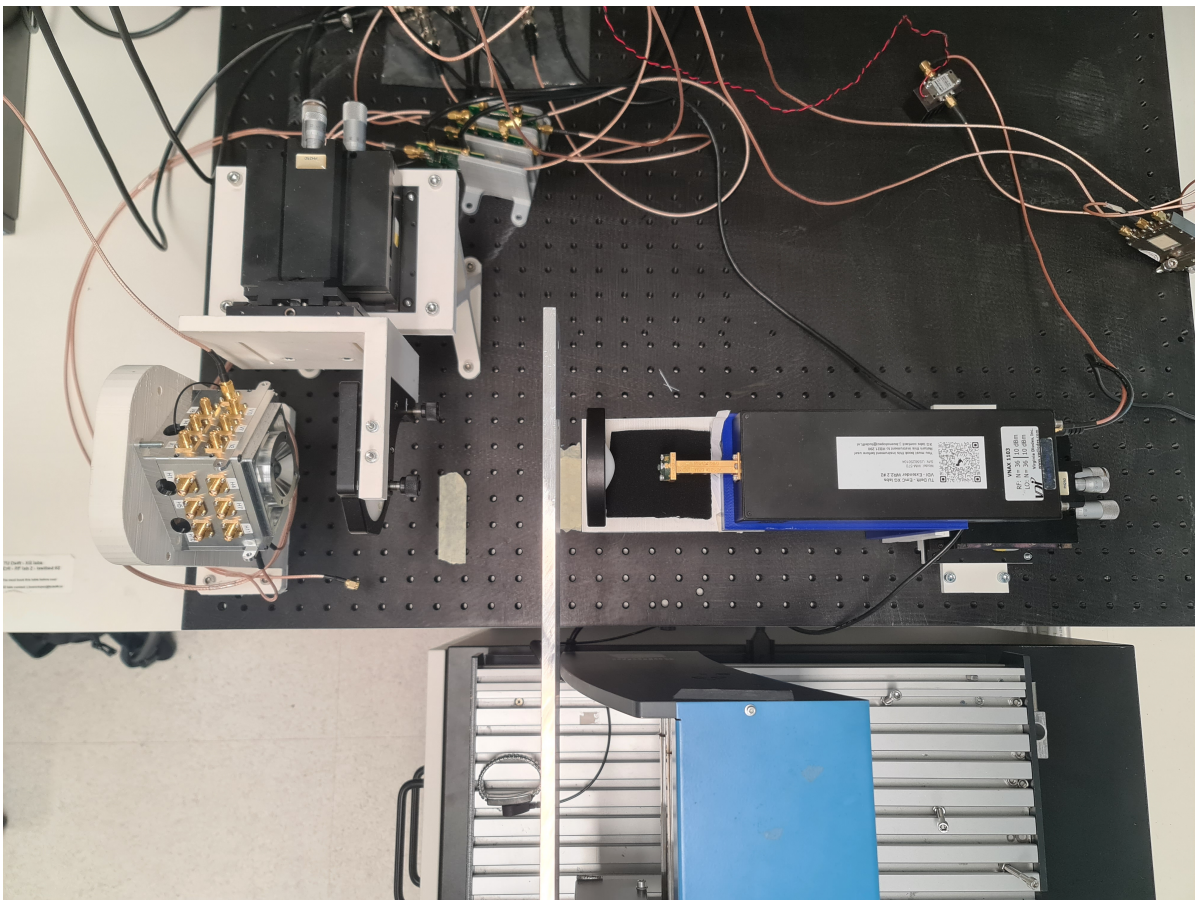

Figure C.4: Top view of the Quasi-optical setup.

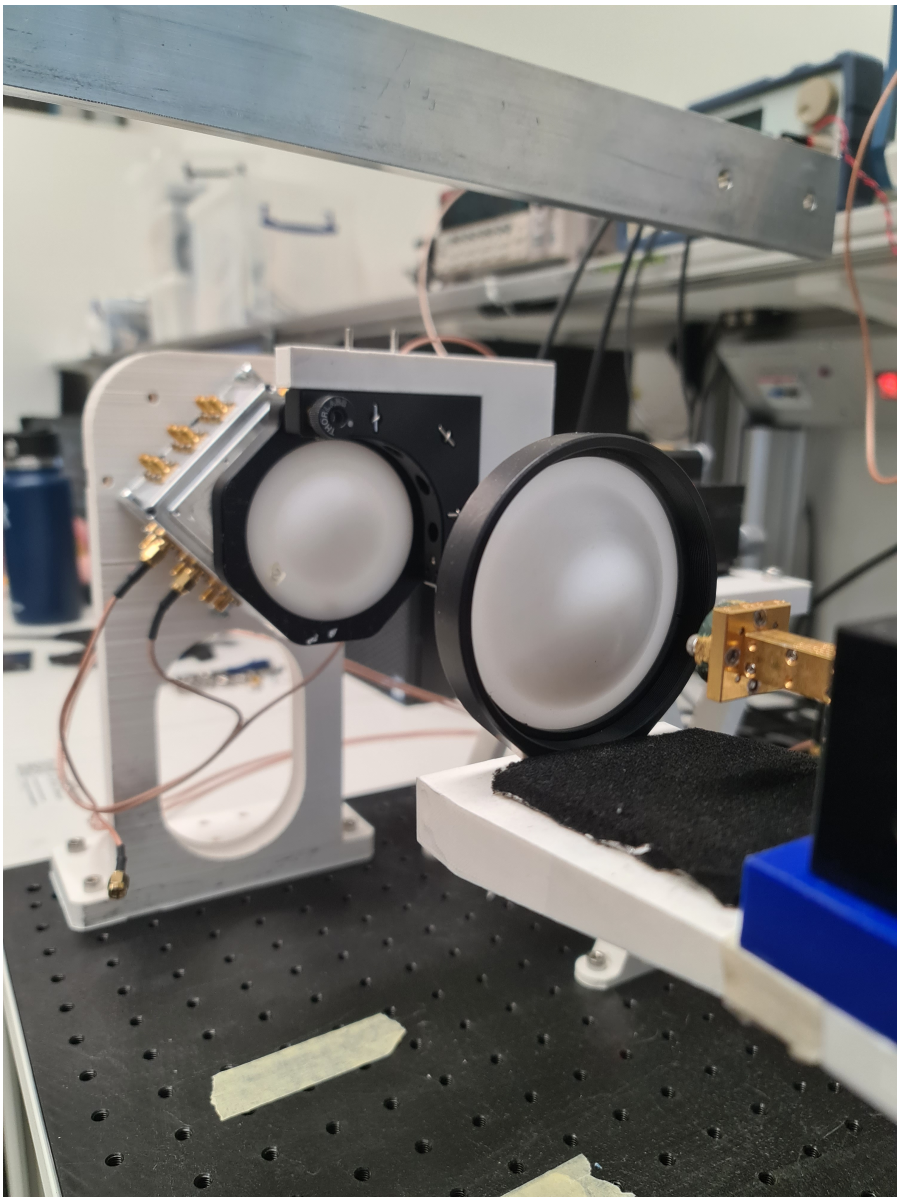

Figure C.5: Path from frequency extender through planoconvex and biconvex lens.

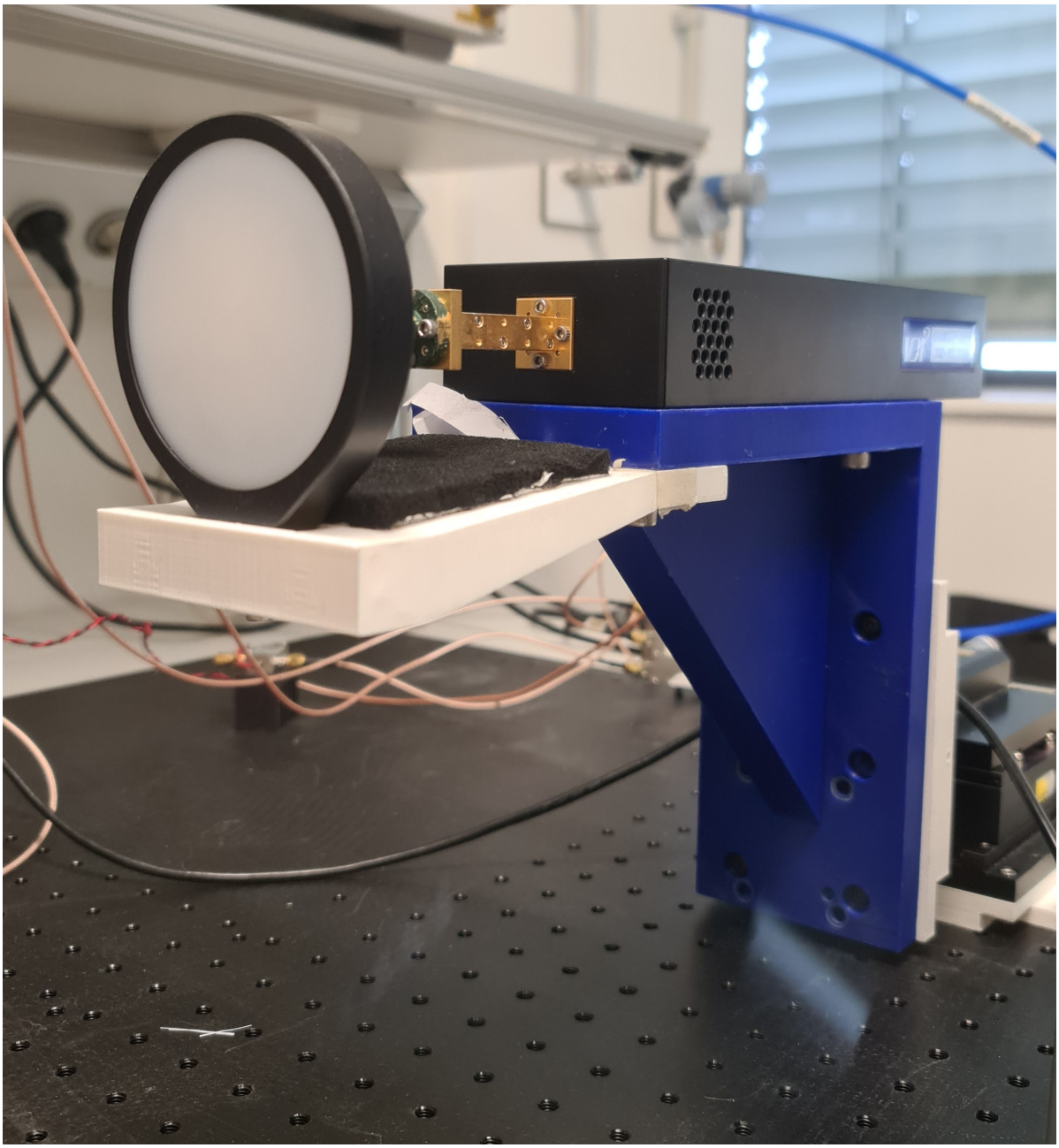

Figure C.6: Frequency extender and planoconvex lens placed on their mount in the final system.

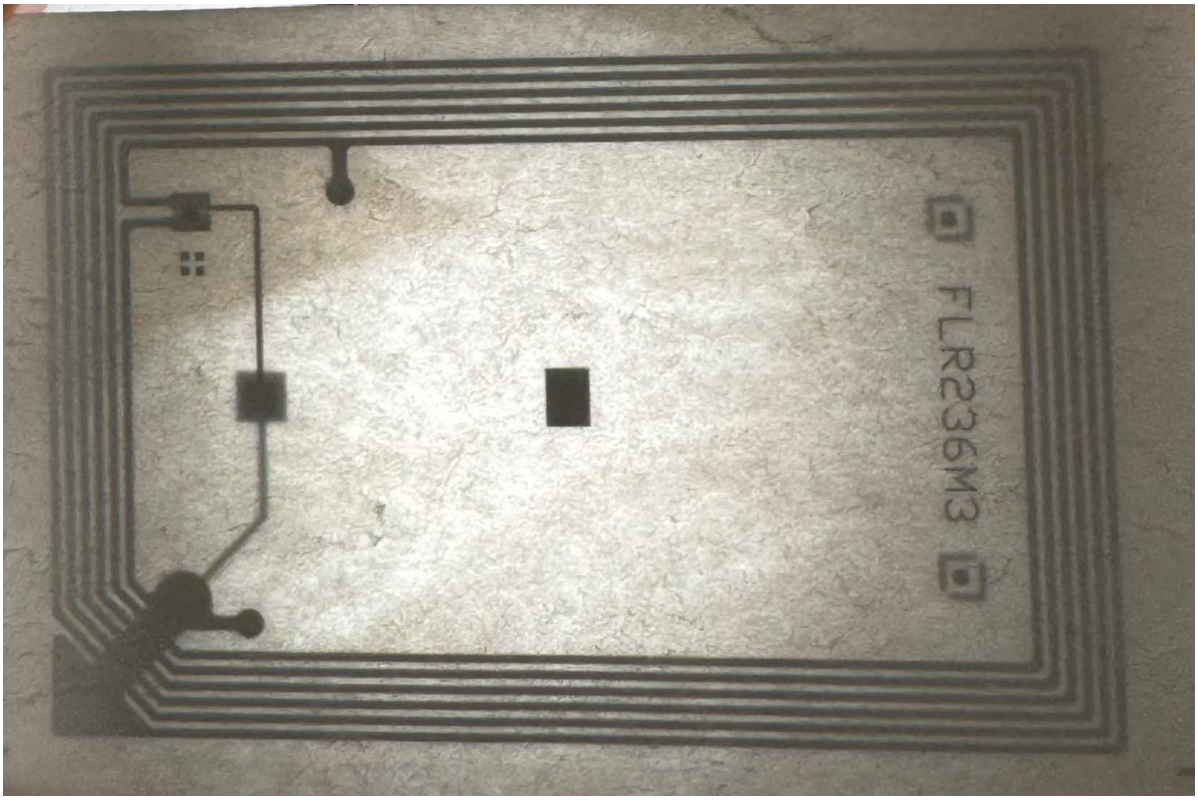

Figure C.7: Inside of the metro ticket. Illuminated with a flashlight from the back.

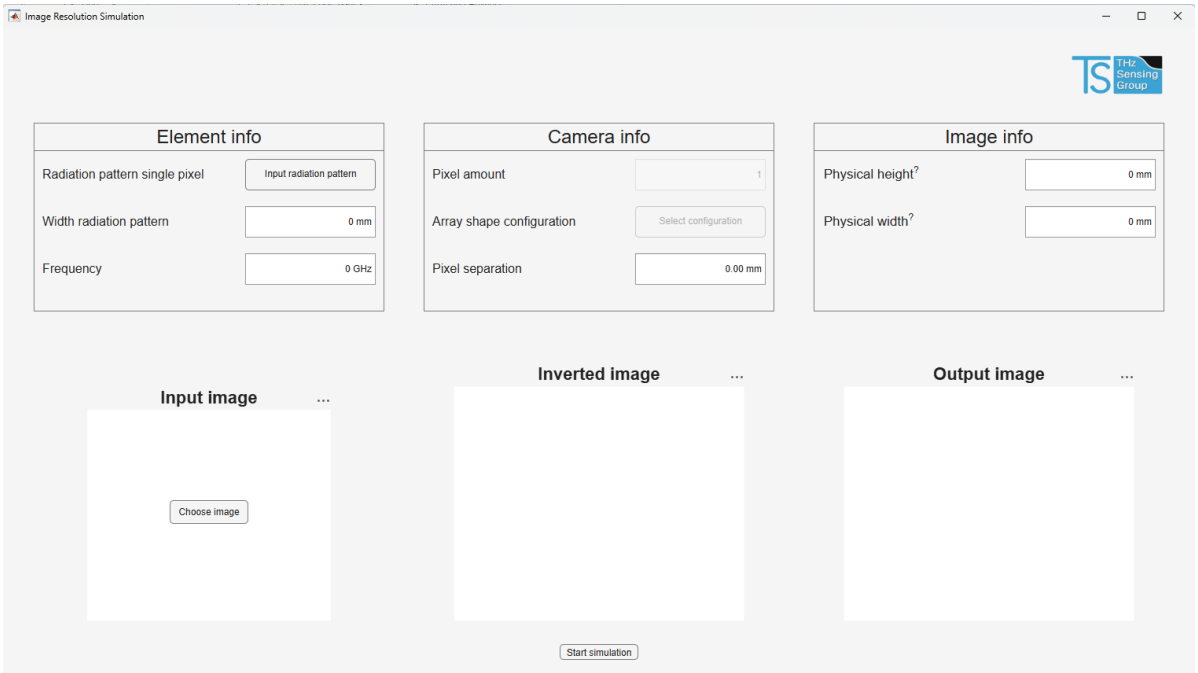

Figure C.8: Image resolution simulation GUI at startup.

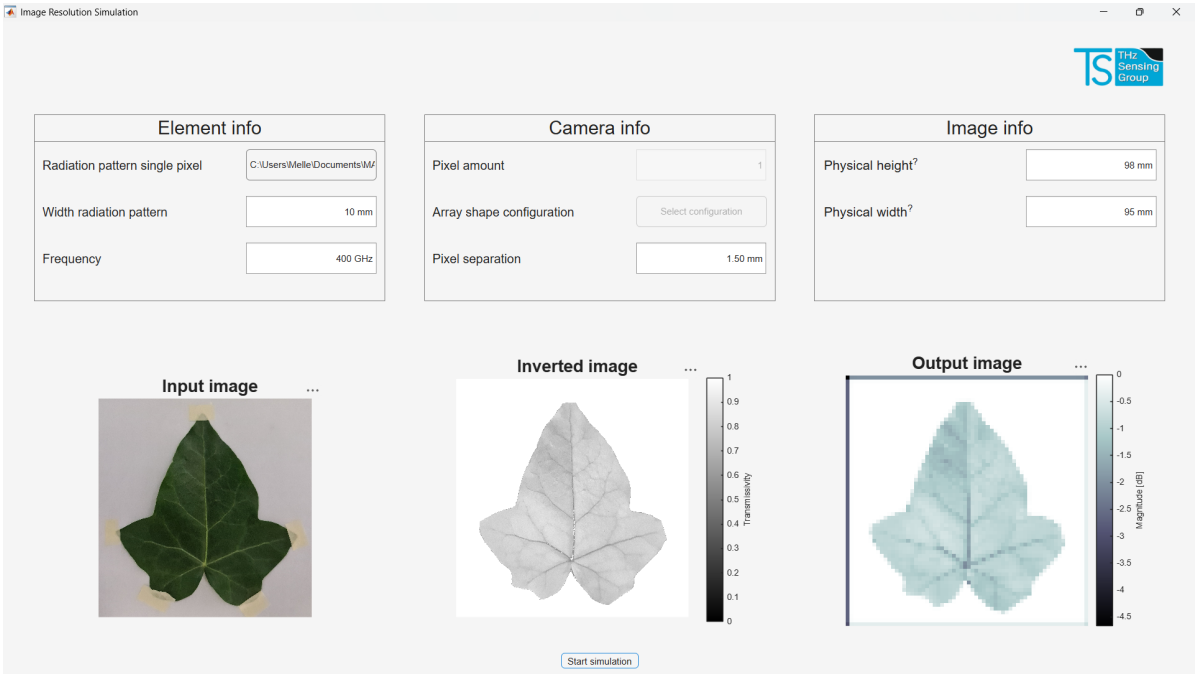

Figure C.9: Image resolution simulation GUI after simulation.

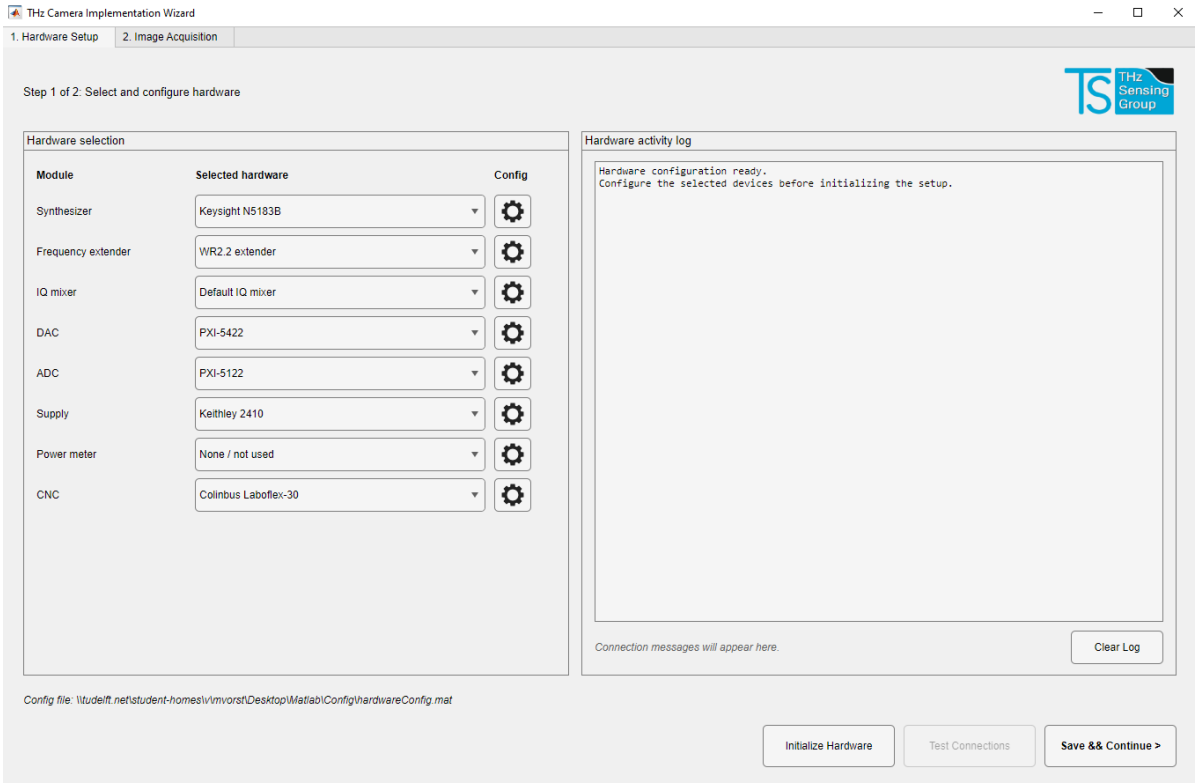

Figure C.10: Hardware selection tab in the hardware GUI.

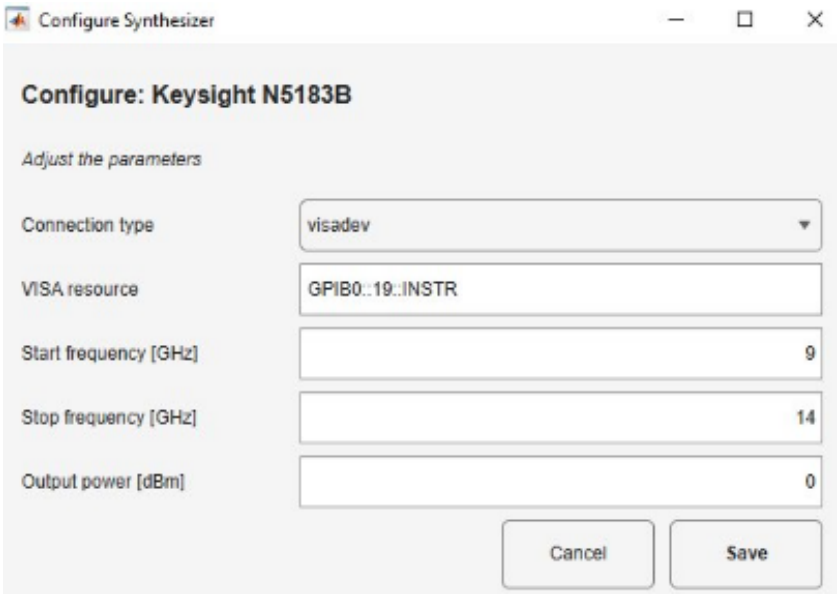

Figure C.11: Configure tab in the hardware GUI.

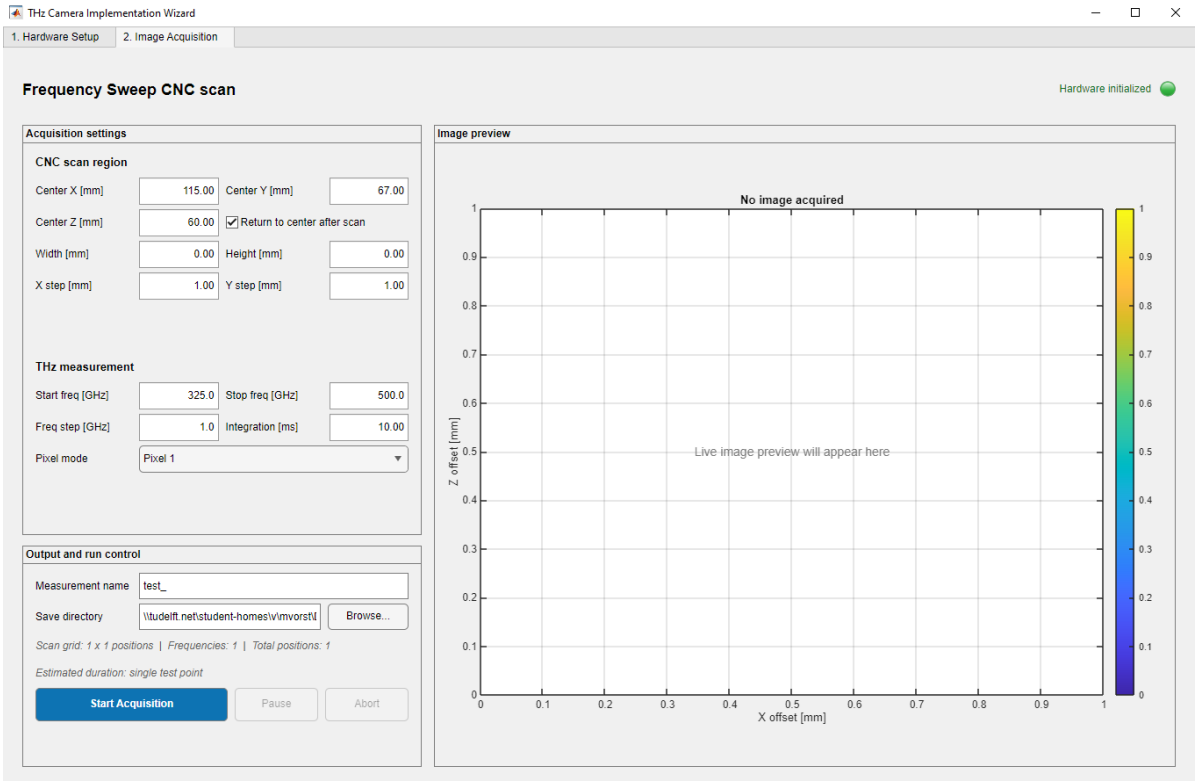

Figure C.12: Image acquisition tab in the hardware GUI.

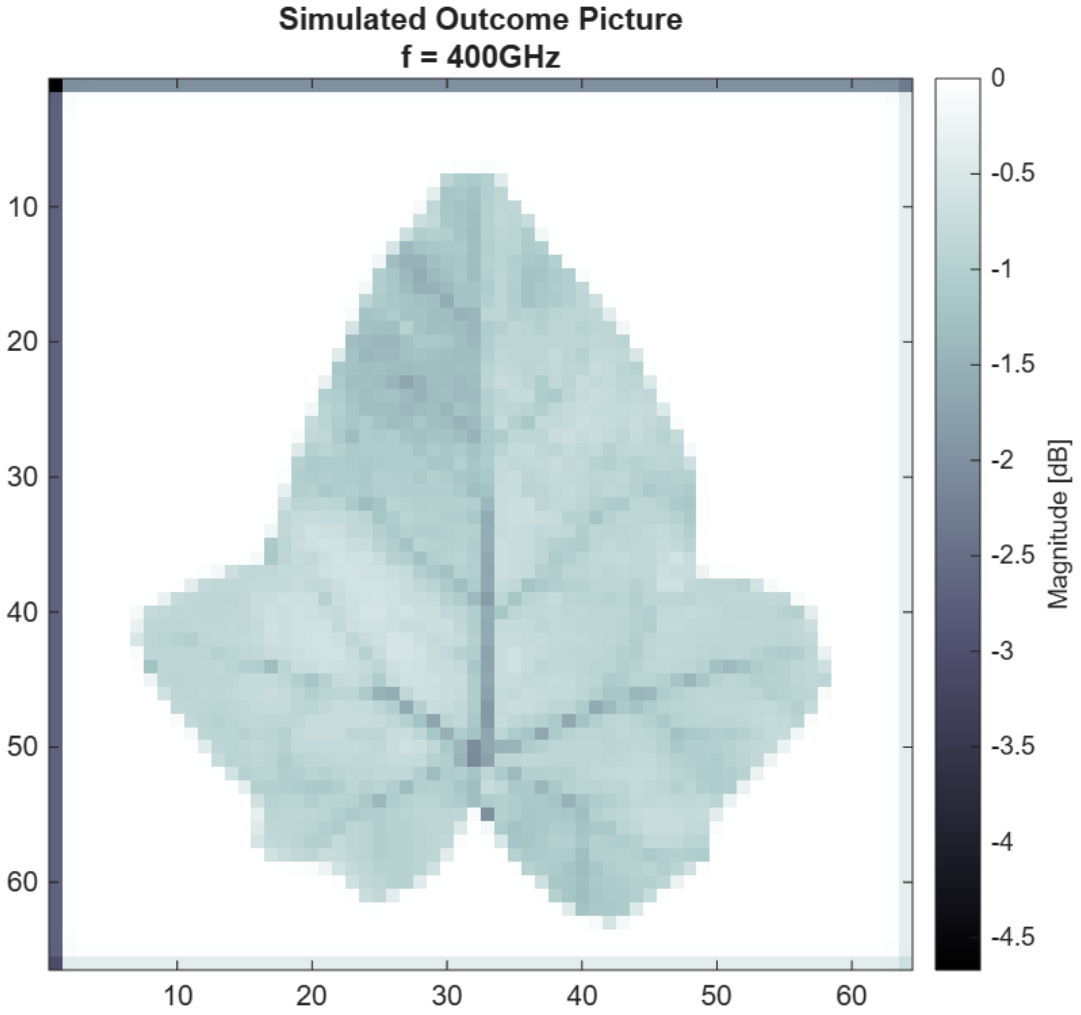

(a) Simulated image at $f = 400GHz$.

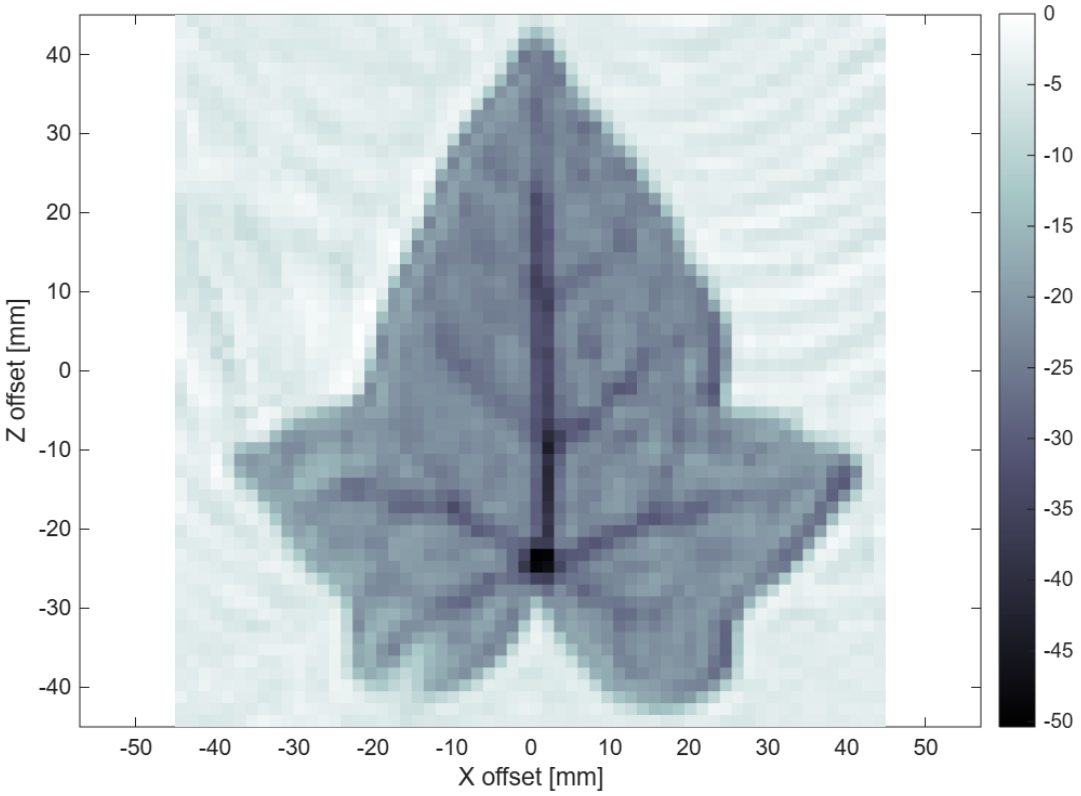

(b) THz outcome image at $f = 400GHz$.

Figure C.13: Simulated image with actual THz image at $f = 400GHz$.

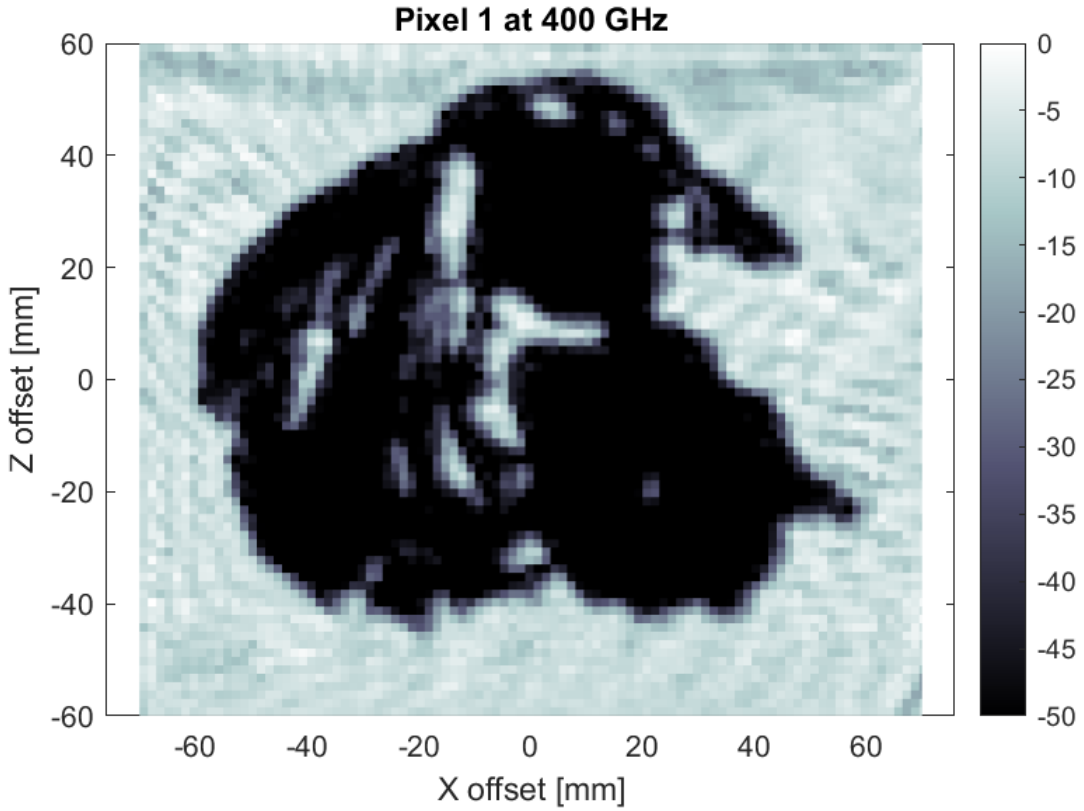

Figure C.14: Raw image of bacon at 400 GHz.

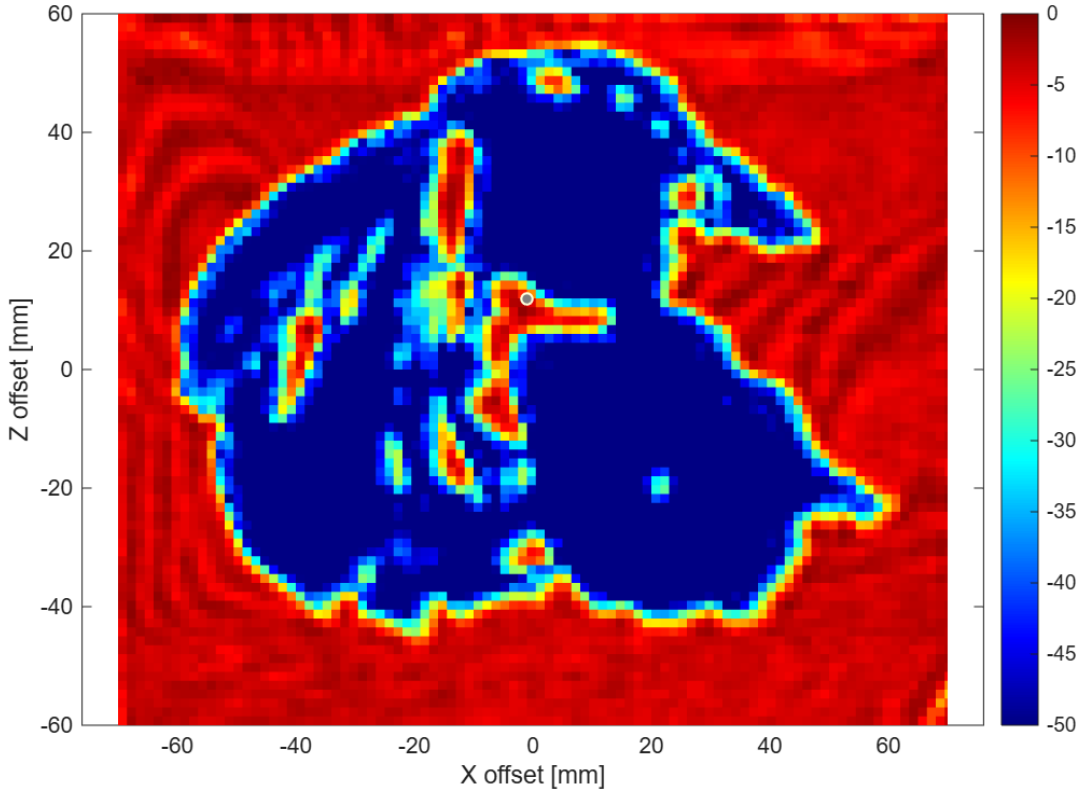

Figure C.15: Frequency-averaged image of bacon around 400 GHz in 'jet' colors.

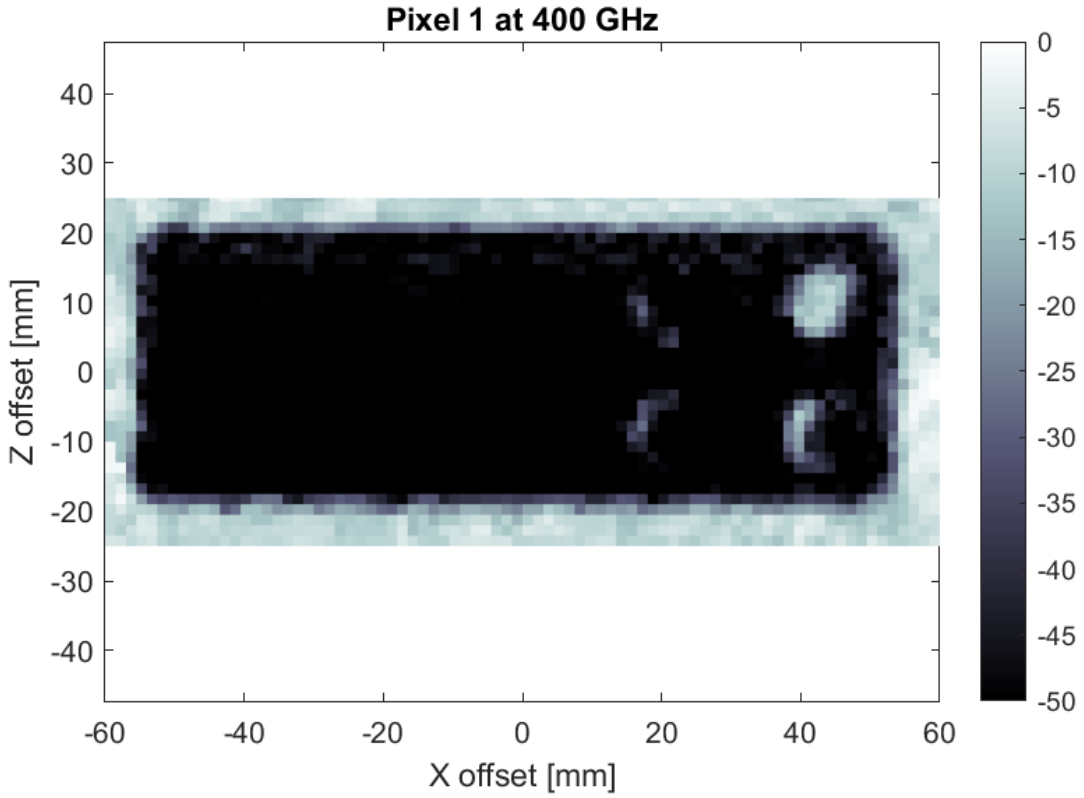

Figure C.16: Raw image of blister pack at 400 GHz.

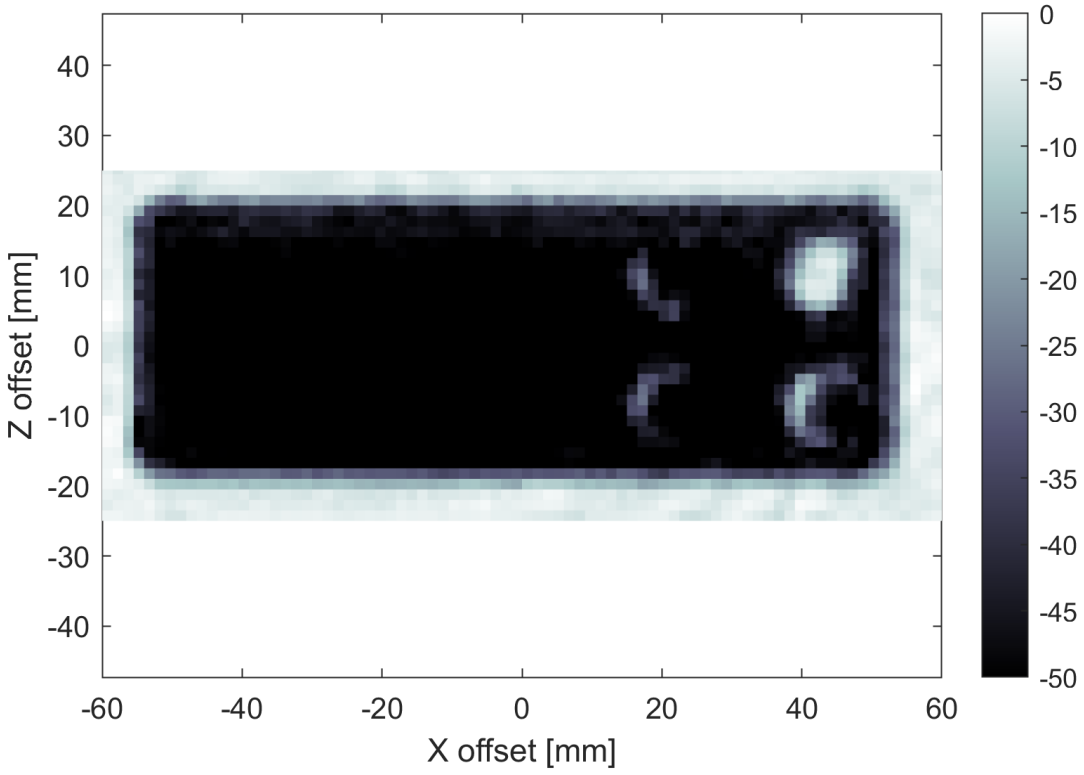

Figure C.17: Frequency-averaged image of blister pack around 400 GHz.

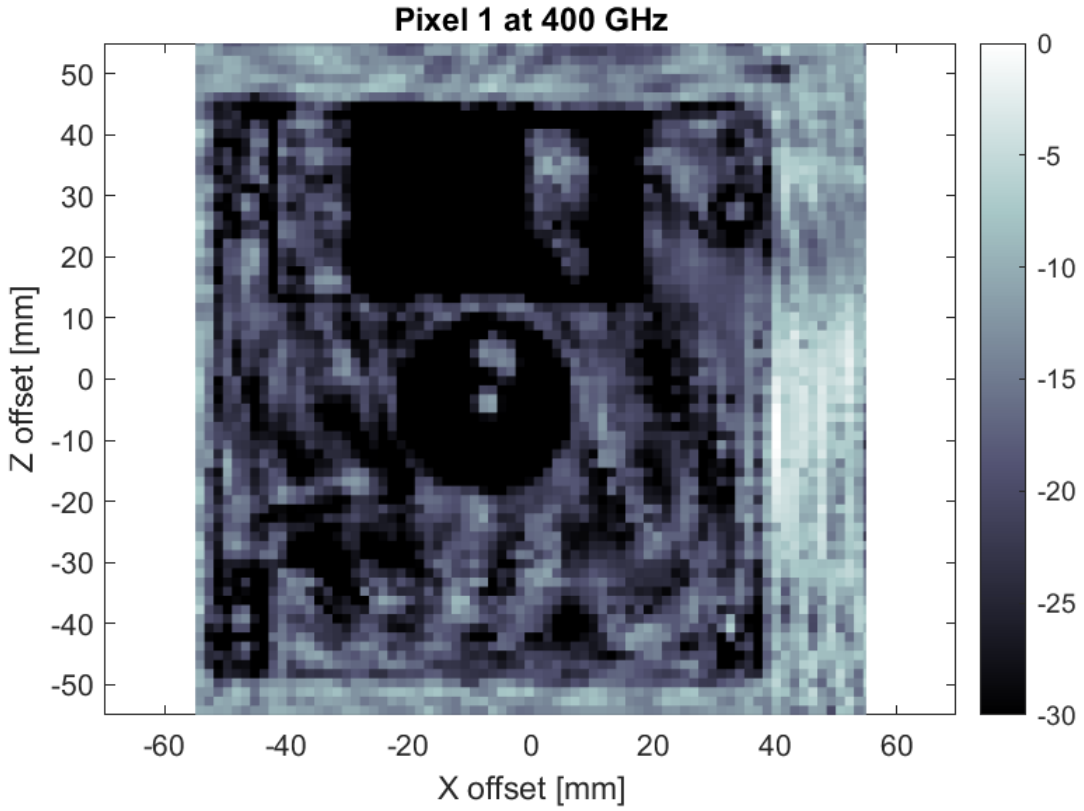

Figure C.18: Raw image of floppy disk at 400 GHz.

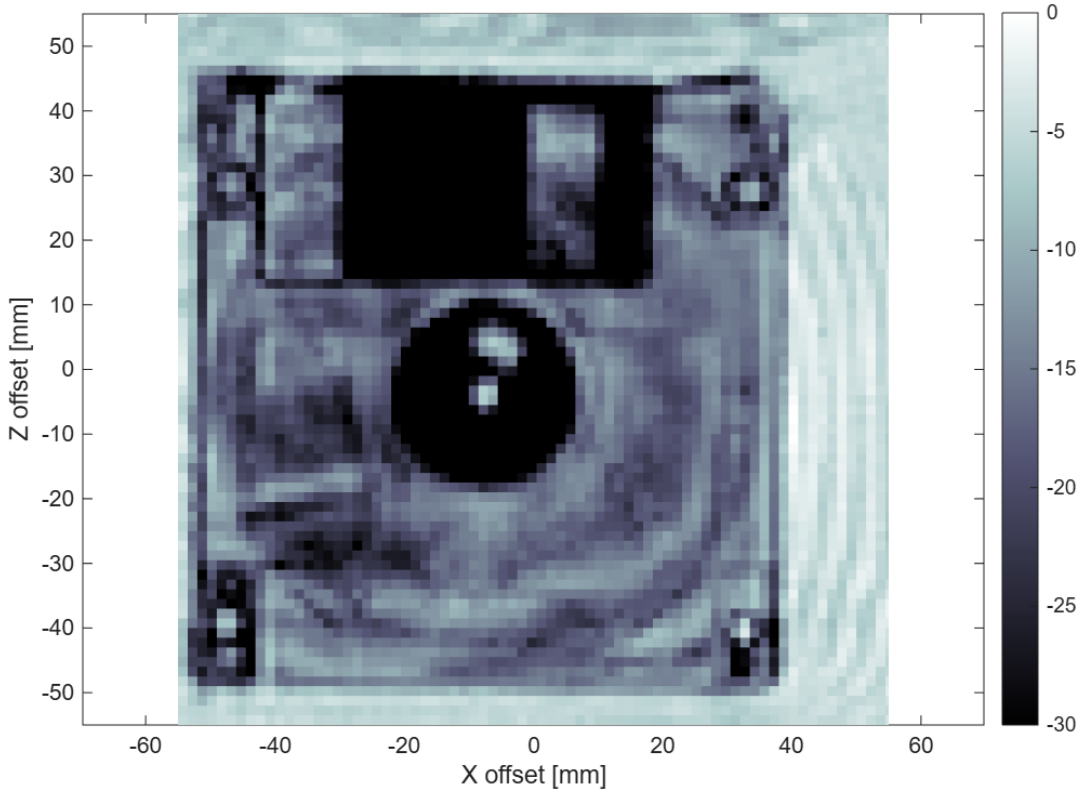

Figure C.19: Frequency-averaged image of floppy disk around 400 GHz.

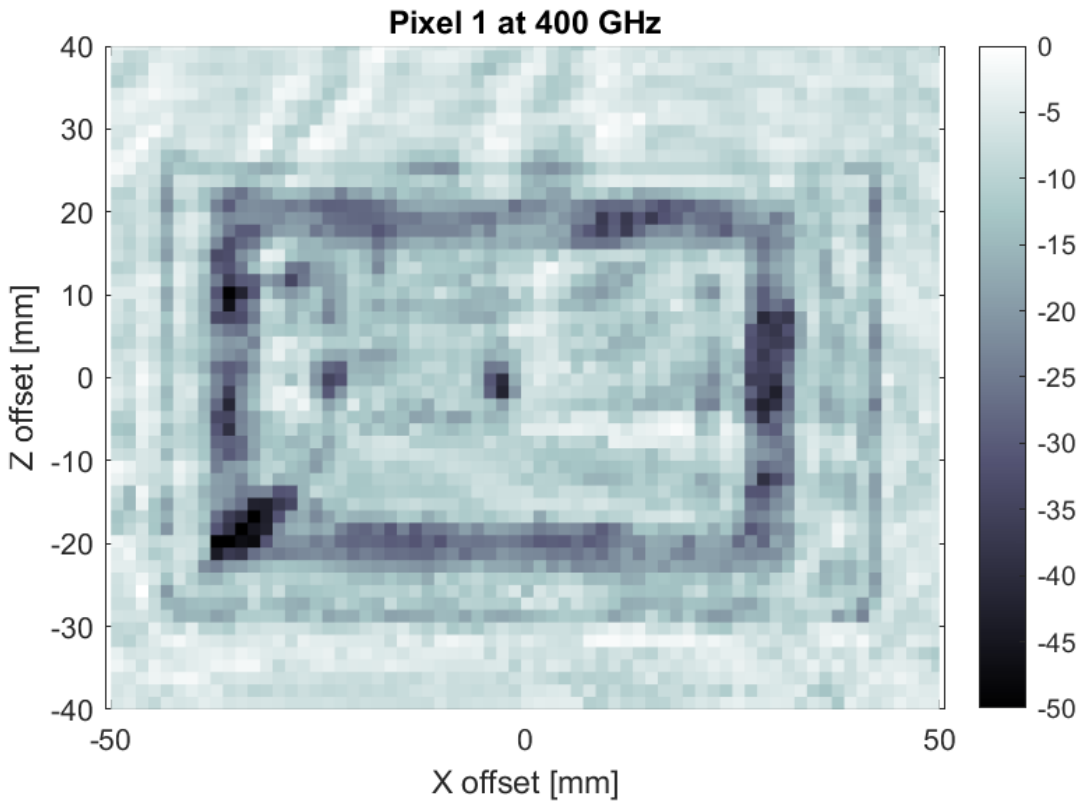

Figure C.20: Raw image of metro card at 400 GHz.

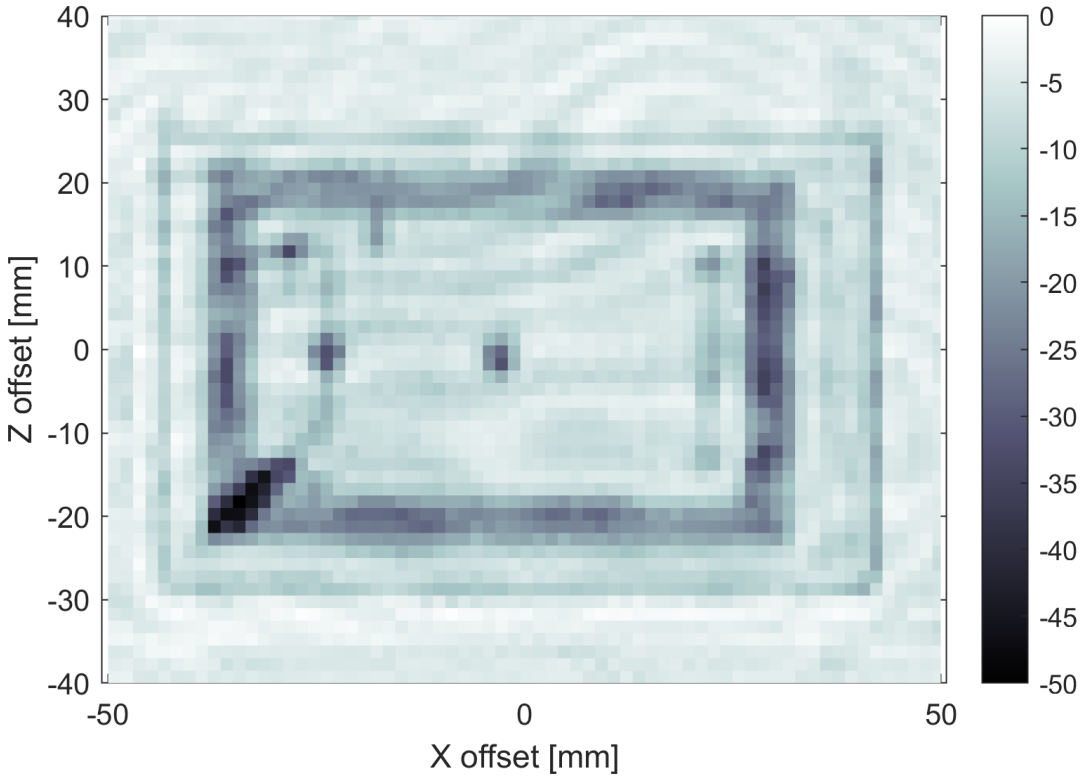

Figure C.21: Frequency-averaged image of metro card around 400 GHz.

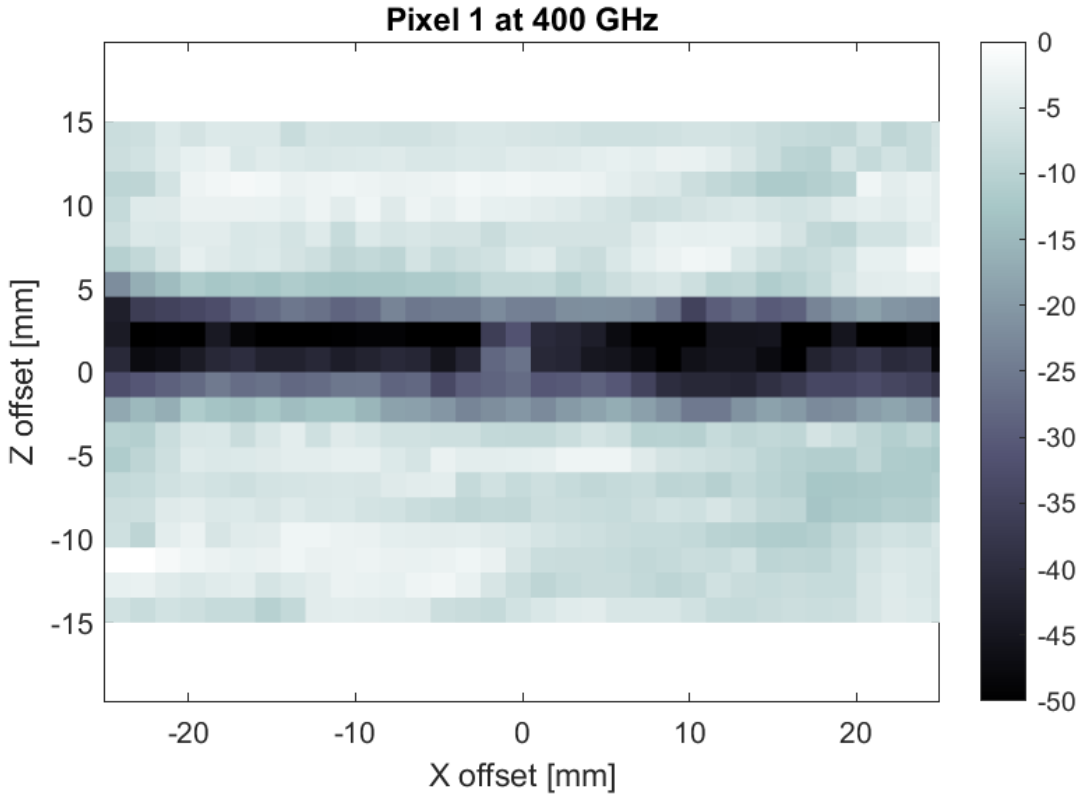

Figure C.22: Raw image of pencil at 400 GHz.

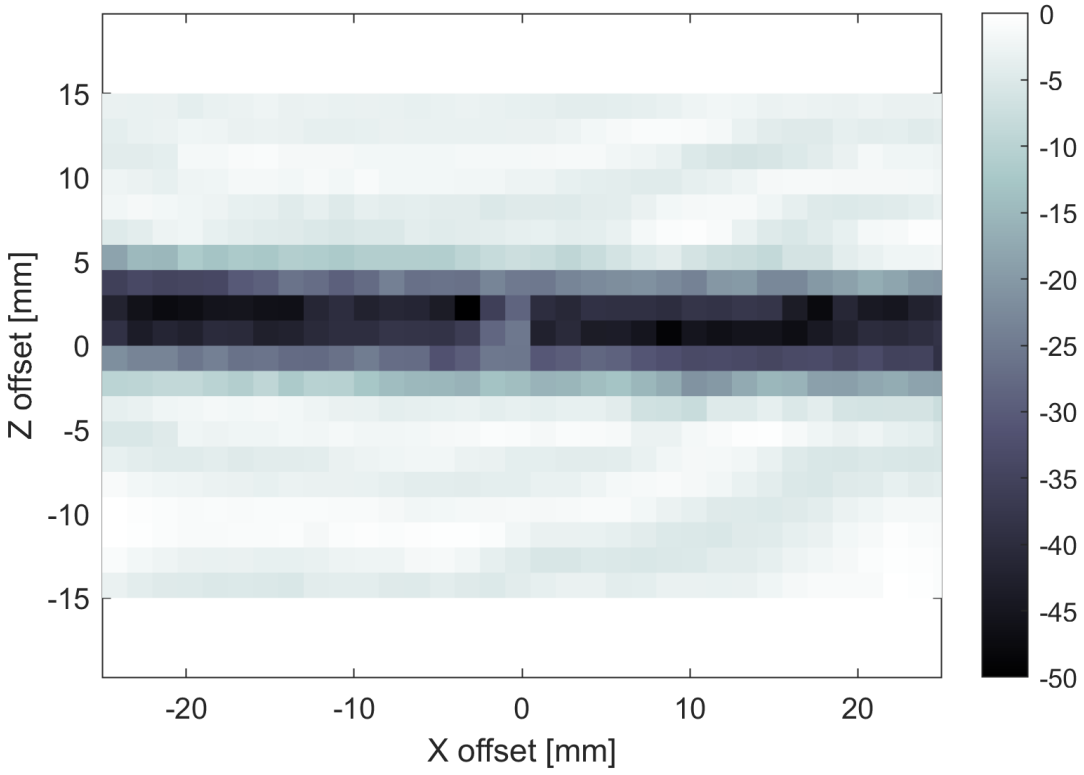

Figure C.23: Frequency-averaged image of pencil around 400 GHz.

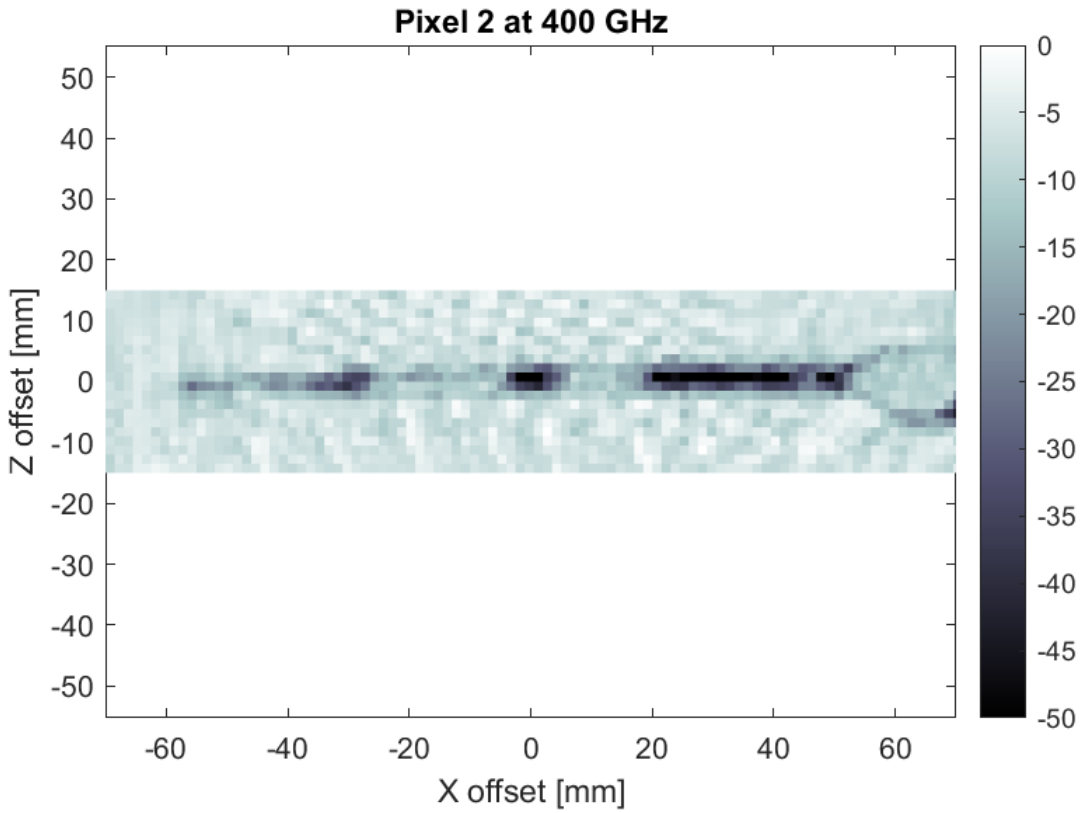

Figure C.24: Raw image of pipette at 400 GHz.

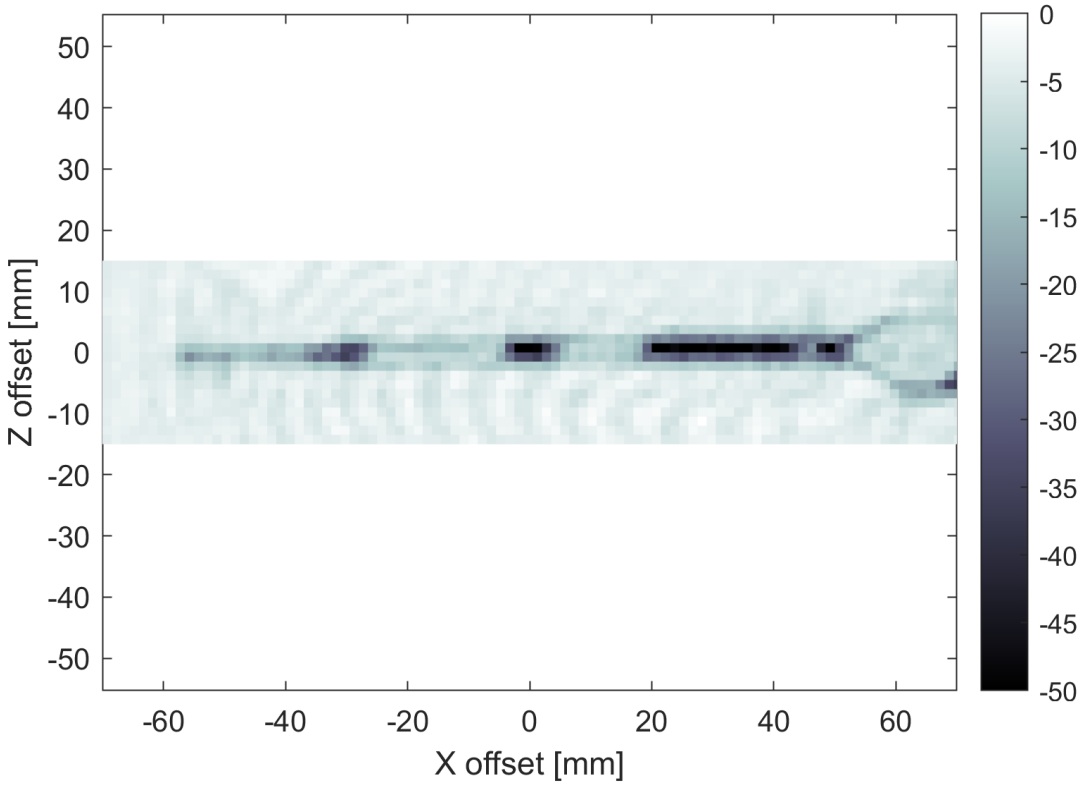

Figure C.25: Frequency-averaged image of pipette around 400 GHz.

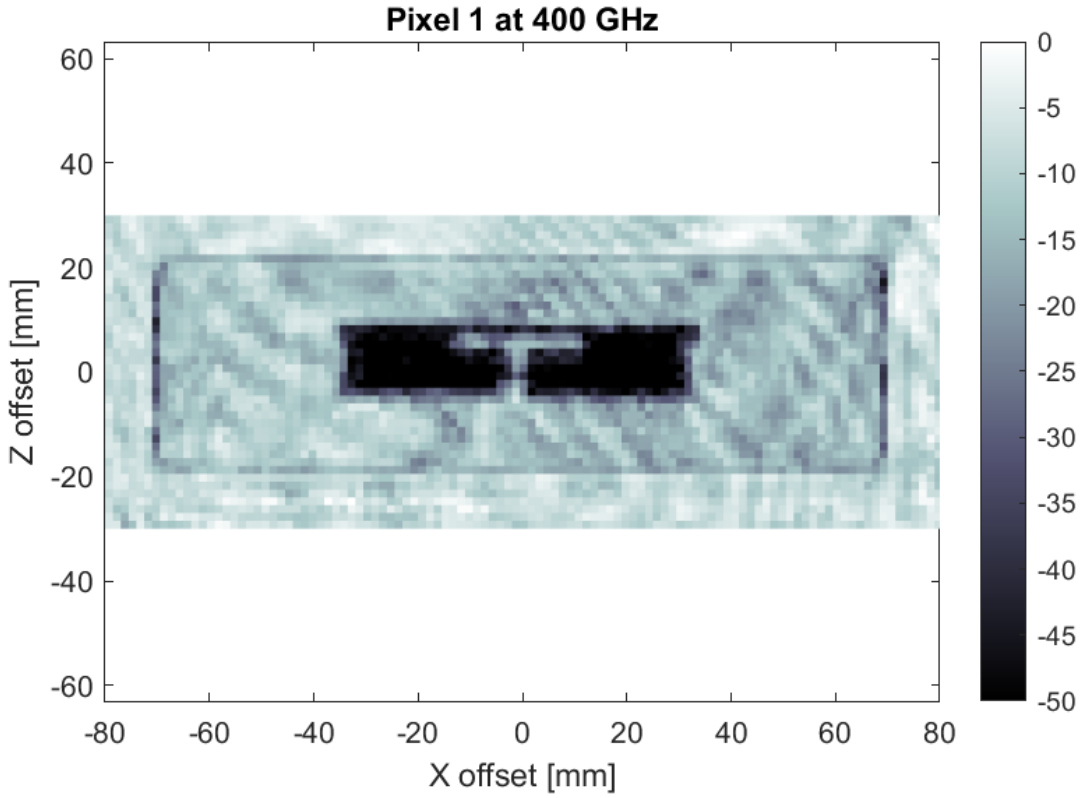

Figure C.26: Raw image of clothing tag at 400 GHz.

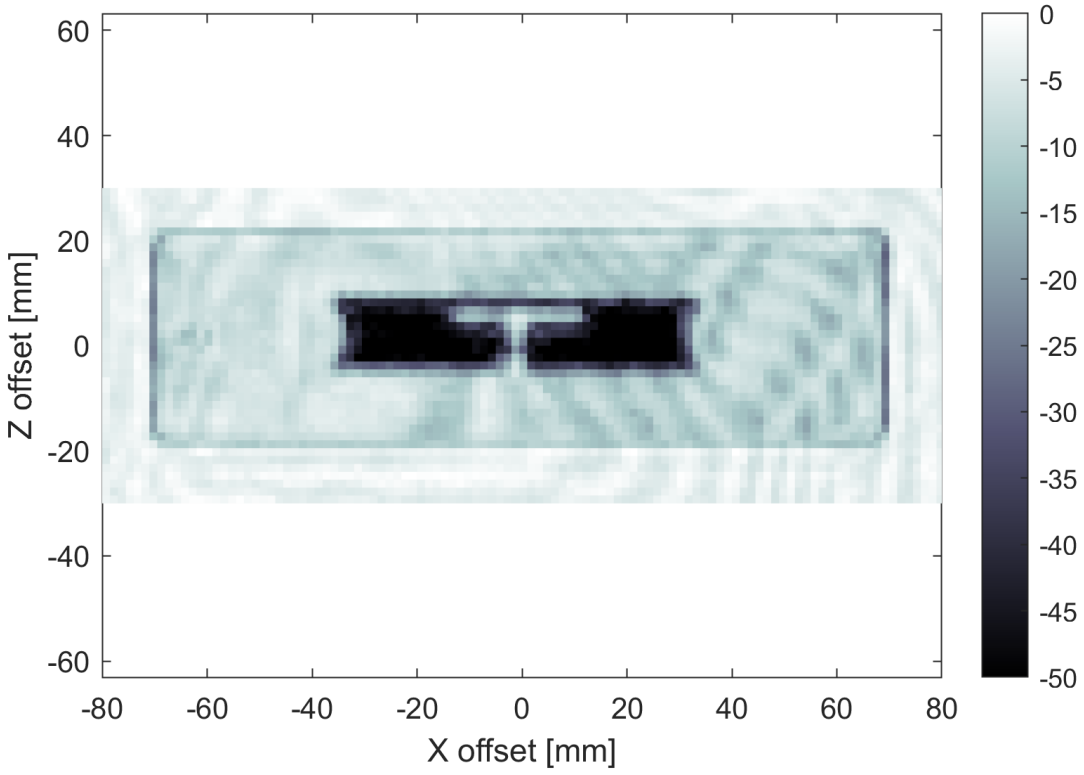

Figure C.27: Frequency-averaged image of clothing tag around 400 GHz.

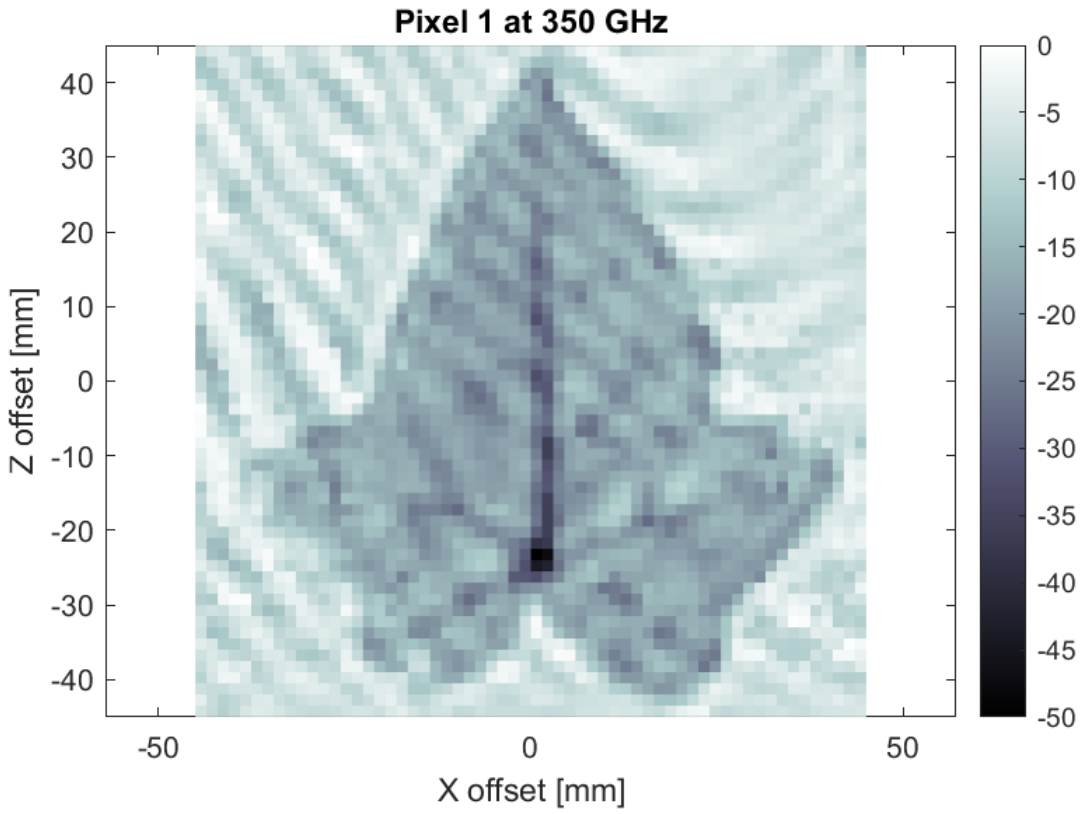

Figure C.28: Raw image of ivy leaf at 350 GHz.

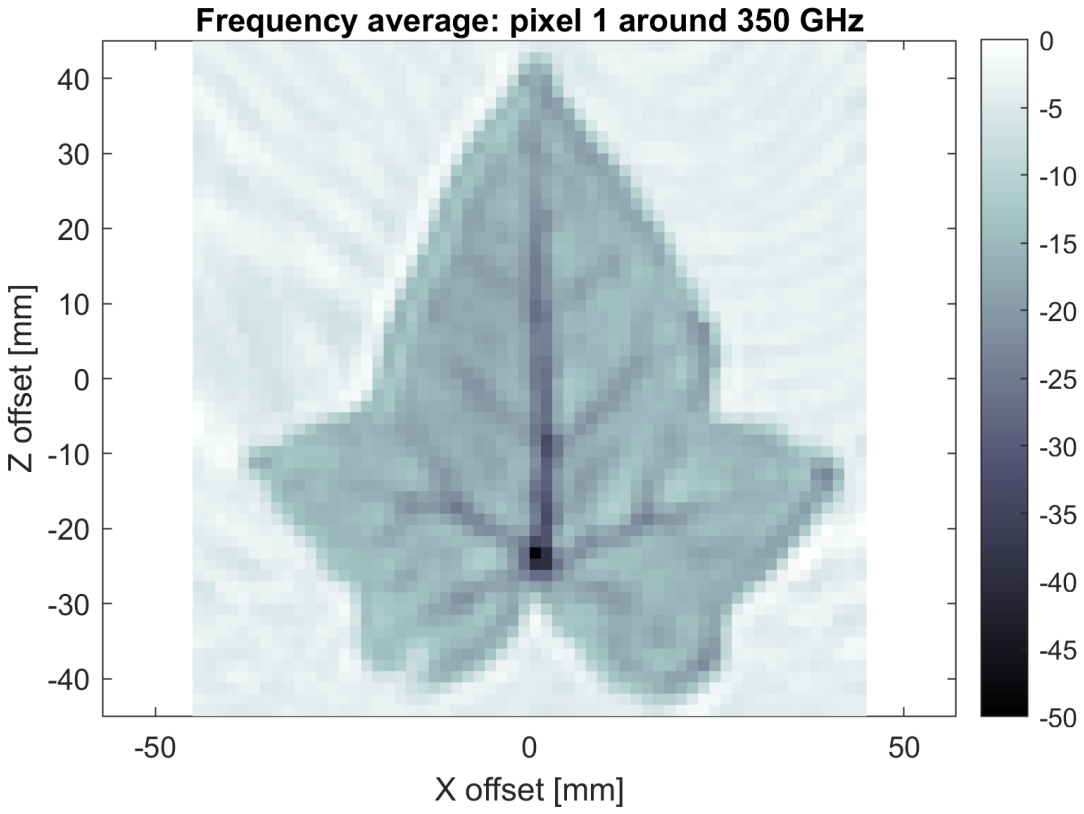

Figure C.29: Frequency-averaged image of ivy leaf around 350 GHz.

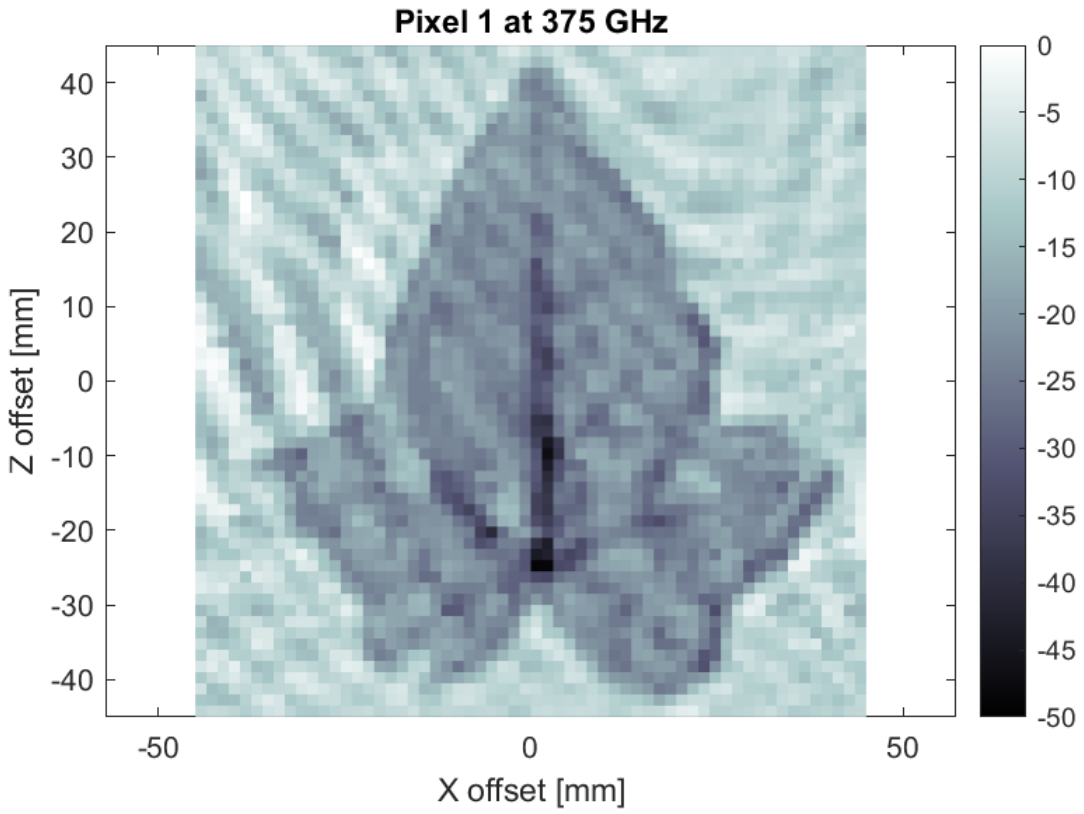

Figure C.30: Raw image of ivy leaf at 375 GHz.

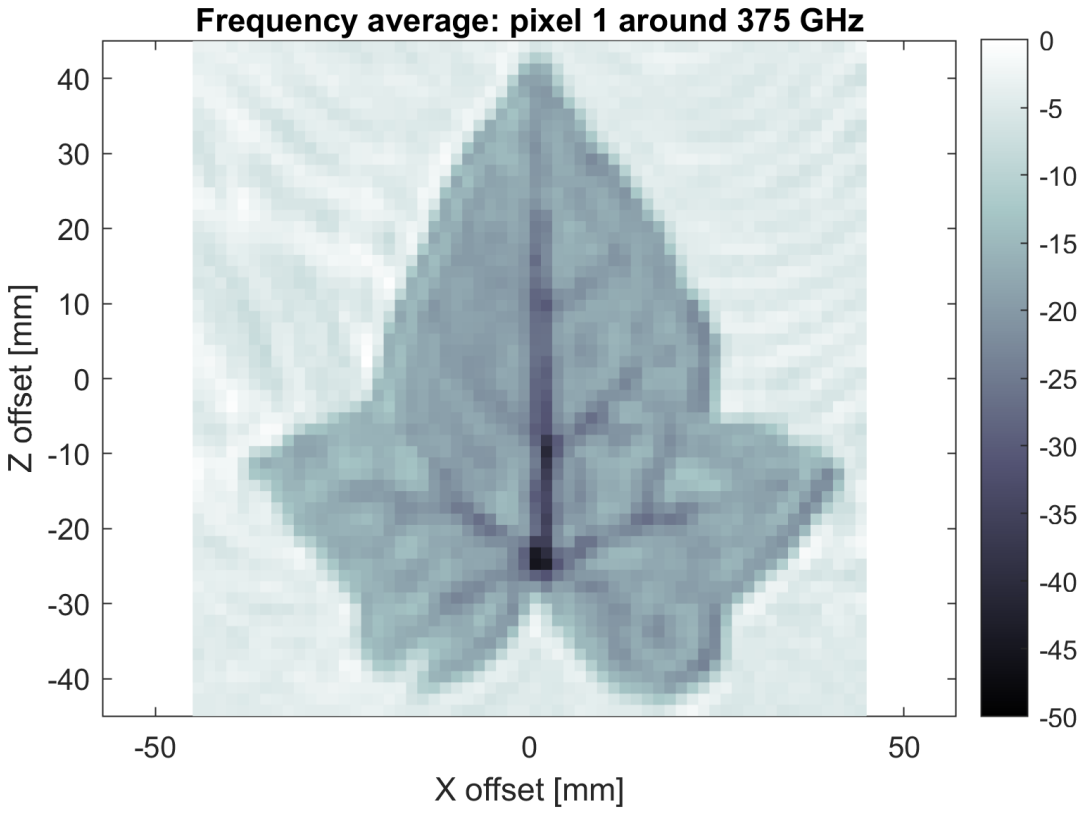

Figure C.31: Frequency-averaged image of ivy leaf around 375 GHz.

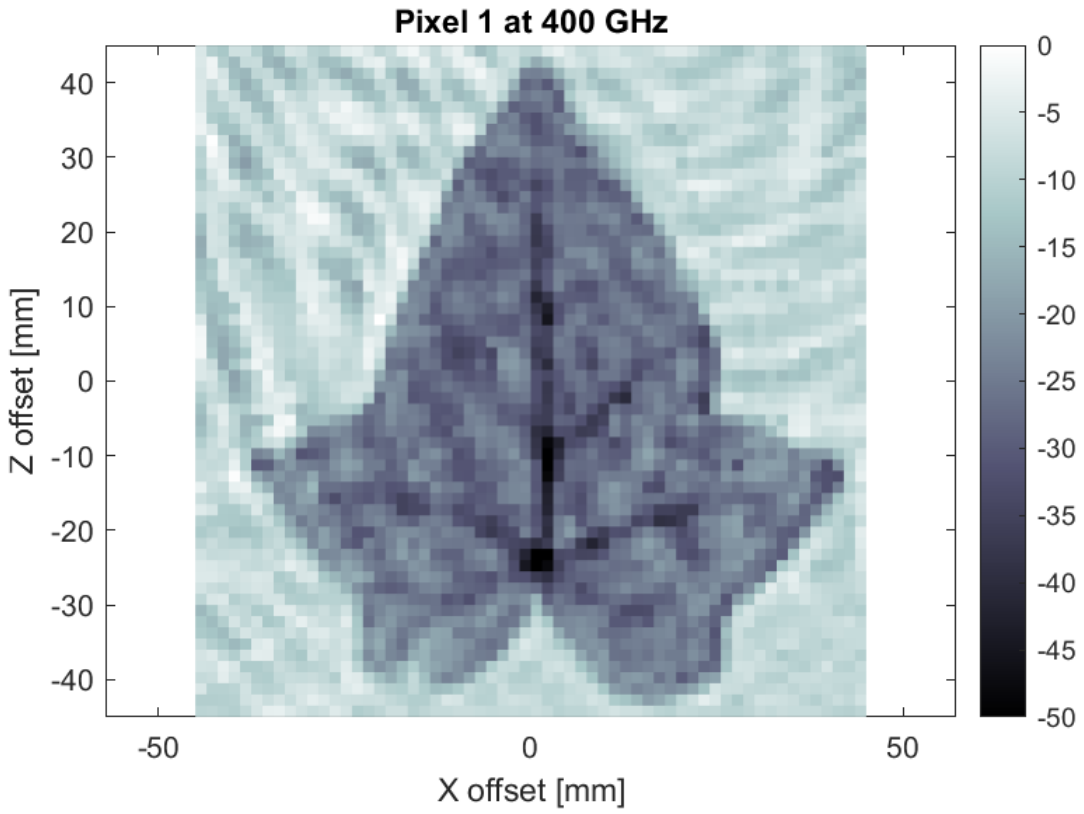

Figure C.32: Raw image of ivy leaf at 400 GHz.

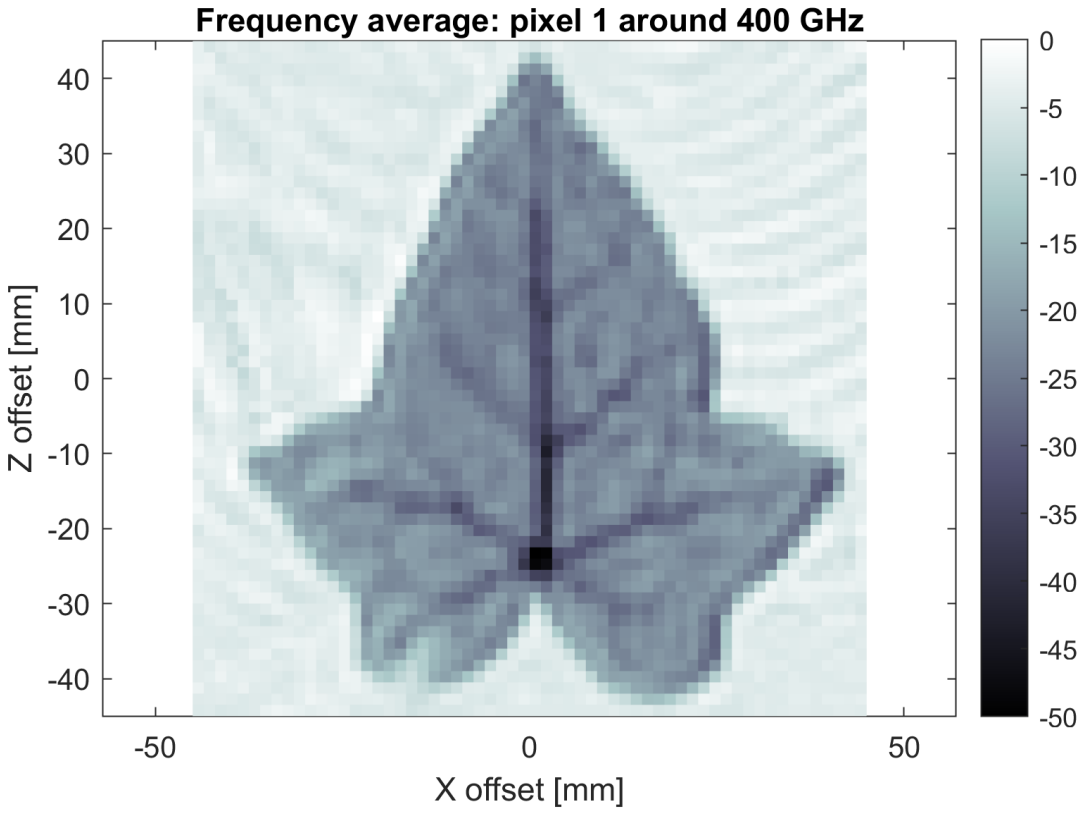

Figure C.33: Frequency-averaged image of ivy leaf around 400 GHz.

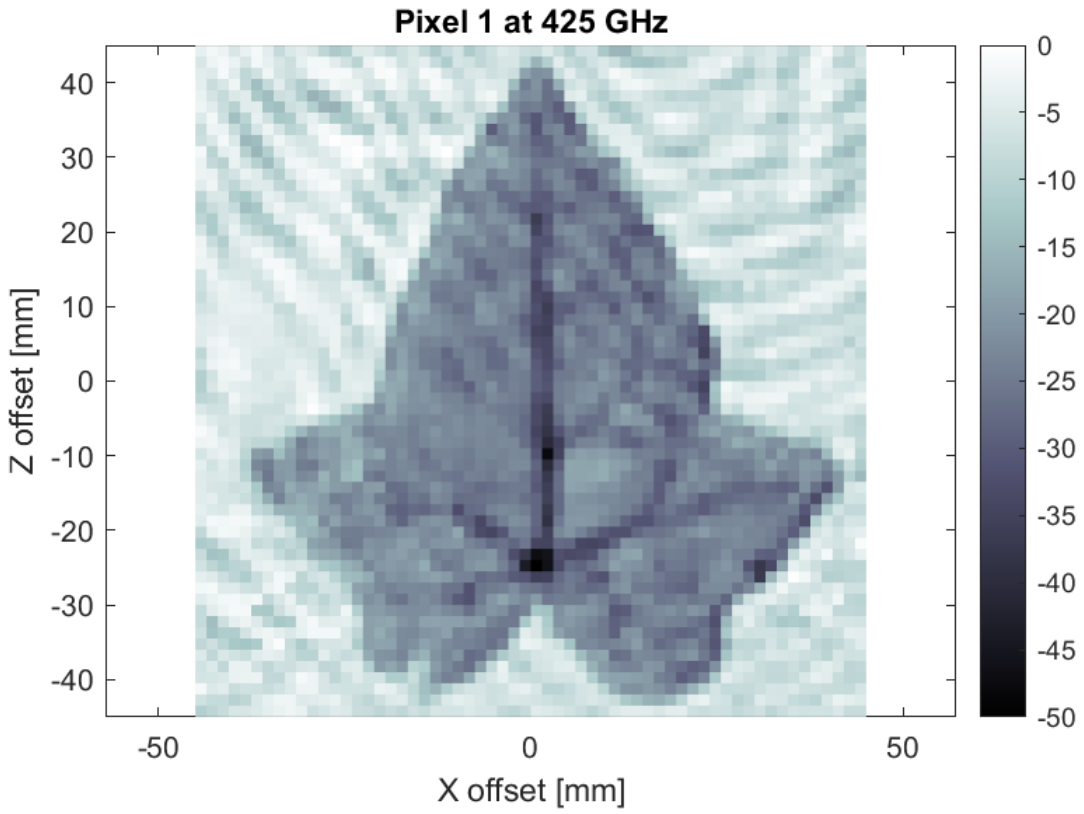

Figure C.34: Raw image of ivy leaf at 425 GHz.

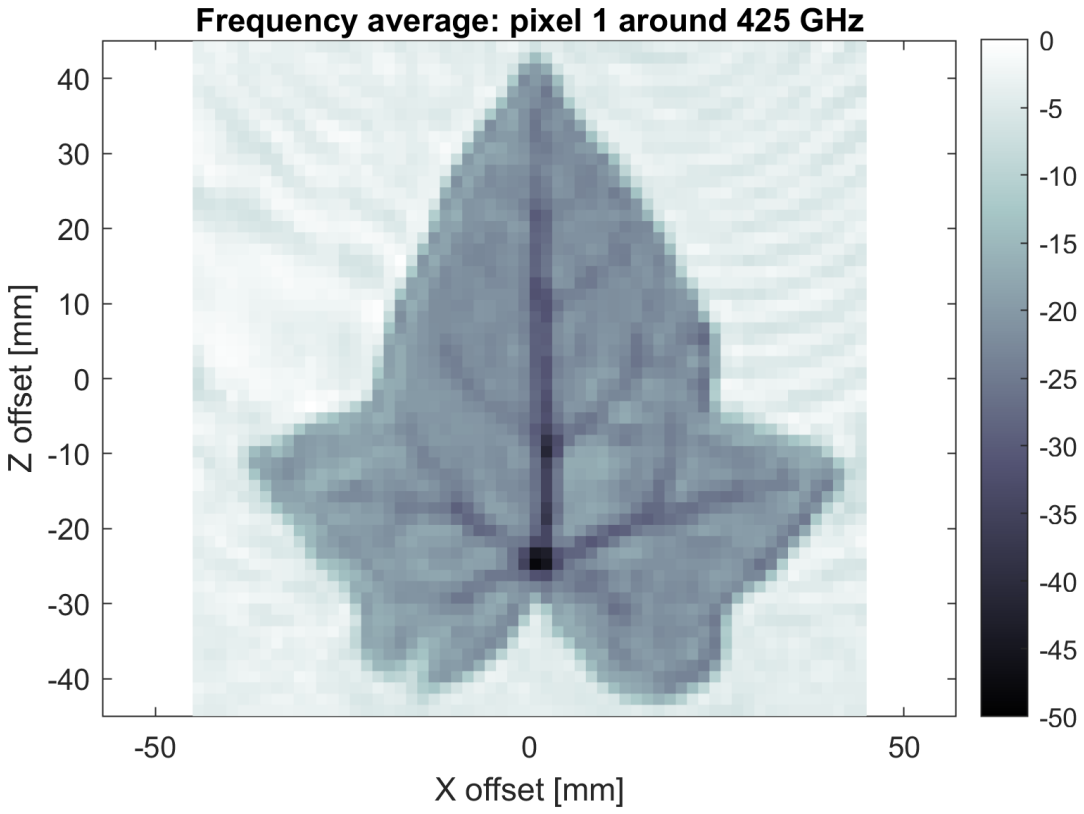

Figure C.35: Frequency-averaged image of ivy leaf around 425 GHz.

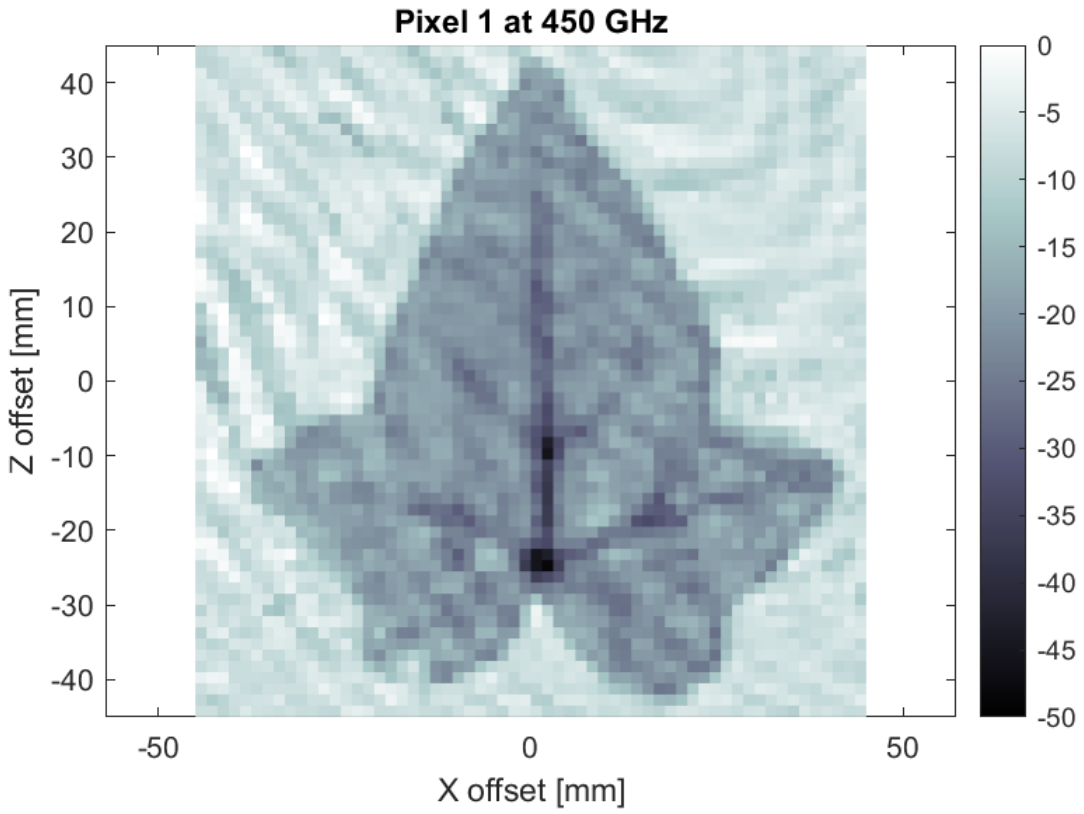

Figure C.36: Raw image of ivy leaf at 450 GHz.

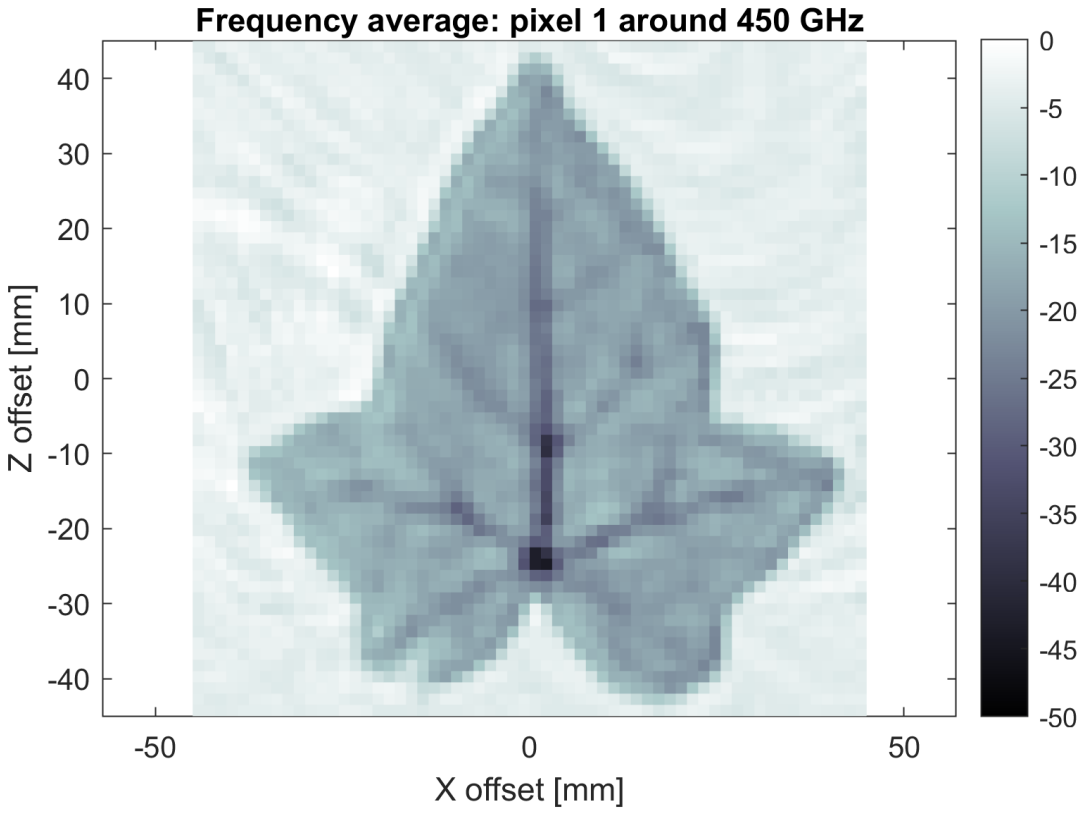

Figure C.37: Frequency-averaged image of ivy leaf around 450 GHz.

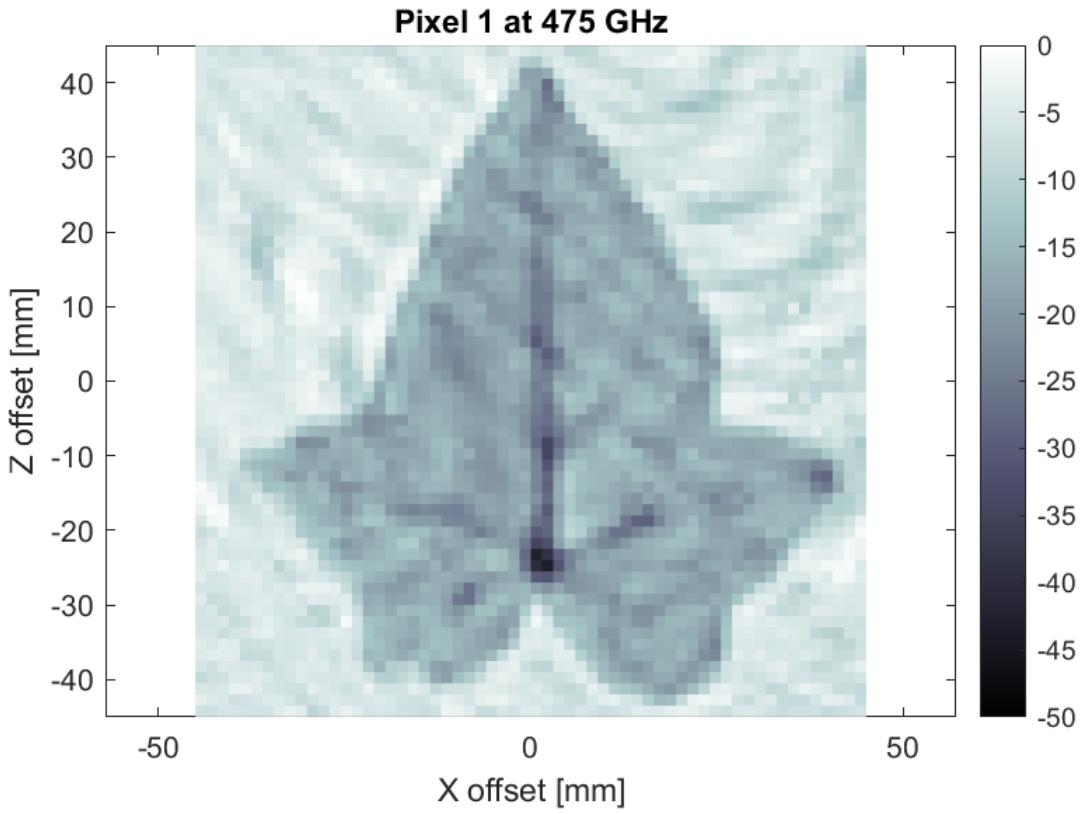

Figure C.38: Raw image of ivy leaf at 475 GHz.

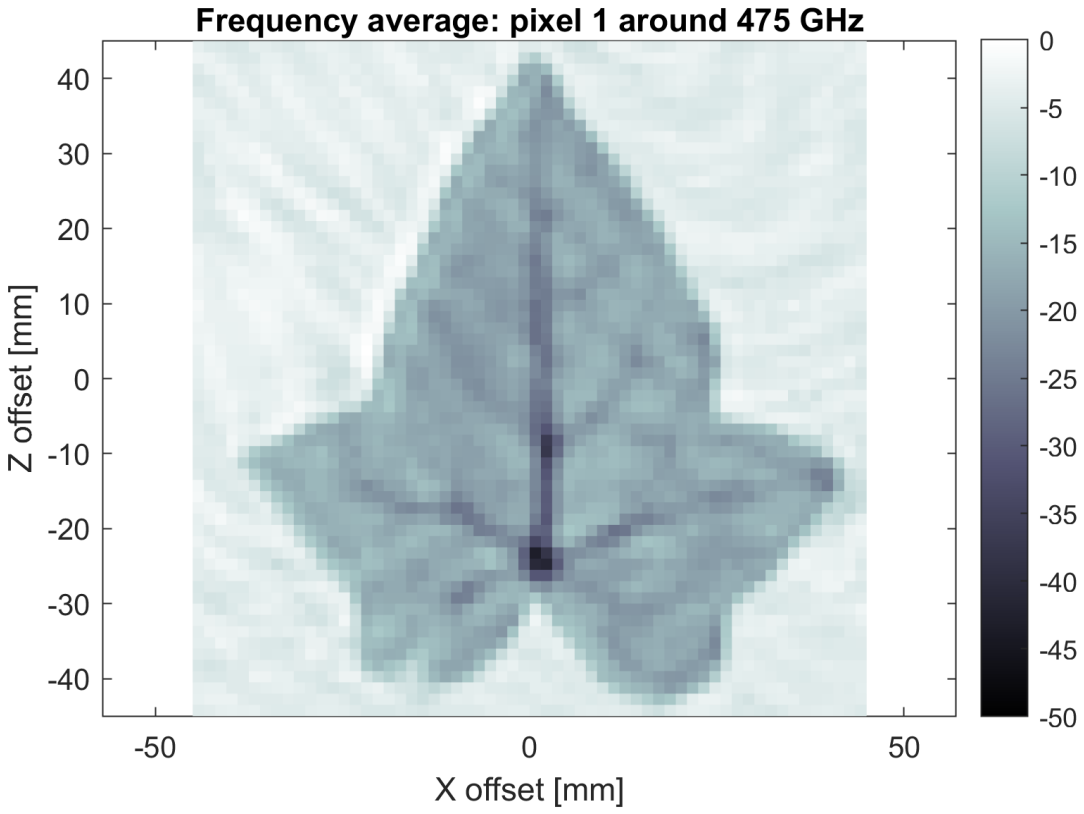

Figure C.39: Frequency-averaged image of ivy leaf around 475 GHz.